2018-04-26

Adaptive Energy Storage System Control for Microgrid Stability Enhancement

Tan Zhang
Worcester Polytechnic Institute

Adaptive Energy Storage System Control for Microgrid Stability Enhancement

by

Tan Zhang

A Thesis

Submitted to the Faculty

of the

WORCESTER POLYTECHNIC INSTITUTE

In partial fulfillment of the requirements for the

Degree of Doctor of Philosophy

in

Electrical and Computer Engineering

April 2018

APPROVED:

_____

Dr. Alexander E. Emanuel, Dissertation Advisor, ECE Department, WPI

_____

Dr. John A. Orr, Advisor, ECE Department, WPI

_____

Dr. Aleksandar Stanković, ECE Department, Tufts University

I hereby declare that I am the sole author of this thesis. This is a true copy of the thesis, including any required final revision, as accepted by my examiners.

I understand that my thesis may be made electronically available to the public.
For discussion with the author, please send email to: tanekzhang@gmail.com.

Abstract

Microgrids are local power systems of different sizes located inside the distribution systems. Each microgrid contains a group of interconnected loads and distributed energy resources that acts as a single controllable entity with respect to the grid. Their islanding operation capabilities during emergencies improve the resiliency and reliability of the electric energy supply. Due to its low kinetic energy storage capacity, maintaining microgrid stability is challenging under system contingencies and unpredictable power generation from renewable resources.

This dissertation highlights the potential benefits of flexibly utilizing the battery energy storage systems to enhance the stability of microgrids. The main contribution of this research consists in the development of a storage converter controller with an additional stability margin that enables it to improve microgrid frequency and voltage regulation as well as its induction motor post-fault speed recovery. This new autonomous control technique is implemented by adaptively setting the converter controller parameters based on its estimated phase-locked loop frequency deviation and terminal voltage magnitude measurement. This work also assists in the microgrid design process by determining the normalized minimum storage converter sizing under a wide range of microgrid motor inertia, loading and fault clearing time with both symmetrical and asymmetrical fault types.

This study evaluates the expandability of the proposed control methodologies under an unbalanced meshed microgrid with fault-induced feeder switching and multiple contingencies in addition to random power output from renewable generators. The favorable results demonstrate the robust storage converter controller performance under a dynamic changing microgrid environment.

Acknowledgements

If there is a God, I want to thank you for guiding me through this journey. For the past seven years, my life has been wonderful here at WPI. My family is the most important part of my life. And I miss you here during my study. I thank you for the continuous love, supports and sacrifices. I love you.

Words cannot express my gratefulness to my beloved mentors: Prof. Alexander Eigeles Emanuel and John Andrew Orr. For me, they are not just my advisors, but my American grandfather and father. They nurture my growth, both as a researcher and as a man. Thank you for guiding me with the patience, love and faith. Now it is the time for me to carry on your torch, and pass on to the next generation.

I consider myself very lucky to have Dr. Aleksandar Stanković as my dissertation examiner. It is inspiring to listen his insights on power system. I also appreciate Dr. Marija D. Ilić on willingness to provide the written feedback on my research.

Finally, I thank you all my friends who share my journey here at WPI. It is like a long marathon, and you help me go through those ups and downs. The memories we created along the way is my life treasure.

天行健， 君子以自强不息； 地势坤， 君子以厚德载物。

-《周易》

I Ching

DEDICATED TO

The people in my WPI journey

”I don’t think about the miles that are coming down the road, I don’t think about the mile I am on right now, I don’t think about the miles I’ve already covered. I think about what I’m doing right now, just being lost in the moment.”

– Ryan Hall, U.S. Olympic marathoner.

”When you’re in the day-to-day grind, it just seems like it’s another step along the way. But I find joy in the actual process, the journey, the work. It’s not the end. It’s not the end event.”

– Cal Ripken, Jr., retired MLB shortstop and 19-time All-Star.

”Doing my PhD feels like running a marathon. The most beautiful part of it is not crossing the finish line, but inside my each step of this journey itself.”

– Tan Zhang, Electrical engineer and marathoner.

Contents

1 Introduction **1**

1.1 Thesis Statement, Objectives and Contributions 1

1.2 Historical Background 4

1.2.1 Grid Evolution 4

1.2.2 Distributed Generation (DG) and Storage 5

1.2.3 Microgrids 6

1.3 Thesis Layout 7

2 Literature Review **9**

2.1 Energy Storage System (ESS) 9

2.2 Voltage-Sourced Converter (VSC) Control 11

2.3 Microgrid Operation 12

2.4 Microgrid Stability and Control 13

2.5 Chapter2 Summary 15

3 Fundamentals of Microgrid Stability, Modeling and Control **16**

3.1 Microgrid Stability 17

3.2 Microgrid Modeling 19

3.2.1 Electric networks 19

3.2.2 Loads 20

3.3 Synchronous Generator Modeling and Control 20
3.3.1 Modeling 20
3.3.2 Real power and frequency control 22
3.3.3 Reactive power and voltage control 25
3.4 Battery Energy Storage System (BESS) Modeling and Control 26
3.4.1 Converter modeling and current-mode control 26
3.4.2 Real/Reactive power/current capacity limitations 27
3.5 Chapter3 Summary 28

4 Adaptive Frequency Regulation **29**
4.1 Microgrid System for Chapter 4 29
4.2 Adaptive Primary Nonlinear Droop Control 30
4.3 Simultaneous Fast Secondary Frequency Control 34
4.3.1 Approach#1: Fixed Gain 34
4.3.2 Approach#2: Adaptive Gain 35
4.4 Cases Studies 36
4.4.1 Case#A: Unstable BESS operation with linear droop 37
4.4.2 Case#B: Stable BESS operation with nonlinear droop 40
4.5 Chapter4 Summary 45

5 Adaptive Voltage Regulation **46**
5.1 Microgrid System for Chapter 5 47
5.2 Induction Motor (IM) loads Impacts on Microgrid Dynamics and Stability 48
5.3 Concept 48
5.4 Implementation 52
5.4.1 Algorithm for adaptive voltage regulation set point: $V_{ref}(t)$ 53
5.4.2 Alternative: With Regulation Delays and Power Priority Switch . 56

5.5 Simulation Studies . . . 58
5.5.1 Transient Study#A: Impacts of BESS size on motor speed recovery 59
5.5.2 Transient Study#B: Advantage of adaptive voltage regulation . . . 66
5.5.3 Sensitivity Study#A: Minimum BESS size under symmetrical fault 70
5.5.4 Sensitivity Study#B: Minimum BESS size under asymmetrical fault 73
5.5.5 Transient Study#C: Multiple IMs recovery . . . 74
5.6 Chapter5 Summary . . . 78

6 Adaptive Control Evaluations on CIGRE Benchmark System 79
6.1 Microgrid System for Chapter 6 . . . 80
6.2 Study#1: Normal Voltage Regulation . . . 82
6.2.1 Case#A: Impact of BESSs secondary control approaches . . . 83
6.2.2 Case#B: Microgrid with and without BESSs - A comparison study 89
6.2.3 Case#C: Impact of asymmetrical fault . . . 93
6.2.4 Case#D: Multiple faults and renewable generation . . . 98
6.3 Study#2: Adaptive Voltage Regulation . . . 109
6.3.1 Case#A: Without voltage regulation control delay . . . 109
6.3.2 Case#B: With voltage regulation control delay . . . 121
6.4 Chapter6 Summary . . . 127

7 Conclusions 128
7.1 Summary . . . 128
7.2 Future Work . . . 130

A System Parameters 131
A.1 Radial Feeder for Chapter 4 and 5 . . . 131
A.2 Microgrid data for Chapter 6 CIGRE Benchmark System . . . 131

A.2.1 Feeder 131
A.2.2 Transformer 132
A.2.3 Loads 132
A.3 Synchronous generators 133
A.4 Prime movers and governing systems 134
A.5 Excitation systems 136
A.6 Inverter 136
A.7 Induction Motors 138

List of Abbreviations

AGC: Automatic Generation Control

BESS: Battery Energy Storage System

DER: Distributed Energy Resources

DFIG: Doubly-Fed Induction Generator

DG: Distributed Generation

EMS: Energy Management System

ESS: Energy Storage System

FIDVR: Fault Induced Delayed Voltage Recovery

HV: High Voltage

IM: Induction Motor

LFC: Load-Frequency Control

MV: Medium Voltage

PCC: Point of Common Coupling

PSS: Power System Stabilizer

PLL: Phase-Locked Loop

RES: Renewable Energy Source

VSC: Voltage-Sourced Converter

List of Symbols

Chapter 3

D: Load damping constant

H: Inertia constant (s) of the synchronous machine

δ: rotor angle, rad.

i_{dref}: Converter reference real current

i_{qref}: Converter reference reactive current

i_d: Converter real current

i_q: Converter reactive current

$\hat{i}$: Converter current magnitude

$\overline{P_a}$: Per unit accelerating power applied to the rotor.

$\Delta\overline{P_m}$: Generator input mechanical power change (pu)

$\Delta\overline{P_e}$: Generator output electrical power change including the losses (pu)

$\Delta\overline{P_L}$: Non-frequency-sensitive load change (pu)

$\Delta\overline{P_D}$: Frequency-sensitive load change (pu)

ω_s: Synchronous angular velocity (radians/s)

$\overline{\omega_s}$: Per unit synchronous angular velocity

$\Delta\overline{\omega}$: Per unit angular speed deviation of the rotor.

R_s: Generator governor speed regulation

$\overline{T_a}$: Per unit accelerating torque applied to the rotor.

Chapter 4

f_{db}: frequency regulator dead-band

f_r: Generator rotor speed

f_s: Estimated PLL frequency

$I_{d_{max}}$: maximum d axis current.

K_A: Gain parameter for adaptive nonlinear droop control

K_B: Gain parameter for adaptive secondary frequency control

K_I: Secondary frequency control gain

$K_{I_{max}}$: maximum allowable value of K_I

K_P: Primary droop gain

P_B: Battery real power

$P_{ref1}^{'}$: Converter nonlinear droop reference power under base power of converter rated power

P_{ref1}:: Converter nonlinear droop reference power under system base power

P_c: BESS rated power in pu under the system base.

P_{max}: Maximum allowable converter output power

R_c: Converter capacity saturation droop

$\hat{V}_{PCC}$: PCC voltage magnitude

Chapter 5

$\Delta f^{'}$: frequency deviation with respect to the nominal value

ω_{IM}: IM speed (rev/min)

f_{sw}: frequency deviation threshold for power priority switch

H_{IM_E}: equivalent motor inertia constant (s)

$I_{q_{max}}$: maximum q axis current.

I_{max}: maximum allowable converter current.

I_{sat}: converter saturation current

K_R: adaptive voltage reference value ramping rate

J_{IM}: IM inertia ($Kg.m^2$).

K_{IM}: IM load linear interpolation factor.

K_{V_I}: voltage regulator integral gain

Q_B: reactive power response of the BESS

Q_{max}: maximum allowable reactive power

S_B: BESS converter power rating in MVA

$\overline{S}_B$: normalized minimum BESS inverter size under microgrid loading base

S_m: total microgrid demand in MW.

t_{rs}: reset time (s)

T_M: load torque

T_r: rated torque of the IM

T_e: IM electromechanical torque

T_p: IM breakdown torque

V_{db}: voltage regulator dead-band

V_s: Source voltage

V_T: IM terminal voltage

$V_{ref}(t)$: voltage reference point for voltage regulator

V_{ref_N}: normal voltage reference point

V_{ref_E}: emergency voltage reference point

V_{th_H}: higher threshold voltage to deactivate the adaptive voltage regulation

V_{th_L}: lower threshold voltage to activate the adaptive voltage regulation

Z_s: short circuit source impedance

Chapter 6

P_{RE}: renewable power output.

List of Figures

3.1 Microgrid stability problems with usual reasons and improvement strategies. 18

3.2 Block diagram for transfer function relating (a). generator speed and power; (b). generator speed and power including the effects of the load damping. 22

3.3 Speed-droop governor schematic 23

3.4 Traditional Droop Control Concept 24

3.5 Two generators parallel operation with both primary and secondary frequency control. 25

3.6 Generic excitation control system block diagram (a). DC type; (b). AC type 26

3.7 Overall converter modeling and control block diagrams 27

4.1 Single-Line diagram of the chapter 4's studied microgrid system 30

4.2 Adaptive Nonlinear Droop: (a) Block diagram, (b) Resultant Droop Curve 31

4.3 Converter Frequency Regulator Block Diagram 34

4.4 Adaptive Secondary Frequency Controller Block Diagram 35

4.5 Estimated PLL frequency f_s for linear droop with $R_c = 1\%$ and secondary controller gain of 1000: (a). Overall unstable response, (b). Magnified oscillogram for $0.67 < t < 0.71s$, (c). Magnified oscillogram for $1.48 < t < 1.52s$. 38

4.6 Magnified PCC voltage oscillogram vs. time: for $0.53 < t < 0.73s$, inadmissible waveform quality for linear droop with $R_c = 1\%$ and secondary controller gain of 1000. 39
4.7 Unstable control performance: The BESS power vs. time for linear droop with $R_c = 1\%$ and secondary controller gain of 1000. 39
4.8 Estimated PLL frequency f_s for adaptive nonlinear droop with $R_c = 1\%$ and secondary controller gain of 1000. 41
4.9 Stable control performance: The BESS power vs. time for adaptive nonlinear droop with $R_c = 1\%$ and secondary control gain of 1000. 42
4.10 PCC voltage dq components vs. time with and without BESS adaptive control 43
4.11 Magnified PCC voltage oscillogram vs. time: (a). With BESS adaptive control, for $0.53 < t < 0.73s$, (b). With BESS adaptive control, for load#2 switched in at $t = 1.5s$, (c). Without BESS, for $0.53 < t < 0.73s$, (d). Without BESS, for load#2 switched in at $t = 1.5s$. 44
4.12 Synchronous generator rotor frequency f_r with and without BESS adaptive control 45

5.1 Single-Line diagram of the chapter 5's studied system 47
5.2 Induction motor free accelerating experiment single-line diagram: (a). Direct start, (b). With step-down transformer. 49
5.3 Induction motor free accelerating torque-speed curves 51
5.4 Torque-speed characteristics for an induction motor under different terminal voltage V_T 51
5.5 BESS PCC voltage regulator 52
5.6 $V_{ref}(t)$ operating state decision tree 54
5.7 The alternative $V_{ref}(t)$ decision tree 57

5.8 Induction motor speed ω_{IM_1} under different BESS sizes 60
5.9 $\hat{V}_{PCC}$ with and without 2.5 MVA BESS 61
5.10 Induction motor torque (T_{e_1}) versus time with and without 2.5 MVA BESS 61
5.11 Induction motor torque (T_{e_1}) versus speed (ω_{IM_1}) with and without 2.5 MVA BESS 63
5.12 BESS converter current d/q frame components versus time 63
5.13 BESS power versus time: (a). Real power, (b). Reactive power. 65
5.14 Generator frequency f_r versus time with and without 2.5 MVA BESS . . 66
5.15 Induction motor speed ω_{IM_1} with and without adaptive voltage regulation 68
5.16 $\hat{V}_{PCC}$ with and without adaptive voltage regulation 68
5.17 PCC voltage waveform oscillograms under adaptive voltage regulation, $1.40 < t < 1.55\ s$. 69
5.18 Torque of induction motor (T_{e_1}) versus time with and without adaptive voltage regulation 69
5.19 BESS converter current d/q frame components versus time, with and without adaptive voltage regulation 70
5.20 Normalized minimum BESS inverter size $\overline{S}_B$ as a function of equivalent motor inertia constant H_{IM_E} with fault clearing time as the parameter: (a). 34 % IM loading, (b). 47 % IM loading, (c). 55 % IM loading, (d). 61 % IM loading. 72
5.21 Minimum normalized BESS Size $\overline{S}_B$ as a function of fault clearing time under single-phase fault 74
5.22 Speed of the two induction motors versus time with 3.1 MVA BESS . . . 75
5.23 $\hat{V}_{PCC}$ with and without 3.1 MVA BESS 76
5.24 BESS power versus time under two induction motors loading: (a). Real power, (b). Reactive power. 77

5.25 Generator frequency f_r versus time with two induction motors loading and a 3.1 MVA BESS 78

6.1 GIGRE Test Network 81

6.2 Estimated PLL Frequency f_s; (left column): unstable under secondary controller with $K_I = 3000$, (right column): stable under secondary controller with adaptive gain using $K_B = 3 \times 10^5$: (a) f_{s_1}, unstable; (b) f_{s_2}, unstable; (c) f_{s_3}, unstable; (d) f_{s_1}, stable; (e) f_{s_2}, stable; (f) f_{s_3}, stable . . 85

6.3 The BESSs power vs. time; (left column): unstable under secondary controller with $K_I = 3000$, (right column): stable under secondary controller with adaptive gain using $K_B = 3 \times 10^5$: (a) P_{B_1}, unstable; (b) P_{B_2}, unstable; (c) P_{B_3}, unstable; (d)P_{B_1}, stable; (e) P_{B_2}, stable; (f) P_{B_3}, stable . . 86

6.4 The PCCs voltage magnitude $\hat{V}_{PCC}$ vs. time; (left column): unstable under secondary controller with $K_I = 3000$, (right column): stable under secondary controller with adaptive gain using $K_B = 3 \times 10^5$: (a) $\hat{V}_{PCC_1}$, unstable; (b) $\hat{V}_{PCC_2}$, unstable; (c) $\hat{V}_{PCC_3}$, unstable; (d) $\hat{V}_{PCC_1}$, stable; (e) $\hat{V}_{PCC_2}$, stable; (f) $\hat{V}_{PCC_3}$, stable 87

6.5 The synchronous generators rotor frequency f_r (Hz) vs. time; (left column): unstable under secondary controller with $K_I = 3000$, (right column): stable under secondary controller with adaptive gain using $K_B = 3 \times 10^5$: (a) f_{r_1}: $5\ MVA$ hydroelectric generator, unstable; (b) f_{r_2}: $1.8\ MVA$ diesel generator, unstable; (c) f_{r_3}: $3.125\ MVA$ diesel generator, unstable; (d) f_{r_1}: $5\ MVA$ hydroelectric generator, stable; (e) f_{r_2}: $1.8\ MVA$ diesel generator, stable; (f) f_{r_3}: $3.125\ MVA$ diesel generator, stable 88

6.6 The synchronous generators rotor frequency f_r (Hz) vs. time; with and without BESSs: (a) f_{r_1}: 5 MVA hydroelectric generator; (b) f_{r_2}: 1.8 MVA diesel generator; (c) f_{r_3}: 3.125 MVA diesel generator 90

6.7 Induction motors speed ω_{IM} vs. time, with and without BESSs: (a) ω_{IM_1}: 2250 HP; (b) ω_{IM_2}: 500 HP; (c) ω_{IM_3}: 2250 HP; (d) ω_{IM_4}: 500 HP 91

6.8 The PCCs voltage magnitude $\hat{V}_{PCC}$ vs. time; with and without BESSs: (a) $\hat{V}_{PCC_1}$; (b) $\hat{V}_{PCC_2}$; (c) $\hat{V}_{PCC_3}$ 92

6.9 Estimated PLL Frequency f_s under 12 cycles $asymmetrical$ fault: (a) f_{s_1}; (b) f_{s_2}; (c) f_{s_3} 94

6.10 The BESSs power vs. time under 12 cycles $asymmetrical$ fault: (a) P_{B_1}; (b) P_{B_2}; (c) P_{B_3} 95

6.11 The synchronous generators rotor frequency f_r (Hz) vs. time under 12 cycles $asymmetrical$ fault: (a) f_{r_1}: 5 MVA hydroelectric generator; (b) f_{r_2}: 1.8 MVA diesel generator; (c) f_{r_3}: 3.125 MVA diesel generator . . 96

6.12 The PCCs voltage magnitude $\hat{V}_{PCC}$ vs. time under 12 cycles $asymmetrical$ fault: (a) $\hat{V}_{PCC_1}$; (b) $\hat{V}_{PCC_2}$; (c) $\hat{V}_{PCC_3}$ 97

6.13 Renewable Energy Power Output P_{RE} under multiple faults (4 and 3 cycles fault clearing time respectively): (a) P_{RE_1}; (b) P_{RE_2} 100

6.14 Estimated PLL Frequency f_s under multiple faults and renewable generation ramping events with normal voltage regulation: (a) f_{s_1}; (b) f_{s_2}; (c) f_{s_3} 101

6.15 BESSs current magnitudes transients under multiple faults and renewable generation ramping events with normal voltage regulation: (a) BESS_1; (b) BESS_2; (c) BESS_3 102

6.16 BESSs real power vs. time under multiple faults and renewable generation ramping events with normal voltage regulation: (a) P_{B_1}; (b) P_{B_2}; (c) P_{B_3} 103

6.17 BESSs reactive power vs. time under multiple faults and renewable generation ramping events with normal voltage regulation: (a) Q_{B_1}; (b) Q_{B_2}; (c) Q_{B_3} 104

6.18 Induction motors speed ω_{IM} vs. time, under multiple faults and renewable generation ramping events with normal voltage regulation: (a) ω_{IM_1}: 2250 HP; (b) ω_{IM_2}: 500 HP; (c) ω_{IM_3}: 2250 HP; (d) ω_{IM_4}: 500 HP 105

6.19 The synchronous generators rotor frequency f_r (Hz) vs. time under multiple faults and renewable generation ramping events with normal voltage regulation: (a) f_{r_1}: $5\ MVA$ hydroelectric generator; (b) f_{r_2}: $1.8\ MVA$ diesel generator; (c) f_{r_3}: $3.125\ MVA$ diesel generator 106

6.20 The PCCs voltage magnitude $\hat{V}_{PCC}$ vs. time under multiple faults and renewable generation ramping events with normal voltage regulation: (a) $\hat{V}_{PCC_1}$; (b) $\hat{V}_{PCC_2}$; (c) $\hat{V}_{PCC_3}$ 107

6.21 Magnified PCC voltage oscillogram vs. time under multiple faults and renewable generation ramping events with normal voltage regulation: (a) V_{PCC_1}, first fault-induced islanding transient, $0.05 < t < 0.45\ s$; (b) V_{PCC_2}, first fault-induced islanding transient, $0.05 < t < 0.45\ s$; (c) V_{PCC_3}, first fault-induced islanding transient, $0.05 < t < 0.45\ s$; (d) V_{PCC_1}, second (islanding) fault-induced feeder switching transient, $3.5 < t < 3.9\ s$; (e) V_{PCC_2}, second (islanding) fault-induced feeder switching transient, $3.5 < t < 3.9\ s$; (f) V_{PCC_3}, second (islanding) fault-induced feeder switching transient, $3.5 < t < 3.9\ s$ 108

6.22 Renewable Energy Power Output P_{RE} under multiple (two) faults (7 and 4 cycles fault clearing time respectively): (a) P_{RE_1}; (b) P_{RE_2} 112

6.23 The synchronous generators rotor frequency f_r (Hz) vs. time under multiple faults and renewable generation ramping events with adaptive voltage regulation (no regulation delay): (a) f_{r_1}: $5\ MVA$ hydroelectric generator; (b) f_{r_2}: $1.8\ MVA$ diesel generator; (c) f_{r_3}: $3.125\ MVA$ diesel generator 113

6.24 The PCCs voltage magnitude $\hat{V}_{PCC}$ vs. time under multiple faults and renewable generation ramping events with adaptive voltage regulation (no regulation delay): (a) $\hat{V}_{PCC_1}$; (b) $\hat{V}_{PCC_2}$; (c) $\hat{V}_{PCC_3}$ 114

6.25 Magnified PCC voltage oscillogram vs. time under multiple faults and renewable generation ramping events with adaptive voltage regulation (no regulation delay): (a) V_{PCC_1}, first fault-induced islanding transient, $0.05 < t < 0.45\ s$; (b) V_{PCC_2}, first fault-induced islanding transient, $0.05 < t < 0.45\ s$; (c) V_{PCC_3}, first fault-induced islanding transient, $0.05 < t < 0.45\ s$; (d) V_{PCC_1}, second (islanding) fault-induced feeder switching transient, $3.5 < t < 3.9\ s$; (e) V_{PCC_2}, second (islanding) fault-induced feeder switching transient, $3.5 < t < 3.9\ s$; (f) V_{PCC_3}, second (islanding) fault-induced feeder switching transient, $3.5 < t < 3.9\ s$ . . . 115

6.26 Induction motors speed ω_{IM} vs. time, under multiple faults and renewable generation ramping events with adaptive voltage regulation (no regulation delay): (a) ω_{IM_1}: 2250 HP; (b) ω_{IM_2}: 500 HP; (c) ω_{IM_3}: 2250 HP; (d) ω_{IM_4}: 500 HP 116

6.27 Estimated PLL Frequency f_s under multiple faults and renewable generation ramping events with adaptive voltage regulation (no regulation delay): (a) f_{s_1}; (b) f_{s_2}; (c) f_{s_3} 117

6.28 BESSs current magnitudes transients under multiple faults and renewable generation ramping events with adaptive voltage regulation (no regulation delay): (a) $BESS_1$; (b) $BESS_2$; (c) $BESS_3$ 118

6.29 BESSs real power vs. time under multiple faults and renewable generation ramping events with adaptive voltage regulation (no regulation delay): (a) P_{B_1}; (b) P_{B_2}; (c) P_{B_3} 119

6.30 BESSs reactive power vs. time under multiple faults and renewable generation ramping events with adaptive voltage regulation (no regulation delay): (a) Q_{B_1}; (b) Q_{B_2}; (c) Q_{B_3} 120

6.31 The PCCs voltage magnitude $\hat{V}_{PCC}$ vs. time under multiple faults and renewable generation ramping events with adaptive voltage regulation (including regulation delay): (a) $\hat{V}_{PCC_1}$; (b) $\hat{V}_{PCC_2}$; (c) $\hat{V}_{PCC_3}$ 122

6.32 Induction motors speed ω_{IM} vs. time, under multiple faults and renewable generation ramping events with adaptive voltage regulation (including regulation delay): (a) ω_{IM_1}: 2250 HP; (b) ω_{IM_2}: 500 HP; (c) ω_{IM_3}: 2250 HP; (d) ω_{IM_4}: 500 HP 123

6.33 The synchronous generators rotor frequency f_r (Hz) vs. time under multiple faults and renewable generation ramping events with adaptive voltage regulation (including regulation delay): (a) f_{r_1}: $5\ MVA$ hydroelectric generator; (b) f_{r_2}: $1.8\ MVA$ diesel generator; (c) f_{r_3}: $3.125\ MVA$ diesel generator 125

6.34 Magnified PCC voltage oscillogram vs. time under multiple faults and renewable generation ramping events with adaptive voltage regulation (including regulation delay): (a) V_{PCC_1}, first fault-induced islanding transient, $0.05 < t < 0.45\ s$; (b) V_{PCC_2}, first fault-induced islanding transient, $0.05 < t < 0.45\ s$; (c) V_{PCC_3}, first fault-induced islanding transient, $0.05 < t < 0.45\ s$; (d) V_{PCC_1}, second (islanding) fault-induced feeder switching transient, $3.5 < t < 3.9\ s$; (e) V_{PCC_2}, second (islanding) fault-induced feeder switching transient, $3.5 < t < 3.9\ s$; (f) V_{PCC_3}, second (islanding) fault-induced feeder switching transient, $3.5 < t < 3.9\ s$ 126

A.1 CIGRE system loading 133

A.2 Diesel governor block diagram 134

A.3 MATLAB hydraulic turbine and governing system block diagram: (a). Overall model; (b). hydraulic turbine; (c). gate servomotor 135

A.4 PLL schematic and associated control block diagram 137

Chapter 1

Introduction

1.1 Thesis Statement, Objectives and Contributions

Deregulation of the electric utility industry as well as the need for a more sustainable and efficient future power system drive a broad range of technological developments including the proliferation of distributed generation (DG) units in the electrical distribution grid [1]. The increasing concerns regarding grid reliability and resiliency under both physical disturbances and cyber attacks support development of the capacity of islanding portions of distribution systems with groups of interconnected distributed energy resources (DERs) and loads as "Micro-Grids" during emergencies [2–4]. Consensus has been reached that microgrids will play a significant role in enhancing the performance of modern distribution systems by improving the quality and reliability of the electric energy supply [5].

The realization of microgrid benefits requires each microgrid to maintain stable frequency and voltage operation by implementing robust control of its DERs [6], especially during the unplanned islanding events such as fault-triggered islanding incidents [7]. This requires power engineers to develop innovative control strategies that can maintain electric power system stability under these challenging contingencies [1, 6].

The following conditions highlight the microgrid stability and control challenges:

1. The randomly varying power generation from distributed Renewable Energy Sources (RESs), unforeseeable load switchings, faults and their induced electric network reconfigurations, all create large disturbances on both microgrid frequency and voltage.

2. Low kinetic energy storage capacity and reduction of rotational inertia as synchronous generators are replaced by DERs with power converter interfaces within a microgrid further reduce ride-through capability.

3. The high degree of interaction among different DG units with various interfaces and differing controller characteristics can negatively impact overall microgrid stability.

Energy storage systems (ESSs) equipped with converter interfaces are capable of providing rapid real and reactive current/power support to a microgrid control system. They can be seen as either loads or generators depending on their modes of operation. Under proper control methodologies, those capabilities can be indispensable for facilitating a reliable and stable microgrid operation. Although previous work has proposed several new strategies using ESSs for microgrid frequency and voltage control under disturbance conditions [7, 8], their control methods are usually based on fixed microgrid topologies. Thus a microgrid with frequent system modifications or expansions may require multiple re-tunings of the controllers. This can make numbers of studies that address adaptive control approaches less practical [9–13]. It is of fundamental importance for an energy storage system to have simple yet effective adaptive control methodologies in order to make its microgrid truly robust under an unpredictable dynamic changing environment. Unfortunately, this has not been available to date and is the subject of this dissertation.

The goal of this dissertation is to address the aforementioned shortcomings by proposing a set of adaptive ESS control methodologies for both microgrid frequency and voltage

stability enhancements. This research has the following objectives:

1. To propose an autonomous adaptive frequency regulation strategy for fast microgrid frequency regulation via control of a battery energy storage system (BESS).

2. To propose an autonomous adaptive voltage regulation strategy for BESS converters to enhance both voltage recovery and induction motor (IM) speed recovery within a fault-triggered islanded microgrid, as the continuation of the work in Objective 1.

3. To evaluate the proposed adaptive ESS frequency and voltage regulation control methodologies with a realistic network topology.

This study has made the following contributions in the context of microgrid stability enhancements via adaptive ESS control analysis, design and implementation:

1. Introduced an improved fast frequency regulation strategy that combines a phase-locked loop (PLL) frequency measurement based adaptive nonlinear droop control with a simultaneous fast secondary control using BESS. It demonstrates the additional stability margin of the controller over the traditional frequency regulation method without performance sacrifice.

2. Developed an autonomous adaptive voltage regulation strategy for BESS converters that implements a simple yet effective way of achieving both faster voltage recovery and longer maximum permissible fault clearing/islanding time for a microgrid with one or more IMs.

3. Facilitated the microgrid design process by presenting the normalized minimum BESS inverter sizing under a wide range of microgrid motor inertia, loading and fault clearing times with both $symmetrical$ and $asymmetrical$ fault types.

4. Investigated the microgrid dynamics under CIGRE medium voltage (MV) distribution network benchmark system [14] with unbalanced loads, multiple IMs, renewable generators with converter interfaces and distributed synchronous generators with different prime resources (diesel fuel or hydropower). It also studied the impacts of voltage regulation delays inside the adaptive voltage regulation algorithm on microgrid dynamics.

5. Evaluated and demonstrated the robustness as well as expandability of the proposed adaptive ESS frequency and voltage regulation control methodologies under a meshed microgrid with fault-induced feeder switching and multiple contingencies in addition to random power output from RESs.

1.2 Historical Background

1.2.1 Grid Evolution

There is little doubt regarding the assertion that an interconnected electric grid may be the largest and most complex machine ever devised by man [15]. Since the birth of Thomas Edison's historic Pearl Street DC generation station in New York City on September 4, 1882, the electric power utility industry has grown to be one of the largest enterprises in the world over the past 136 years [16]. The transformer development by William Stanley Jr. as well as Nikola Tesla's inventions of polyphase AC machines and related systems broke the boundary of short distance DC power delivery to create an era of large-scale AC electric power distribution, signified by the commissioning of the Niagara Power Project's three-phase AC long-distance power transmission system on August 26, 1895. The large-scale electric grid was formed by gradually interconnecting isolated utility systems for achieving better reliability and economies of scale.

Several regulatory and market actions either shaped or redirected the grid evolution. Those movements started with the regulated monopolies concept introduced by Samuel Insull as the mark of the beginning of the regulation era following the Public Utility Holding Company Act (PUHCA) of 1935. The deregulation took place after the 1973 oil crisis through the Public Utility Regulatory Policies Act (PURPA) of 1978 with the Energy Policy Act of 1992 afterward. These enactments motivated engineers to develop distributed generation and renewable energy techniques. Although the incentives for better efficiency yielded to promotion of "alternative" fuel sources, it inflated the cost of building new infrastructures and hence discouraged the new investments on transmission lines [17]. Consequently, the electric grid is evolving toward a more de-centralized nature. Without proper actions to account these grid changes, the interconnected power grid continuously operates near its capacity limits under this market-based system. The 2000 California energy crisis began to show somewhat problematic nature of the new competitive energy market. A lacking grid infrastructures investments further contributed to the Great Northeast power blackout of 2003. Those challenges all motivated the Energy Policy Act of 2005. Today, the need for a more reliable, high-quality electric power to digital societies in an environmentally friendly and sustainable manner leads to the birth of the idea of a "Smart Grid" around the globe [18].

1.2.2 Distributed Generation (DG) and Storage

As previously stated, increasing amounts of electric power are generated from various DERs since 1970s (e.g., In 2016, DERs accounted for about 2 % of the installed generation capacity in the United States [1]). The major incentives include better use of the diverse energy resources of different types for greater energy savings and delivering efficiency. The environmental concerns of electric power generation lead to the continued

[1] source: https://www.ferc.gov/CalendarFiles/20180215112833-der-report.pdf

integration of renewable resources, especially wind and solar. DG can be categorized into dispatchable and non-dispatchable generation. The diesel-fueled generators, for example, are dispatchable. Most of the renewable generation, however, is non-dispatchable, with the exception of hydroelectric power generation. From the technical perspective, different DGs need different interfaces in order to be connected to their host utility grid. These can be divided into three groups: (i) synchronous generators, (ii) induction machines or (iii) power converters. Due to the increasing grid integration of non-synchronous generator based DERs, the overall power grid inertia is decreasing. Both the randomness of non-dispatchable resources and the reduction in power system inertia weaken the electrical grid and create operational difficulties in maintaining a reliable electric power supply.

The traditional power grid has very limited energy storage capability (mostly in the form of pumped hydro). However, the necessity of developing and deploying ESSs has been widely accepted in the face of the grid operational challenges under high penetration of DERs. It will be possible to make non-dispatchable resources dispatchable with the help of storage. As one will see in this thesis, the ESS can be a critical component for stable and reliable operation of a microgrid.

Both technical and economic aspects must be addressed in demonstrating the feasibility of both DGs and storage systems [19]. On the technical side, the goal is to effectively manage the DGs and storage in order to maximize their operational benefits in the electric grid. The microgrid concept presented in the following subsection serves as one of the most viable solutions to this task.

1.2.3 Microgrids

The U.S. Department of Energy defines a microgrid as ”a group of interconnected loads and distributed energy resources within clearly defined electrical boundaries that acts as a single controllable entity with respect to the grid. A microgrid can connect and disconnect

from the grid to enable it to operate in both grid-connected or islanded mode [20]."

Microgrid systems have been identified as key components of the future "Smart Grid". They provide multiple benefits that include [20]:

1. Capability for systematical integrating various types DERs and storage devices into the grid.

2. Ensuring a greater grid resiliency under physical and cyber attacks.

3. Ability to be self-healing from power system disturbances.

4. Potential to serve as "black start" entities for a faster restoration process during a blackout.

5. Meeting the electric energy delivery quality needs for critical and sensitive loads.

6. Supporting bulk power system by providing ancillary services such as demand shifting, deferral infrastructures investments, and frequency regulations.

1.3 Thesis Layout

The remaining six chapters of this dissertation are structured as follows:

Chapter 2 presents the literature summary related to the studied topics on energy storage, converter control, microgrid operation and stability.

Chapter 3 reviews the fundamentals of the microgrid stability definition, modeling concepts and control principles of its DERs as essential tools and background knowledge for this research.

Chapter 4 proposes the adaptive frequency regulation strategy in order to help the microgrid frequency quickly return to its nominal value with a zero steady state error after

disturbances. This improved control methodology combines a PLL frequency measurement based adaptive nonlinear droop control with a simultaneous fast secondary control using BESS. Two case studies show the additional stability margin gained by adaptively changing the controller gains based on the estimated PLL frequency deviation. Simulation results reveal the robustness of the control under both fault induced islanding and load switching during microgrid autonomous operation.

Chapter 5 introduces the new adaptive voltage regulation strategy for BESS converters as the continuation of the work in Chapter 4. This is implemented by adaptively setting the voltage regulator reference point after sensing the low voltage condition. This new autonomous control strategy outperforms conventional voltage regulation by enabling IMs to achieve a higher electromechanical torque for successful fault ride-through. The results also assist in the microgrid design process by determining the normalized minimum converter size as a function of the IM inertia, loading, fault types and clearing time.

Chapter 6 evaluates the effectiveness and robustness of the overall proposed adaptive ESS control methods, combining both adaptive frequency regulation from Chapter 4 and adaptive voltage regulation from Chapter 5. The studied meshed microgrid is based on the CIGRE MV distribution network with both synchronous generator and inverter based resources. The microgrid loadings are mixed with RLC impedance and IM loads. The results demonstrate significant enhancements of the microgrid stability and resiliency under multiple disturbances with the help of the proposed BESS's autonomous control. The investigated transient events include fault-induced islanding (both $symmetrical$ and $asymmetrical$ faults), isolated microgrid internal fault with topology change induced by feeder switching, as well as, random power generation from RESs.

Chapter 7 summarizes the study and suggests future work. An appendix details the system parameters including the simulated microgrid network, generators and load data.

Chapter 2

Literature Review

This presentation aims to give a comprehensive view of the current art and identify the gaps regarding this dissertation's research topics.

2.1 Energy Storage System (ESS)

The potential opportunities and operating benefits of grid-tied ESSs have long been well-recognized [21]. The DOE/EPRI Electricity Storage Handbook in 2005 [8] provides an extensive information resource guide on the stationary ESSs regarding their use cases, benefits, technologies, and development stages. The costs and evaluation tools for both the economic and technical analyses are also detailed. A recent technology development review is given in [22] for high power storage devices such as supercapacitors and flywheels. A good technical analysis regarding the flywheels design, modeling and associated passivity-based power electronic control for power system stability enhancement under wind power plants is presented by Bachovchin from Carnegie Mellon University [23]. The study in [24] also uses a passivity-based control design method and shows the potential to combine the application of STATCOM and battery energy storage to enhance

the transient stability of large-scale multimachine power systems with synchronous and doubly-fed induction generators (DFIGs). The work in [25] shows a method for dimensioning a storage device to provide a primary frequency reserve. Another piece of work related to this high power ESS application on electric grid frequency regulation is given by Leitermann from MIT [26], it highlights the characteristics of the frequency regulation signal that are important for dividing the regulation loads between an energy storage unit and a traditional generator. It also points out the potential for a near-instantaneous frequency response from an ESS. This dissertation provides a novel adaptive ESS control approach inside microgrids for a fast frequency regulation service.

The importance of ESS on microgrid operation and control is reflected in several studies [27–31]. The ability of a storage device to provide inertial response by adding additional converter control loop to account for frequency rate of change is shown in [27]. It mentions adaptive control for frequency controller parameter tuning as a future work. The same group of researchers experimentally demonstrate the microgrid performance enhancements and possible resynchronization accomplished by additional monitoring and hysteresis triggering circuits [28]. A multiple ESS control study is conducted in [29]. It uses a deadband droop in combination with SoC gain scheduling to set power references. The Consortium for Electric Reliability Technology Solutions (CERTS) report [30] details the battery storage systems field testing results including parallel operation with synchronous generators. The capacity limits of the storage converter must be respected for a reliable operation. Finally, the authors in [31] investigate the short-term ESS frequency control support in a French island with high penetration of wind or solar generation. It demonstrates the benefits for high power storage devices on mitigating the impacts of non-inertia type generation on the dynamic performance of island systems under major generation outage.

2.2 Voltage-Sourced Converter (VSC) Control

The effective utilizations of power-electronic converters hold a key role on the integration of DERs for a more flexible and reliable future power systems [32–36]. The authors in [37] present an excellent early analysis on vector control for converters. Good overview of control and synchronization methods can be found in [38, 39]. Several papers provide the converter PLL design and analyses tools [40–43]. A novel grid synchronization method by means of virtual oscillator control is presented in [44]. Some literature advocates for the potential of a converter to mimic synchronous machine dynamics and control as a "virtual" synchronous machine [45,46]. The work in [47] expands on this thesis converter modeling and study by detailing the design and control guidelines for an LCL-filter-based three-phase active rectifier. The converter scaling rule proposed in [48] further assists this dissertation research's sensitivity study on BESS sizing.

In the view of VSC in power systems, the book [49] by Yazdani gives a comprehensive presentation for VSC modeling, control and applications. Load sharing techniques for converters in both AC and DC grids have been investigated for decades under the umbrella of droop control [50–58]. These works introduce several modified droop control methodologies such as real/reactive current droop [52], signal injection and measurement based droop control in [53], droop control with inverter output impedance turning in AC grids [55, 56], as well as probable adaptive droop control in Multi-Terminal DC (MTDC) grids [57, 58]. The studies in [59, 60] tackle the flexible converter real & reactive power/current control methodologies during grid faults for a better fault ride-through. The DERs' VSC control strategies have profound impacts on microgrid dynamics and energy supply quality [61–68]. The report [61] gives a detailed summary as well as future trends on the power converter microgrid operation modes and control structures with three configurations: grid-forming, grid-feeding and grid-supporting.

2.3 Microgrid Operation

Extensive amount of literature focuses on the microgrid operation and energy management system (EMS). The reports of [69–71] show some of the early work on CERTS microgrid and its autonomous control strategy. Recent publications rectify this ongoing effort by providing experimental results on model and control validation of the natural gas generator set [72], updating the refinement of the EMS design and implementation with parallel BESS, RES, as well as synchronous generators operating via traditional droop control to achieve $Plug-and-play$ functionality [73]. It indicates the importance for a fast frequency regulation capability via batteries sources to improve the grid stability [73]. Another series of work from Katiraei [1, 74–76] provide good inspirations for his pioneer study on real/reactive power management of DERs on microgrid dynamics. Its real power control is based on the standard frequency droop with restoration integral control under a large time constant. Moreover, three reactive power management strategies based on: (1). voltage-droop, (2). voltage regulation and (3). power factor correction are explored.

A classic paper dealing with microgrid islanded operation with both primary and secondary control is [6]. In [77], the authors propose a voltage-power droop/frequency-reactive power boost (VPD/FQB) control scheme to droop voltage reference for real power sharing and frequency reference for reactive power sharing inside a converter fed microgrid. The work in [78] introduces a combined angle-frequency droop controller for both converters and synchronous generators using nonlinear control law for better power sharing and more flexible control. The voltage and frequency dependent load impacts on microgrid operation can be found in [79], where the dependency between microgrid voltage and frequency as well as possible instability are shown to be caused by the load dynamics. The propositions of utilizing a distributed secondary control system with local communication are shown in [80, 81]. The study in [82] demonstrated the feasibility

for stand-alone DFIGs with autonomous frequency control during islanded operation via PLL. Several papers [83–85] conducted good literature surveys on the present practice and future trends of distributed and hierarchical control for microgrids.

The aforementioned works indicate the value of flexible converter-based dispatchable DER control strategies on enhancing microgrid operations. This dissertation research on the efficacy of BESS application for autonomous fast frequency regulation builds on these past works and combines both distributed primary and secondary control using PLL.

2.4 Microgrid Stability and Control

The microgrid and bulk power system stability shares the same fundamental concepts [86, 87]. Due to the high level penetration of converter interfaced DERs, many of the microgrid stability problems are either originated or heavily influenced by their converters' dynamics and control [88–90]. Due to this unique aspect, many researchers have been dedicating on enhancing the microgrid stability performance via modifying the converters control loops [36, 91–94]. Some new techniques and methods include introducing a combination of repetitive and deadbeat control with feedforward compensation for disturbance rejection [92], secondary control based on potential-function [93], real-time small signal stability analysis for droop gain schedule [91] and droop gain variation for increasing virtual inertia [94].

There are various methods to analyze and predict the stability of microgrids [95–101]. All of them serve important roles on providing analytical tools for microgrid controllers design. The small signal models of the converter based microgrid is well-established in [96, 97]. The active loads impacts on system small-signal stability are analyzed in [98], it shows the active loads with a large dc voltage controller gain may lead to instability. Similarly, the system is more prone to become unstable when the microgrid system unbal-

ance level increases [99]. A combination of small-signal and time-domain simulation are usually used for a comprehensive stability analysis [7, 95, 99, 102, 103]. Another popular analytic tool for grid-connected inverters is the impedance-based stability criterion [101], which is based on an old concept from [104].

Numerous control methodologies have been proposed to enhance the microgrid stability [9–13,105–107]. Two studies in [105,106] present novel frequency regulation methods of microgrid by either utilizing the kinetic energy from the IM loads [105] or load voltage sensitivity via voltage regulation [106]. Both methods can reduce the amount of needed energy storage in microgrid. There are extensive references that fall within the category of adaptively controlling converter in microgrid power system [9–13, 107]. An early adaptive droop adjustment based on the microgrid small signal model is introduced in [9]. The authors in [10] use the on-line grid parameter estimation combined with small signal stability analysis to detect the islanding and adjust the inverters droop control parameters. The droop scheduling scheme based on bifurcation theory is presented in [11] to find the worst primary reserve share that is closest to instability. A mode-adaptive droop control method was proposed in [12]. Two nonlinear droop controls are proposed in [13, 107] to enhance microgrid frequency regulation. Nonetheless, it may either require multiple small signal stability analyses to determine the acceptable droop gains [13] or lead to instability due to a high droop gain when the frequency is close to the nominal value [107]. Both aspects are problematic for the practical implementations. On the contrary, the adaptive frequency regulation strategy developed in this dissertation aims to provide a simple, efficient and robust control action under dynamic changing microgrid environments.

2.5 Chapter2 Summary

The prior work not only indicates a great potential for ESSs to enhance the microgrids stability via fast converter control but also points out the need for a more flexible, simpler yet more effective way of utilizing the limited converter capacity. Building on top of the prior work, this dissertation research developed a set of adaptive ESS control strategies for both microgrid frequency and voltage stability enhancements. This work focuses on the real time control process under the inspirations from [108, 109]. In a microgrid that may encounter frequent topology changes and load switchings, the control laws must also be adaptable to those uncertainties. This is achieved by adjusting the BESS converters controllers parameters adaptively via utilizing their PLL and terminal voltage measurements.

Chapter 3

Fundamentals of Microgrid Stability, Modeling and Control

The purpose of this chapter is to provide essential background review for this dissertation research. The presentation aims to:

1. Provide precise definition of microgrid stability problems investigated in this study.
2. Clarify microgrid modeling techniques as well as assumptions in this work regarding the electric networks, loads, synchronous generators and BESS.
3. Review the synchronous generator's governing control system and its primary droop and secondary controls during power system frequency regulation process.
4. Present the synchronous generator's voltage regulation methodology via excitation control systems and associated power system stabilizer (PSS).
5. Discuss the overall power converter $current - mode\ control$ and its real/reactive power/current constrains during operation.

3.1 Microgrid Stability

This research considers the general microgrid stability as same as the formal power system stability definition in [87], which is:"the ability of an electric power system, for a given initial operating condition, to regain a state of operating equilibrium after being subjected to a physical disturbance, with most system variables bounded so that practically the entire system remains intact."

While analyzing the microgrid stability problems, one must take advantage of previous large-scale power system stability research efforts while identify their critical distinctions. In order to develop appropriate stability enhancement strategies, it is of fundamental importance to understand the physical nature of the instability phenomena that are unique for microgrids, which are reflected in the thesis statements (Ch. 1.1). This dissertation categorizes the microgrid stability problems based on previous work in [15, 87], under following considerations:

- The physical nature and cause of the microgrid instability;
- The size of the disturbance relative to the studied microgrid systems;
- The devices, processes, and the time span that are critical for determining microgrid stability; and
- The appropriate method to assess and predict the microgrid stability.

Figure 3.1 presents the overall picture of the microgrid system stability problem. The unique origins of the microgrid instability and probable enhancement methods are emphasized in bold at the necessary places.

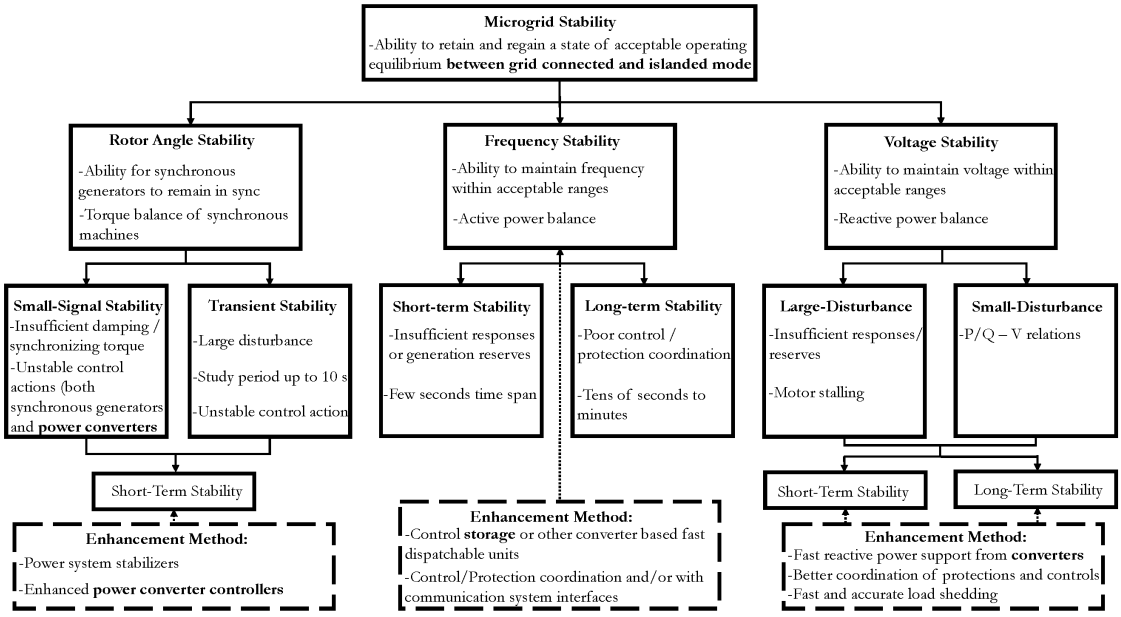

Figure 3.1: Microgrid stability problems with usual reasons and improvement strategies.

This study focuses on microgrids frequency and voltage stability. The frequency stability is ”the ability of a power system to maintain steady frequency following a severe system upset resulting in a significant imbalance between generation and load. [87]” And the voltage stability refers to ”the ability of a power system to maintain steady voltage at all buses in the system after being subjected to a disturbance from a given initial operating condition. [87]” Similar to the bulk power system, the microgrid frequency stability is largely depends on the real power demand-supply balance and the reactive power balance is critical for microgrid voltage stability. Moreover, this thesis analyses make sure to keep the overall microgrid stability in mind since different categories of microgrid instability phenomena can have high degree of overlapping. For examples, during the low voltage condition caused by the faults, the motors may lose stability by means of running toward the stall and this indeed can further worse both microgrid voltage and frequency [110]. Moreover, the instability of the power converter controllers can cause microgrid synchronous generators loss synchronism and lead to inadmissible overall system voltage

profiles at the same time.

In the case of high penetration of DERs with converter interfaces and stochastic power generation from RESs, maintaining a stable microgrid frequency even during normal operations can be difficult due to the significant reduction of microgrid rotational inertia as well as slow real power control from synchronous generators. Similarly, the insufficient microgrid capabilities to fast regulate system voltage after the contingencies can result a sustained low voltage condition or even voltage collapse in the case with substantial IM loads. This research considers the short-term microgrid frequency and voltage stabilities in a time frame from a fraction of a second to a few seconds. The goal is to develop a set of novel adaptive ESS control strategies for a fast and accurate real/reactive power support to ensure a stable and reliable microgrid operation under severe disturbances.

3.2 Microgrid Modeling

3.2.1 Electric networks

The microgrid electric network is modeled under the general settings of the MV electric power distribution [111]. The distributed parameter line models are used to model the feeder [112]. To evaluate the expandability of the proposed control, this dissertation case studies consider all three types of feeder, which include: (i). radial, (ii). loop and (iii). meshed network [113].

Chapter 4 and 5 use a radial feeder topology, adapted from [1, 114], as the first platform to carry on the proposed ESS adaptive control strategies studies under a microgrid of full feeder scale. Chapter 6 expands the work into a full substation microgrid with loop and/or meshed distribution systems based on the CIGRE MV distribution network benchmark for the further control verifications [14].

3.2.2 Loads

The studied microgrid systems include both $static$ and $dynamic$ load models [15].

Static load model: RLC impedance

Instead of widely used ZIP (constant impedance, constant current, constant power) model [115], this thesis chooses the linear RLC impedance as the $static$ load model to avoid the convergence issues during the low voltage conditions caused by the studied contingencies (e.g., faults).

Dynamic load model: induction motor

The induction motor is the workforce of the industry and typically consume 60% to 70% of the total energy supplied by a power system [15]. Therefore, this research considers three-phase single squirrel-cage induction machine as the $dynamic$ load model. The nonlinear differential equations based on reference-frame theory that described the induction machine are simulated [116]. The parameters of the machine are taken from [117], summarized in Appendix A.7.

3.3 Synchronous Generator Modeling and Control

3.3.1 Modeling

The modeling and analysis of a synchronous machine has always been a central part in understanding the power system operation and study the power system stability [118]. This work uses a 6^{th} order state-space model as the electric part of the machine, represented in the rotor reference frame (dq frame) [119]. It takes the dynamics of the stator, field and damper windings into considerations. The mechanical system is represented by

a single equivalent rigid mass as [120]:

$$\frac{2H}{\omega_s}\frac{d^2\delta}{dt^2} = \overline{T_a} = \overline{P_a} \tag{3.1}$$

where:

H = synchronous machine inertia constant in (MJ/MVA) or simply (s), as equal to the machine kinetic energy in joules at the rated speed divided by the rated apparent power of the machine.

δ = rotor angle, the electrical equivalent angular displacement of the rotor (radians) with respect to the synchronously rotating reference axis.

$\overline{T_a}$ =per unit accelerating torque applied to the rotor.

$\overline{P_a}$ =per unit accelerating power applied to the rotor

ω_s =synchronous angular velocity (radians/s)

and with:

$$\frac{d^2\delta}{dt^2} = \frac{d\Delta\omega}{dt} = \omega_s\frac{d\Delta\overline{\omega}}{dt} \tag{3.2}$$

where:

$\Delta\overline{\omega}$ = per unit angular speed deviation of the rotor.

One also deducts the following equation governing the alternator rotor dynamic [15]:

$$\frac{d\Delta\overline{\omega}}{dt} = \frac{1}{2H}\overline{P_a} \tag{3.3}$$

3.3.2 Real power and frequency control

Speed-droop governor [15]

Following the (3.3), the equivalent generators and load composite response to a small rotor frequency deviation (denoted by $\Delta\overline{\omega}$) can be mathematically expressed as:

$$\begin{aligned} \overline{P_a} &= \Delta\overline{P_m} - \Delta\overline{P_e} \\ \Delta\overline{P_e} &= \Delta\overline{P_L} + D\Delta\overline{\omega} = \Delta\overline{P_L} + \Delta\overline{P_D} \end{aligned} \tag{3.4}$$

where

$\Delta\overline{P_m}$ = Generator input mechanical power change (pu)

$\Delta\overline{P_e}$ = Generator output electrical power change including the losses (pu)

$\Delta\overline{P_L}$ = Non-frequency-sensitive load change (pu)

$\Delta\overline{P_D}$ = Frequency-sensitive load change (pu)

D = Load damping constant

Figure 3.2 shows the generator and its load response block diagrams.

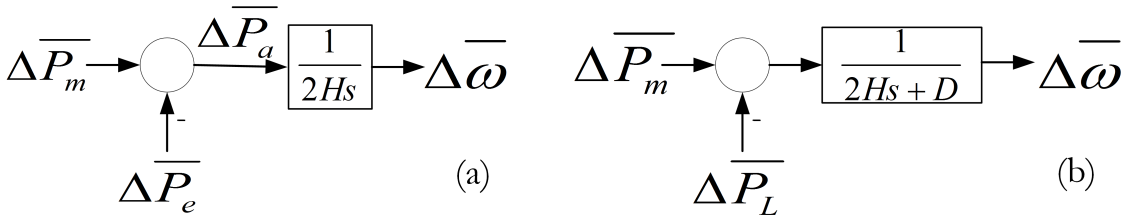

Figure 3.2: Block diagram for transfer function relating (a). generator speed and power; (b). generator speed and power including the effects of the load damping.

A speed-droop governor control system senses this generator per unit rotor speed deviation ($\Delta\overline{\omega}$) with respect to its per unit synchronous angular velocity ($\overline{\omega_s}$), inputs to a servomotor (modeled by an integrator with amplification gain K) and provide the valve/gate position actuating signal ΔY to adjust the generator input mechanical power P_m. Fig. 3.3 shows such speed-droop governor schematic.

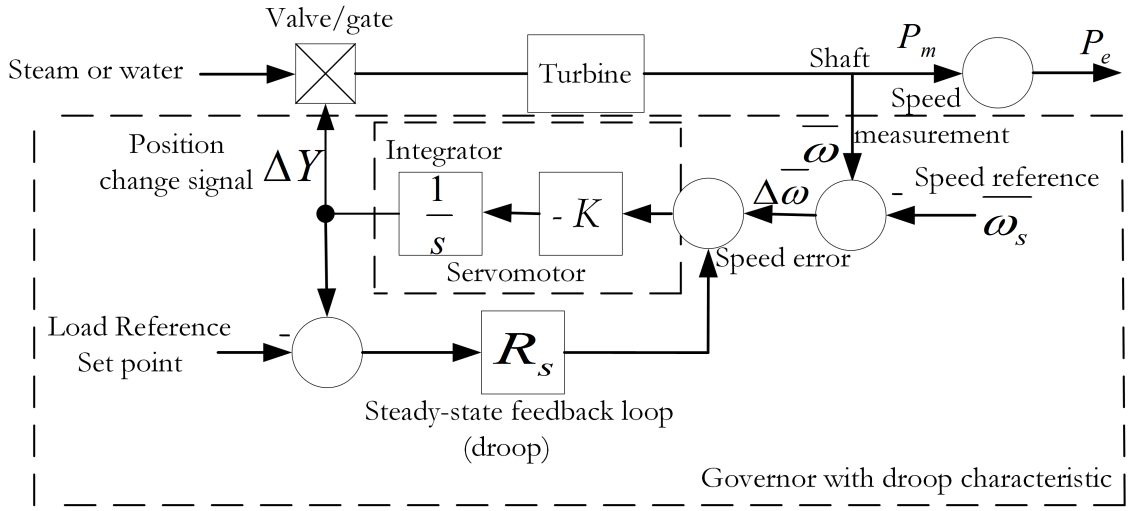

Figure 3.3: Speed-droop governor schematic

The steady-state feedback loop with droop gain R_s results a speed-droop governor characteristic. The parameter R_s also refers as speed regulation expressed in percent %. For example, $R_s = 5\%$ means the generator governor control system will change 100% of its power output when experiences a 5% rotor frequency deviation. Appendix A.4 summarizes the hydraulic and diesel engine governor systems used in this study.

Primary droop control and power sharing [15]

With speed-droop governors, multiple synchronous generators can operate in parallel and autonomously share the load change when they all experience a sudden rotor frequency deviation. The concept of two units' power sharing via primary droop control is explained in Fig. 3.4.

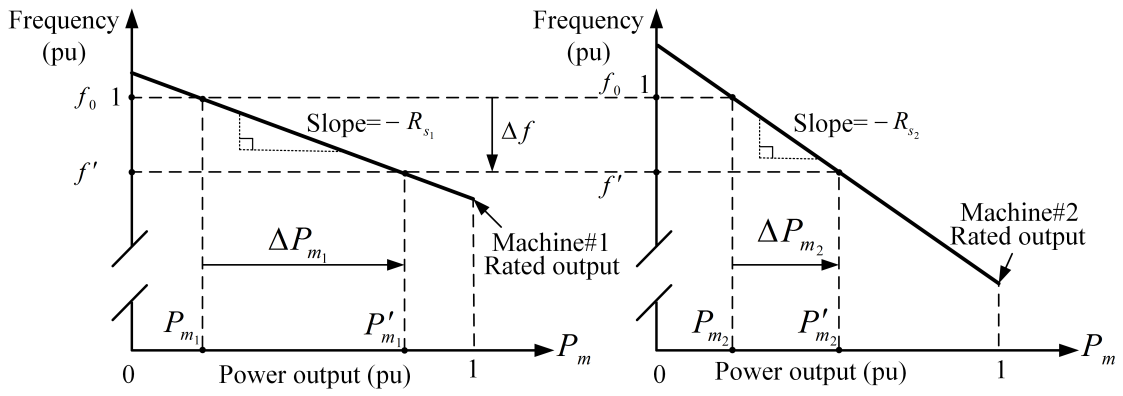

Figure 3.4: Traditional Droop Control Concept

It shows that each generator picks up load based on their own speed regulation R_s:

$$\frac{\Delta P_{m_1}}{\Delta P_{m_2}} = \frac{R_{s_2}}{R_{s_1}} \tag{3.5}$$

Hence a generator governor with a smaller percent R_s will pick up more load change during a frequency disturbance.

Secondary frequency restoration control [15]

A secondary control, also referred as $automatic\ generation\ control$ (AGC) or $load - frequency\ control$ (LFC), adjusts the selective generators' load reference setpoints to restore the power system frequency after the primary droop control. The idea is illustrated in Fig. 3.5 two units system. It shows the supplementary integral control action on units # 1. Meanwhile, it also represents the two units primary control loop and overall generator-load response.

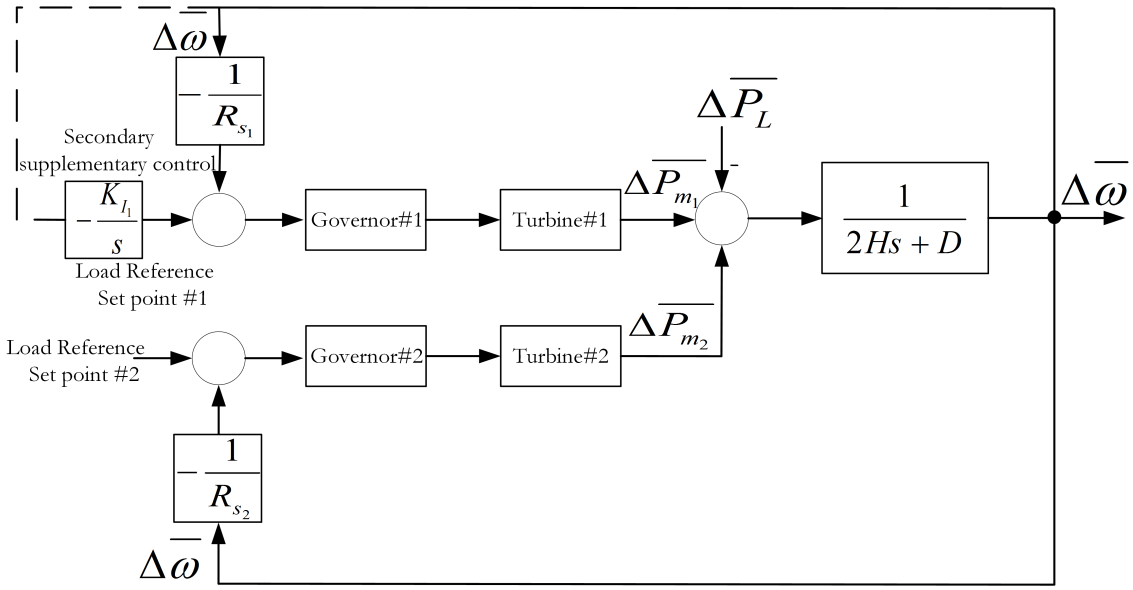

Figure 3.5: Two generators parallel operation with both primary and secondary frequency control.

The design of secondary frequency restoration (i.e., AGC) control system via synchronous generators for a interconnected power grid is a nontrivial task and must consider both technical and economical aspects [121]. Comparing to the primary droop control, the AGC regulation takes much longer time (30 seconds to minutes). On the contrary, it is probable to utilize both primary and secondary frequency control actions via fast BESS converter control to accomplish a rapid microgrid frequency regulation under dynamic changing operational conditions, proposed in Chapter 4.

3.3.3 Reactive power and voltage control

An excitation system controls the synchronous machine terminal voltage and reactive power. This work uses a DC excitation system (Type $DC1C$) for hydroelectric generator and AC excitation system (Type $AC1C$) for diesel generator [122]. A multi-band power system stabilizer (PSS) (Type $PSS4C$) are also equipped at hydroelectric generator's DC excitation system to enhance the damping of power system oscillation [119, 122].

The input signal to PSS is the generator shaft speed.

The generic DC and AC excitation control systems are shown in Fig. 3.6 [123]. Both of them are composed of an amplifier connected in series with a main excitor [1]. The associated excitation systems parameters (gains, time-constants, limiters, non-linear function relations and constant coefficients) are summarized in Appendix A.5.

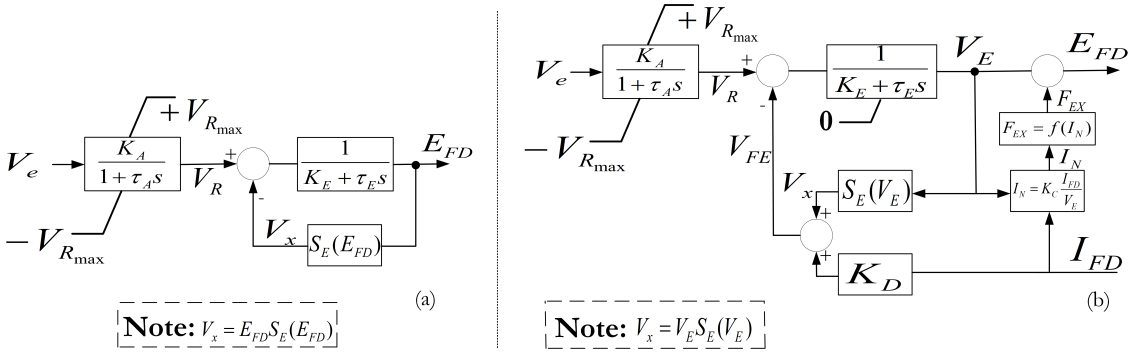

Figure 3.6: Generic excitation control system block diagram (a). DC type; (b). AC type

3.4 Battery Energy Storage System (BESS) Modeling and Control

3.4.1 Converter modeling and current-mode control

This study is based on a simplified simulation model of the BESS as average model of its converter. The overall converter modeling and control block diagram is summarized in Fig.3.7 [49]. The BESS is represented as three linear, dependent voltage sources, connected to PCC through series RL branches. This approach allows one to focus on the converter control strategies' impact on system performance without worrying about the dynamics of the battery sources at the DC side and converter switching harmonics [49]. The figure also shows the associated $d-q$ frame control block diagrams and signal flow. The $current-mode\ control$ is used to regulate the converter injected real and reactive

currents with respect to the PCC voltage. The reference real current (i_{dref}) and reactive current (i_{qref}) are obtained from converter frequency and voltage regulator respectively. The settings of the PLL and current controller are adopted from [49]. Their parameters can be found in Appendix A.6.

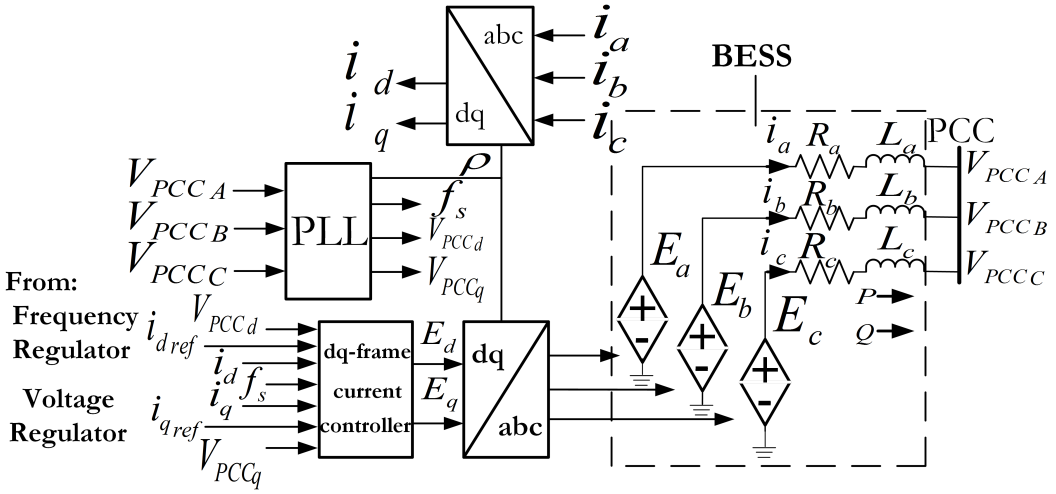

Figure 3.7: Overall converter modeling and control block diagrams

3.4.2 Real/Reactive power/current capacity limitations

The converter output current magnitude $\hat{i}$ can be expressed as:

$$\hat{i} = \sqrt{(i_d)^2 + (i_q)^2} \tag{3.6}$$

where

i_d = Converter real current (pu)

i_q = Converter reactive current (pu)

The main converter capacity constrain is its current magnitude $\hat{i}$ should not exceed its maximum allowable value I_{max}. Under a fast $current - mode\ control$, the $i_d \approx i_{dref}$, $i_q \approx i_{qref}$ and hence $\hat{i} \approx \hat{i}_{ref} = \sqrt{(i_{d_{ref}})^2 + (i_{q_{ref}})^2}$. The level of priority between i_{dref} and i_{qref} can significantly affect the BESS regulations on microgrid frequency and voltage

since the dynamic allocations of i_{dref} and i_{qref} within the current limit will determine the converter output real and reactive power in real-time.

One must realize that a stable real power transfer requires a well-established voltage. Therefore, this study use the reactive power/current priority mode as the default condition. However, it may be beneficial to switch to real power/current priority when the microgrid experiences prolonged over/under-frequency. This aspect particularly reflects in Chapter 5 where a power/current priority switch condition is proposed.

3.5 Chapter3 Summary

This chapter provided necessary background knowledge to understand and conduct this dissertation research by reviewing the fundamentals of microgrid stability, modeling and control. First, it established the context of the research via defining the studied microgrid frequency and voltage stability problems. Second, it explained the modeling concepts for microgrid network, loads, synchronous generators and BESS power converters. Third, it presented the synchronous generator governor/frequency control and excitor/voltage control methodologies. Finally, it discussed the overall power converter $current - mode\ control$ and clarified the BESS converter's controller priority mode settings regarding its real/reactive power/current capacity limitations during operation.

Chapter 4

Adaptive Frequency Regulation

Governor droop control is widely used in the power system for primary frequency control while achieving the load sharing among synchronous generators [15] followed by a slow acting secondary frequency control provided by automatic generation control (AGC) [121, 124]. This approach can create frequency regulation issues in fast changing microgrid systems with small rotational inertia [1].

To tackle such challenges, this chapter introduces an improved fast frequency regulation strategy that combines a PLL frequency measurement based adaptive nonlinear droop control with a fast simultaneous secondary control using BESS. In particular, this study sheds light on stability enhancement of microgrids with synchronous generator.

4.1 Microgrid System for Chapter 4

Figure 4.1 represents the studied system single-line diagram. It shows a $15\ kV$ class radial feeder connected to its upper $69\ kV$ utility grid ($X/R = 22.2$; 1000-MVA short-circuit capacity) through substation step-up transformer. These distribution system parameters were modified from [1, 114]. The line is divided by sections and protected by their dedi-

cated circuit breakers as numbered.

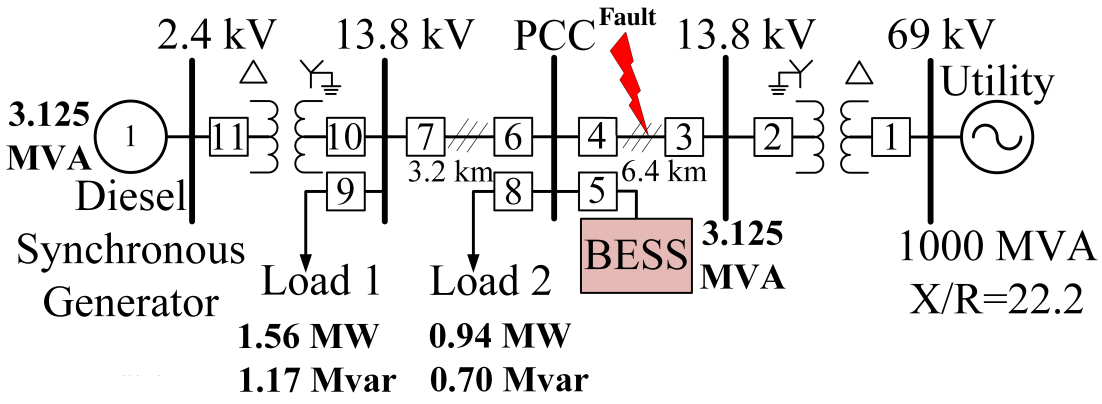

Figure 4.1: Single-Line diagram of the chapter 4's studied microgrid system

A 3.125 MVA diesel generator equipped with excitation and governor control system [125] is in operation at the feeder end. The governor has a droop setting: $R_s = 1\%$. Feeder loads are distributed along the main line with load $\#1 = 1.56\ MW\ and\ 1.17\ Mvar$ (50% diesel generator nameplate capacity, power factor 0.8 inductive) and load $\#2 = 0.94\ MW\ and\ 0.70\ Mvar$ (30% diesel generator nameplate capacity, power factor 0.8 inductive). A 3.125 MVA BESS is installed at the point of common coupling (PCC), capable of controlling its real and reactive power exchange through the hosted network by utilizing the PCC voltage phase angle information obtained from its PLL.

4.2 Adaptive Primary Nonlinear Droop Control

This and the following session describe the proposed adaptive fast frequency regulation strategy used in the BESS converter's power controller. All quantities are expressed in pu, with base values of $13.8\ kV$, $10\ MVA$ and $60Hz$.

Figure 4.2 shows the new proposed adaptive nonlinear droop control strategy. The block diagram is shown in Fig. 4.2(a). The converter nonlinear droop reference power P'_{ref1}:

$$
\begin{aligned}
P'_{ref1} &= K_A|f_0 - f_s|(f_0 - f_s) \\
&= K_A|\Delta f|\Delta f \\
&= K_P \Delta f
\end{aligned}
\tag{4.1}
$$

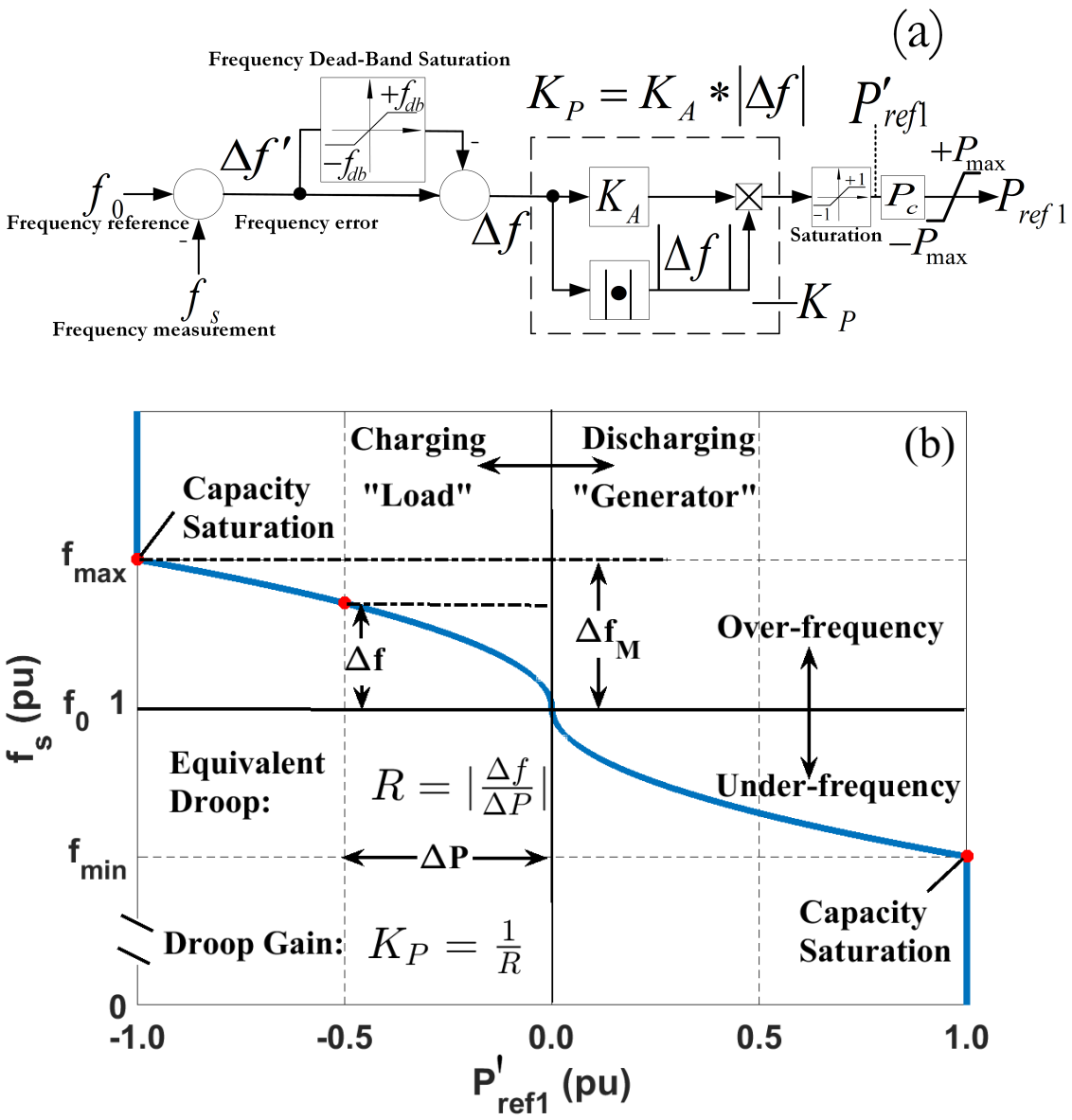

Figure 4.2: Adaptive Nonlinear Droop: (a) Block diagram, (b) Resultant Droop Curve

The $P_{ref1}^{'}$ is converted to P_{ref1} by:

$$P_{ref1} = P_{ref1}^{'} P_c \tag{4.2}$$

where:

P_c is the BESS rated power in pu under the system base.

There is also a real time power limit which is denoted by P_{max}:

$$P_{max} = \hat{V}_{PCC} I_{d_{max}} \tag{4.3}$$

Where $\hat{V}_{PCC}$ is the PCC voltage magnitude and $I_{d_{max}}$ is the maximum d axis current.

The droop gain K_P is expressed as:

$$K_P = K_A |\Delta f| \tag{4.4}$$

Equation (4.4) means that the droop gain is linearly proportional to the measured absolute value of frequency deviation $|\Delta f|$ from the converter PLL (after considering the dead-band frequency f_{db}). As a result, the converter output power (4.1) is proportional to the measured frequency deviation squared. Unlike the previous work [107], when the frequency is close to the nominal value, the droop gain of the converter's power control loop will be small, resulting in a smaller response compared to the traditional linear droop. Meanwhile, as the measured frequency deviation Δf is increasing, the converter power controller gain is ramping up rapidly, thus leading to a more significant power output. Such response helps to bring the microgrid frequency back to normal and the sensitivity of the frequency control is not sacrificed.

The variable droop control gain leads to a nonlinear droop curve, Fig. 4.2(b). The curve is plotted in generator reference, assuming a zero dead-band frequency (i.e., $f_{db} = 0$), with converter power on the $X - axis$ and PLL frequency estimation on the $Y - axis$.

This configuration results in a negative droop curve slope. When the power is positive, the converter is generating power output to its connected system as a generator. On the other side, when the power is negative, the converter acts like a load which absorbs power. At each point along the droop line, there is its equivalent droop $R = |\Delta f/\Delta P|$, defined in the same way as the traditional droop control. The equivalent droop is getting smaller as the absolute frequency deviation becoming larger, which is an indicator of a more sensitive converter frequency regulating response during high frequency deviation. Near the nominal frequency, the slope of the curve becomes infinite, corresponding to a zero droop gain $K_P = 1/R$.

The equivalent droop at the beginning of converter capacity saturation points (i.e., $f_s = f_{max}, P'_{ref1} = -1, P_{ref1} = -P_c$ or $f_s = f_{min}, P'_{ref1} = 1, P_{ref1} = P_c$) is defined as capacity saturation droop, R_c, expressed in precent:.

$$Perccent\ R_c = \sqrt{\frac{1}{K_A}} \times 100 = \Delta f_M \times 100 \tag{4.5}$$

where:

Δf_M: Maximum frequency deviation at the converter capacity saturation points, $\Delta f_M = f_{max} - f_0 = f_0 - f_{min}$.

It is straightforward to determine K_A by given R_c. The most important advantages of this nonlinear droop method is that it provides additional stability margin around the equilibrium point by dynamically changing the droop controller gain. It further avoids back and forth oscillations that yield possible instability that have been observed in systems using linear controllers when the frequency is close to the nominal value [88]. Furthermore, one may be able to achieve a smaller R_c without causing instability compared to the linear droop case to achieve better frequency regulation.

4.3 Simultaneous Fast Secondary Frequency Control

This section introduces a fast secondary integral controller with a very small time constant (sub-cycle). This is achieved by a fast converter control coupled with storage as the primary fuel source. In addition, the secondary controller is acting at the same time as the converter adaptive nonlinear droop control. Two probable approaches are presented in the following two subsections. The first method uses a fixed integral controller gain while the second strategy proposes an integral controller with adaptive gain.

4.3.1 Approach#1: Fixed Gain

If the fixed integral controller gain K_I is used, the complete power controller block diagram is shown in Fig. 4.3.

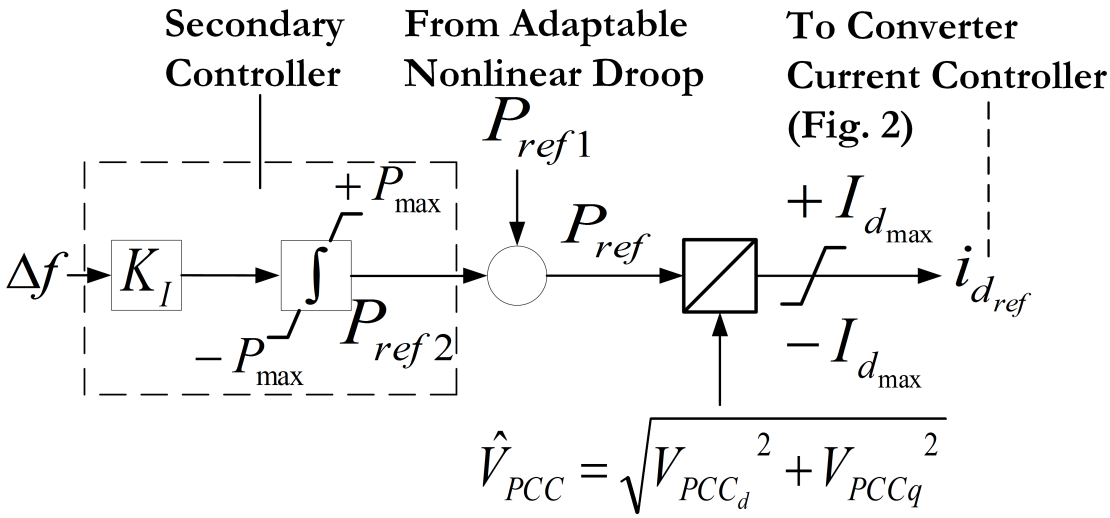

Figure 4.3: Converter Frequency Regulator Block Diagram

The final converter power reference P_{ref} is the sum of both power references from primary adaptive nonlinear droop P_{ref1} and secondary controller P_{ref2}:

$$P_{ref} = P_{ref1} + P_{ref2} = K_A|\Delta f|\Delta f P_c + \int_0^t K_I \Delta f dt \tag{4.6}$$

This method brings the benefit of both sensitive primary control and fast secondary integral control together. For instance, with a sudden frequency deviation, the adaptive droop control will first change converter power based on the nonlinear droop curve. Meanwhile, the secondary controller quickly integrates the frequency errors and provide an additional control signal to move the power set point at the nonlinear droop curve for a new system equilibrium with zero frequency error just like the traditional AGC [121], however much faster. In the end, one has the ability to use converter based generators for regulating the isolated microgrid frequency around its nominal value under the dynamic changing system conditions.

4.3.2 Approach#2: Adaptive Gain

The secondary gain can also be adaptive using the same idea from the previous presented adaptive nonlinear droop control with the following modified block diagram, Fig. 4.4:

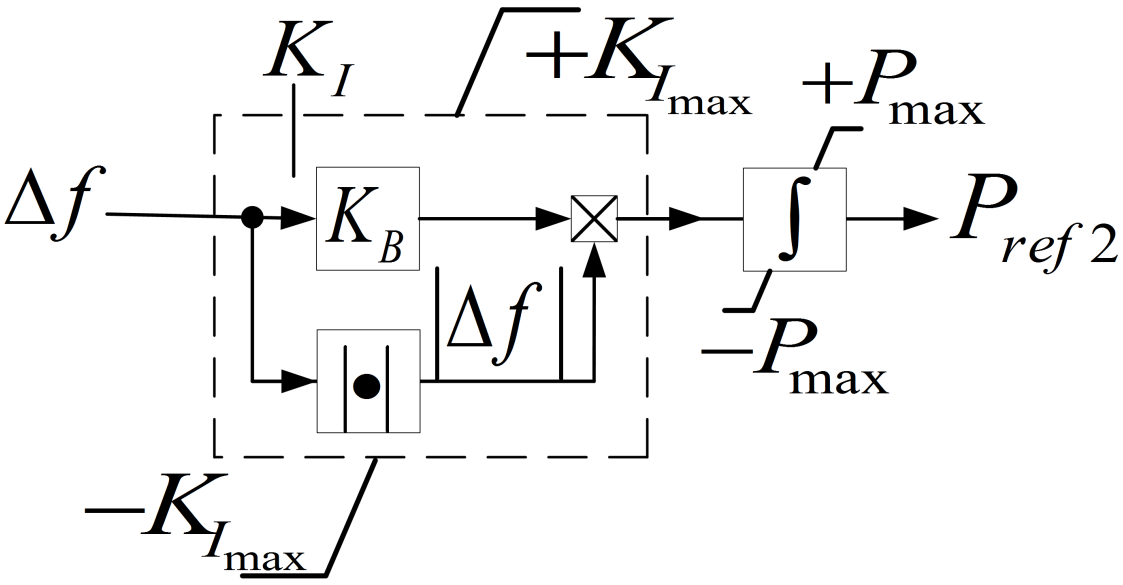

Figure 4.4: Adaptive Secondary Frequency Controller Block Diagram

The expression for the integral gain is:

$$K_I = K_B|\Delta f| \tag{4.7}$$

An excessive secondary control may also lead to undesirable frequency oscillation in the power system [126]. This adaptive secondary control addresses such concern by dynamically changing its integral controller gain K_I. Equation (4.7) means that the secondary integral gain K_I is linearly proportional to the measured absolute value of frequency deviation $|\Delta f|$ from the converter PLL. As the results,the converter will have a large K_I while the $|\Delta f|$ is big. This contributes a quick integration of the frequency error for the needed secondary power reference P_{ref2} and hence also a more aggressive frequency regulation action. Meanwhile, the K_I is small when the system frequency is close to its nominal value. This leads to a much milder response and a better stability margin comparing to an integral controller with a fixed gain.

The value for K_B can be determined by the desired K_I value at a specific $|\Delta f|$. It is often desirable to set a limit $K_{I_{max}}$ as the maximum allowable value of K_I to further avoid the excessive control action. The case study on impacts of adaptive K_I gain on the stability of the converter controller is given in Ch. 6.2.1.

4.4 Cases Studies

To examine the effectiveness of the adaptive storage control on microgrid operation, a fault induced islanding event is conducted in MATLAB® Simulink® model for the studied microgrid system shown in Fig. 4.1. It should be noted that since this chapter is dedicated to frequency regulation strategy, the PCC voltage regulation scheme is adopted from [49]. Prior to the fault, the system works in the steady state with local load $\#1$ in service and load $\#2$ disconnected. The BESS is in the standby mode, connected to the PCC and synchronized to the host utility by its PLL. The diesel synchronous generator

generates 2.5 MW (80% of its nameplate capacity) to the grid. At $t = 0.55\ s$, a permanent three phase-fault strikes on the feeder between circuit breaker $\#3$ and $\#4$. At $t = 0.6\ s$, 3 cycles after the fault, abnormal conditions are detected and the BESS starts to activate its converter for voltage and frequency regulation. The fault is cleared by opening breakers $\#3$ and $\#4$ at $t = 0.63\ s$, 5 cycles after the fault. As a result, part of the distribution system functions as a microgrid at the downstream of the PCC. The microgrid is in autonomous operation after the islanding. Finally, at $t = 1.5\ s$, the load $\#2$ is energized.

4.4.1 Case#A: Unstable BESS operation with linear droop

Figures 4.5 and 4.7 illustrate the unstable BESS performance for a linear droop control with $f_{db} = 6 \times 10^{-4}\ pu\ (36\ mHz)$, $R_c = 1\%$ and secondary controller with a fix gain of 1000. The estimated PLL frequency f_s in Hz is plotted in Fig. 4.5. The overall f_s unstable response versus time is shown in Fig. 4.5(a). Meanwhile, Fig. 4.5(b) and 4.5(c) present the magnified f_s oscillogram for $0.67 < t < 0.71\ s$ and $1.48 < t < 1.52\ s$. Fig. 4.5(a) reveals a significant frequency excursion during the fault ($0.55 < t < 0.63\ s$) and subsequent islanding transients. The f_s returns to near the nominal value around $t = 0.67\ s$ as shown in Fig. 4.5(b). It is also illustrated that the $R_c = 1\%$ of linear droop leads to an unstable oscillation of f_s centering around base frequency ($60Hz$), with oscillating frequency higher than 400 Hz, thus resulting in poor voltage supply quality, Fig. 4.6. The load $\#2$ switching in at $t = 1.5\ s$ leads f_s unstable oscillation to swing in Fig. 4.5(c).

Figure 4.7 presents the BESS power versus time. From here it can be learned that the unstable controller leads to the inadmissable power fluctuation. Before the load $\#2$ is switched on at $t = 1.5\ s$, the mean value of BESS power is negative, indicating its

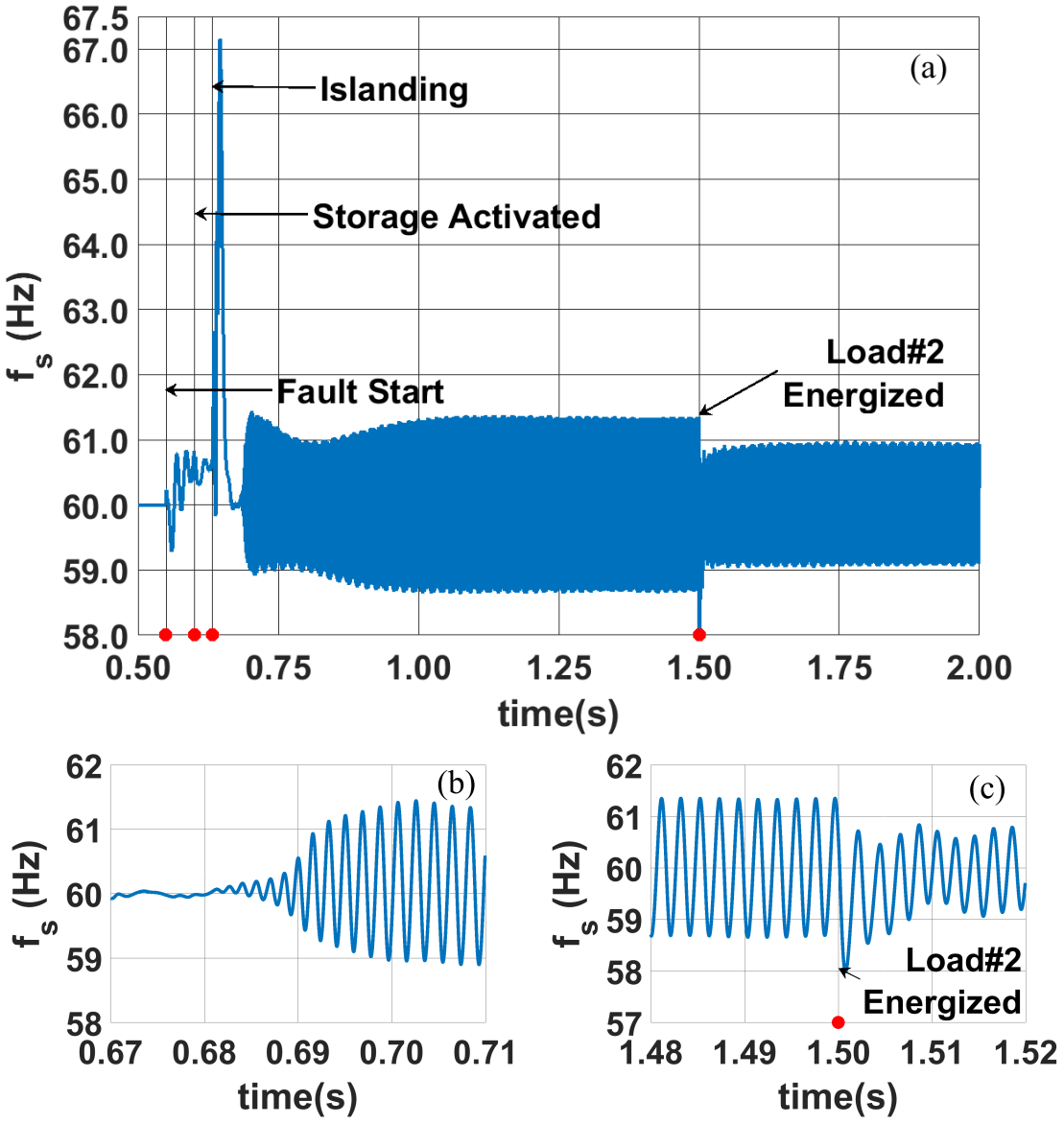

Figure 4.5: Estimated PLL frequency f_s for linear droop with $R_c = 1\%$ and secondary controller gain of 1000: (a). Overall unstable response, (b). Magnified oscillogram for $0.67 < t < 0.71s$, (c). Magnified oscillogram for $1.48 < t < 1.52s$.

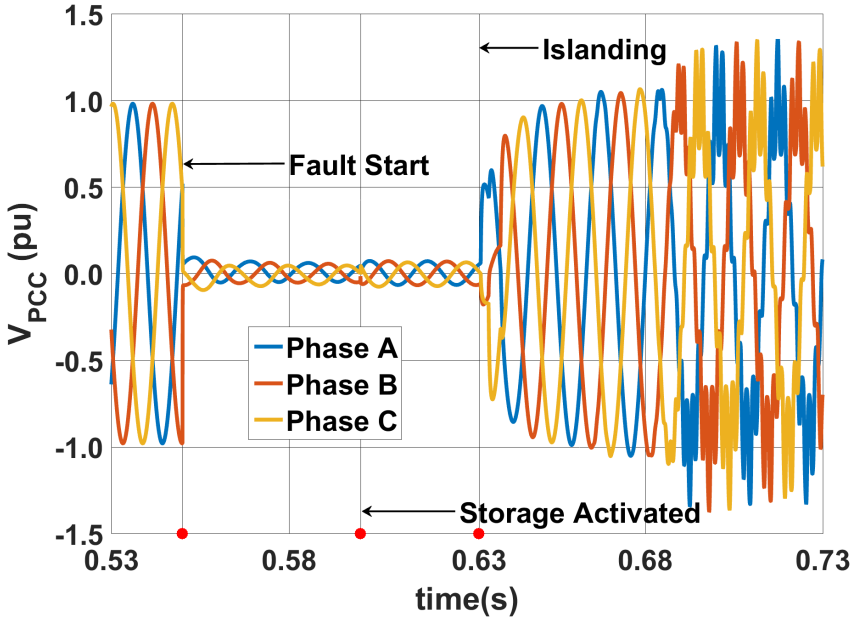

Figure 4.6: Magnified PCC voltage oscillogram vs. time: for $0.53 < t < 0.73s$, inadmissible waveform quality for linear droop with $R_c = 1\%$ and secondary controller gain of 1000.

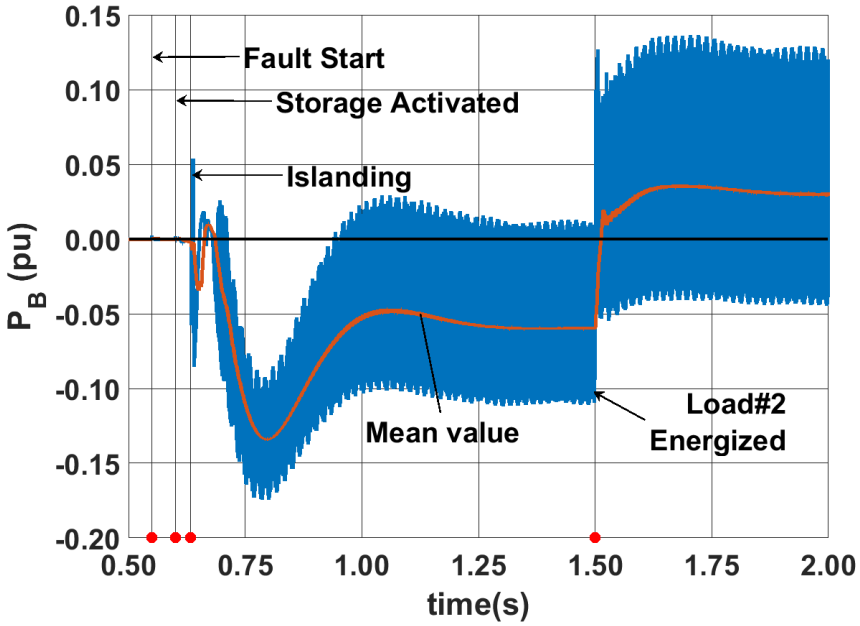

Figure 4.7: Unstable control performance: The BESS power vs. time for linear droop with $R_c = 1\%$ and secondary controller gain of 1000.

charging mode. Afterward, the mean power is positive, showing the BESS discharging as a generator. Nevertheless, the $R_c = 1\%$ linear droop cause the BESS power controller to be unstable.

4.4.2 Case#B: Stable BESS operation with nonlinear droop

In this second case study, the linear droop is replaced with an adaptive droop control under the same $f_{db} = 6 \times 10^{-4}\ pu\ (36\ mHz)$, $R_c = 1\%$ and secondary controller with a fix gain of 1000. The responses of the BESS and the system performance, both with and without BESS, are summarized in Figs. 4.8 to 4.12.

Figure 4.8 shows the converter PLL estimated frequency f_s under adaptive nonlinear droop control. Compared with previous case shown in Fig. 4.5(a), it is learned that the PLL remains stable and f_s quickly returns to 60 Hz with the help of the BESS. Despite the load $\#2$ switching on at $t = 1.5\ s$, the PLL returns to normal operation after a short disturbance.

The BESS power oscillogram is presented in Fig. 4.9. One will observe a stable control performance of the BESS power controller. The power ramps up from negative as a load to positive as a generator at $t = 1.5\ s$ to support the new load $\#2$ in service. It indicates that the proposed controller has the ability to quickly follow the load change. Looking at both Fig. 4.7 and 4.9, it also reveals that the BESS power under adaptive nonlinear droop control is a replica of the mean value of BESS power under linear droop control. This adaptive control preserves the sensitivity of the regulation without causing controller instability.

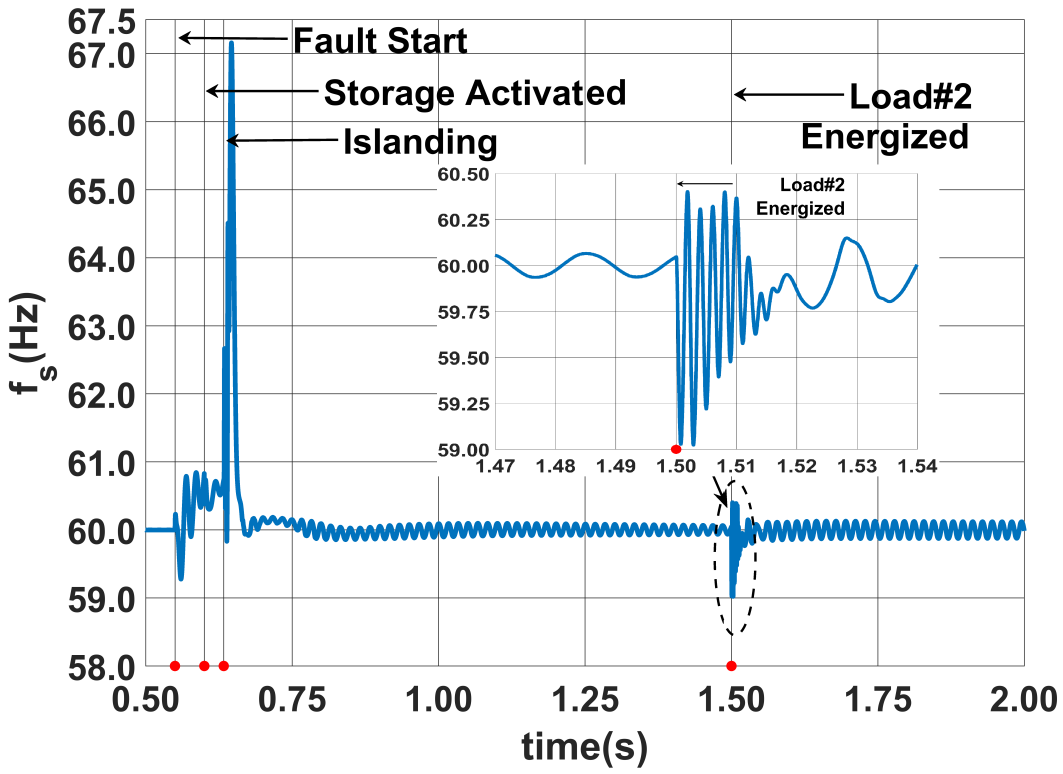

Figure 4.8: Estimated PLL frequency f_s for adaptive nonlinear droop with $R_c = 1\%$ and secondary controller gain of 1000.

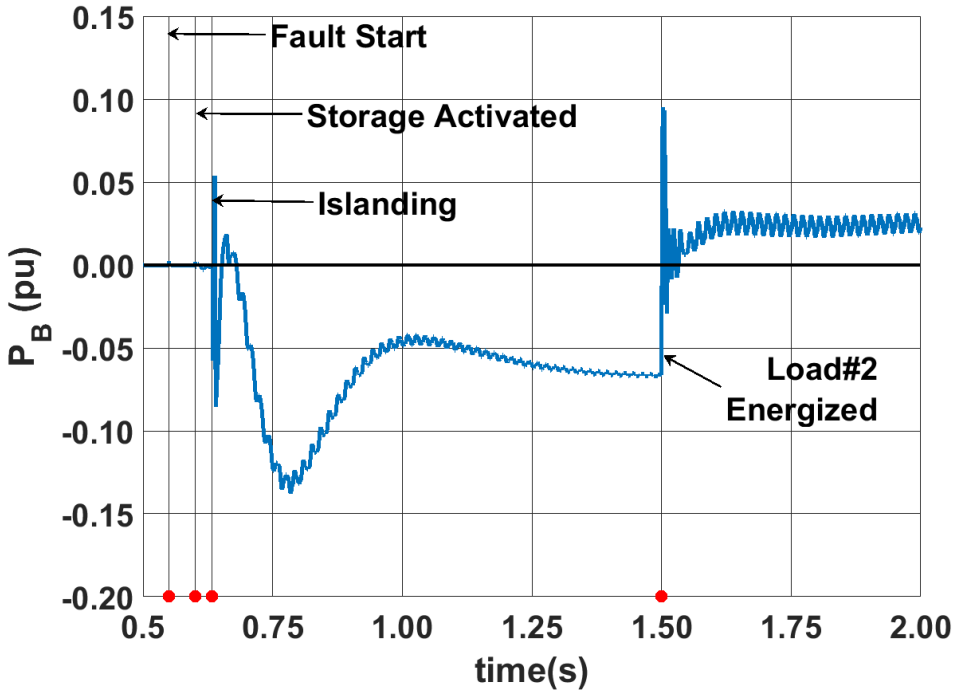

Figure 4.9: Stable control performance: The BESS power vs. time for adaptive nonlinear droop with $R_c = 1\%$ and secondary control gain of 1000.

The PCC voltage $d-q$ components are compared in Fig. 4.10 for cases with adaptive BESS control and without BESS. Excursions are observed at the switching instant, $t = 1.5\ s$, for both d and q axis components. In the case with BESS, the voltage $d-$axis component recovers to 5% of its nominal value after the fault induced islanding event almost 100 times quicker than the case without the BESS. The new load $\#2$ energized at $t = 1.5\ s$ causes prolonged low voltage sags for the case without the BESS. With the BESS contribution, after a brief disturbance at $t = 1.5\ s$, the PCC voltage immediately returns to normal.

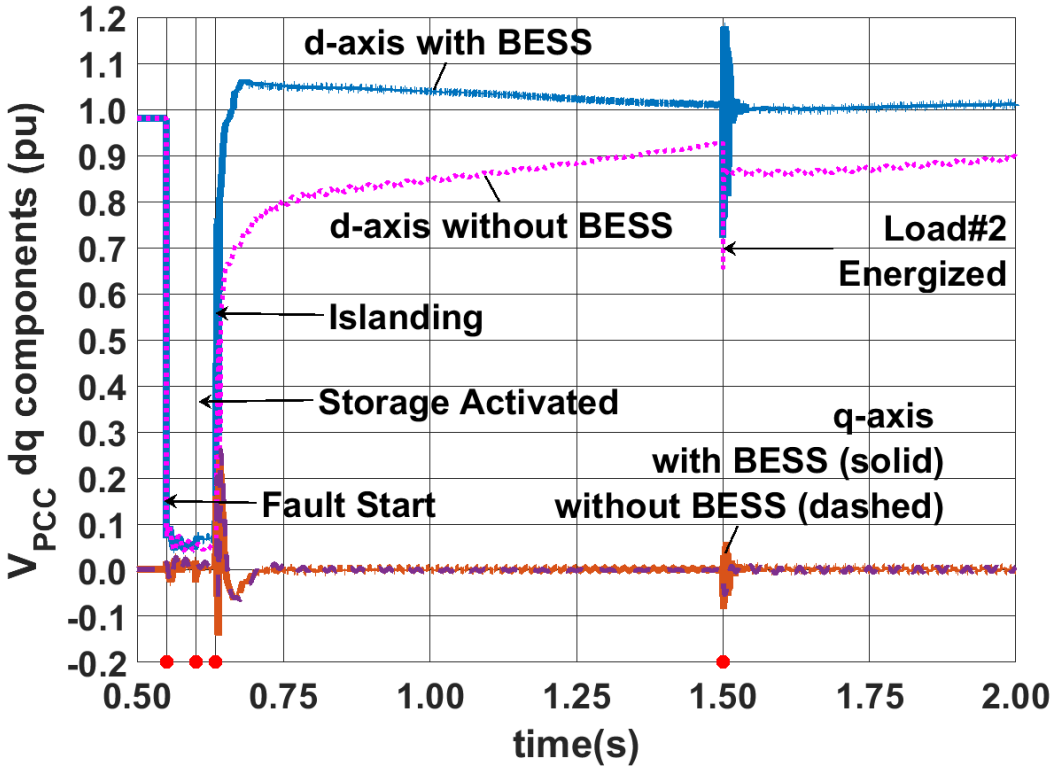

Figure 4.10: PCC voltage dq components vs. time with and without BESS adaptive control

Figure 4.11 depicts the magnified PCC voltage oscillograms versus the time with and without BESS. Fig. 4.11(a) and 4.11(c) compare the system performance with and without BESS before, during and after the fault for $0.53 < t < 0.73$ s. It is shown that in Fig. 4.11(a), the voltage returns within 5% of its nominal value within 1 cycle after the islanding. Conversely, the voltage without the BESS stays below 0.8 pu during first 5 cycles after the islanding. The impacts of load $\#2$ switching in at $t = 1.5$ s is shown in Fig. 4.11(b) and 4.11(d). In Fig. 4.11(b), thanks to BESS performance, the voltage returns to nominal value within 1 cycle. Without BESS, the additional loading causes the obvious voltage sags, Fig. 4.11(d).

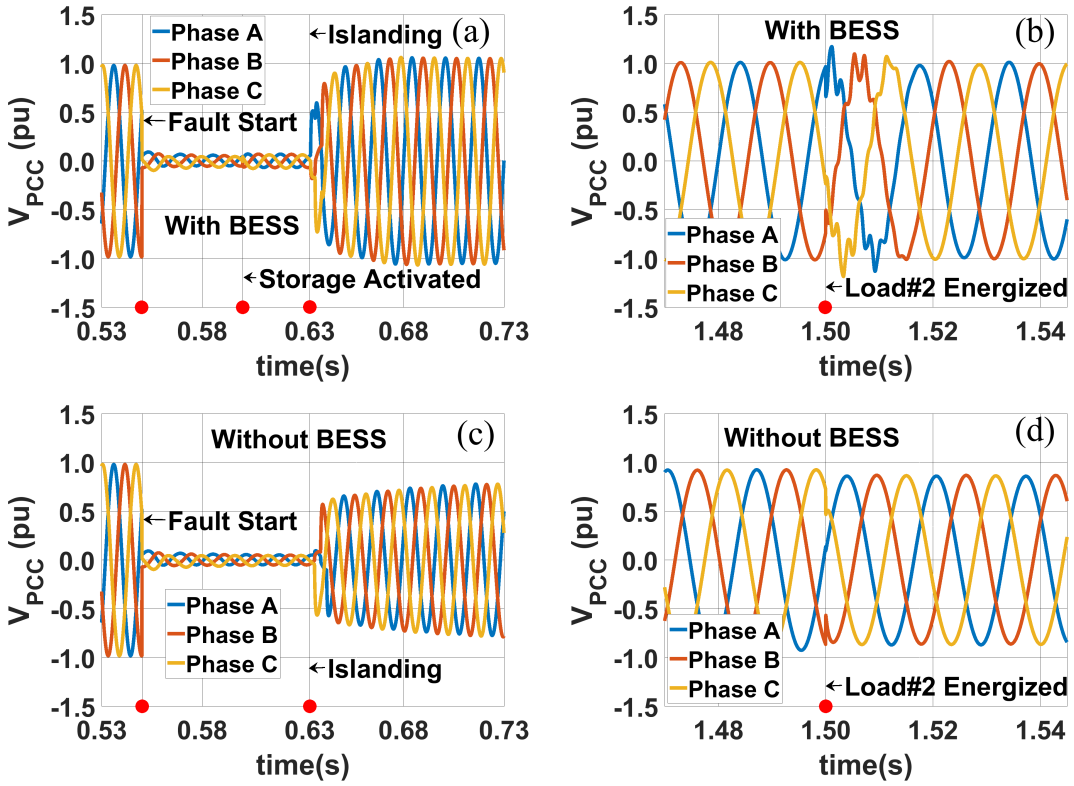

Figure 4.11: Magnified PCC voltage oscillogram vs. time: (a). With BESS adaptive control, for $0.53 < t < 0.73s$, (b). With BESS adaptive control, for load#2 switched in at $t = 1.5s$, (c). Without BESS, for $0.53 < t < 0.73s$, (d). Without BESS, for load#2 switched in at $t = 1.5s$.

Finally in Fig. 4.12, the distributed synchronous generator rotor speed is compared with and without BESS. The three-phase fault causes a severe generator speed excursion that measured over 1 Hz before clearing. With the BESS adaptive control, the rotor frequency quickly returns to 60 Hz within 0.5 s after the islanding. Even with a large load #2 (30% of the generator nameplate) when switching on at $t = 1.5s$, the generator speed varies less than 0.1 Hz when the BESS is used. Without the BESS, the alternator takes considerably longer to regulate its speed despite a fast acting diesel unit in service with a $R_s = 1\%$ droop. Moreover, the additional load #2 leads to a speed change of

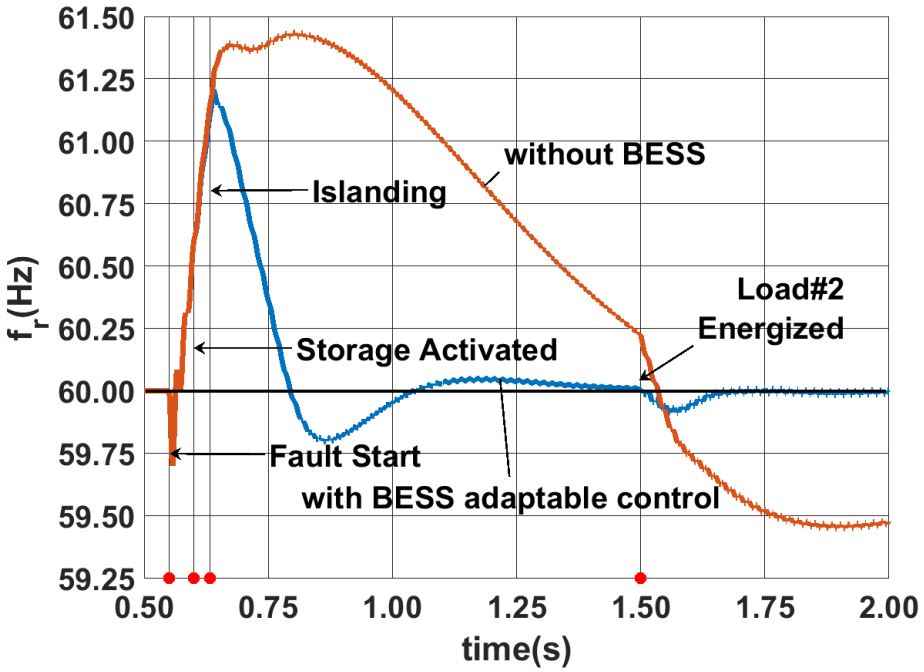

Figure 4.12: Synchronous generator rotor frequency f_r with and without BESS adaptive control

more than 0.75 Hz. All of the above results demonstrate the superior performance of the proposed adaptive energy storage control method.

4.5 Chapter4 Summary

It has been demonstrated that with the droop gain depending on the PLL frequency estimation, the adaptive nonlinear droop control gains additional stability margin over the traditional linear droop control by its flexibility. Moreover, this chapter highlights the operational benefits of adaptably controlling the BESS on the frequency stability enhancement of the microgrid.

Chapter 5

Adaptive Voltage Regulation

This report extends the previous chapter 4's solution [127,128] by describing a new adaptive voltage regulation strategy that goes hand in hand with IM speed recovery after the islanding. The specific contributions of this advocated adaptive voltage regulation approach are:

1. An increase in the microgrid motor's probability of riding-through the fault-induced islanding even under high load torque with prolonged fault clearing time, thereby increasing the maximum permissible fault cleaning time while assuring that the islanded microgrid motors' speeds recover.

2. Provision for an autonomous control strategy, with no additional sensors and monitoring systems needed to achieve the benefits for the IMs.

3. Capability for modifications with a broad adaptability into various power system configurations based on the required standards [5].

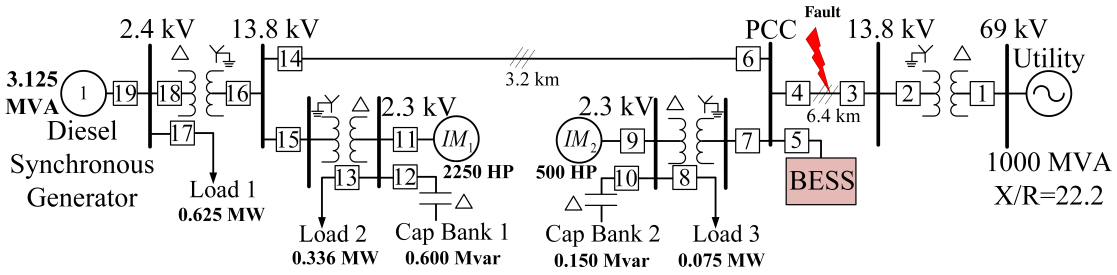

Figure 5.1: Single-Line diagram of the chapter 5's studied system

5.1 Microgrid System for Chapter 5

Figure 5.1 represents the studied system single-line diagram. It shows a 15 kV class radial distribution feeder connected to 69 kV utility source ($X/R = 22.2$; 1000-MVA short-circuit capacity) via a substation step-up transformer. These distribution system parameters (see Appendix I) were adapted from [1, 114]. The loadings of the feeder are mixed with both linear RLC impedance and IM loads. There are two 2.3 kV IMs [117], connected to the 13.8 kV feeder through their transformers; a large unit with 2250 HP rated power and a smaller motor with 500 HP rated power.

A 3.125 MVA diesel generator equipped with excitation and governor control system [125] is in operation at the feeder end. The governor has a droop setting of 1%. A BESS is installed at the PCC for both frequency and voltage regulation. The feeder is sectionized by its dedicated circuit breakers as numbered. It is assumed that a fault happened between the circuit breaker #3 and #4 leading to fault-induced islanding. These system settings capture the essential features of an autonomous microgrid with multiple IM sizes. This topology enables one to test the performance, verify the concept and conduct sensitivity studies for the proposed adaptive voltage regulation strategy without loss of generality.

5.2 Induction Motor (IM) loads Impacts on Microgrid Dynamics and Stability

It has been learned that load characteristics have significant impacts on the dynamics and the stability of a microgrid [129]. The extensive use of IMs, and their nonlinear transient behavior have triggered special interest [7]. During the low voltage condition caused by the fault, the microgrid IMs may begin to stall and consume excessive reactive power before tripping off, which leads to fault induced delayed voltage recovery (FIDVR) or even voltage collapse [130]. It is essential for a truly reliable microgrid to be able to achieve a successful motor fault ride-through under a broad range of conditions. Previously, several approaches have been proposed in order to avoid motor stalling after the fault-induced islanding [7, 131]. For example, [131] utilizes dynamic inverter frequency settings inside an inverter based microgrid that are meant to increase the motor torque at a low speed. The study in this chapter also focuses on the microgrid voltage stability issue caused by the IM stalling.

5.3 Concept

Figure 5.2 shows the one-line diagrams of a 2250 HP IM connected to a stiff voltage source V_s either directly or through a step-down transformer (8% short circuit reactance). The machine parameters are taken from [117].

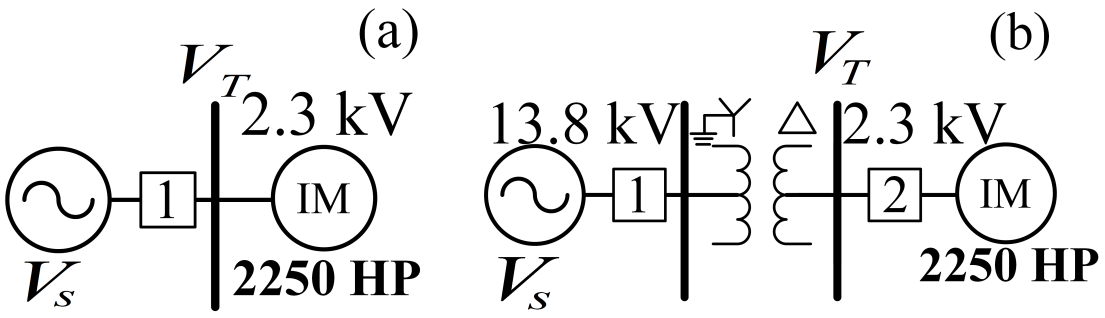

Figure 5.2: Induction motor free accelerating experiment single-line diagram: (a). Direct start, (b). With step-down transformer.

The idea behind utilizing adaptive voltage regulation to enhance the IM fault ride-through can be illustrated by simulating the IM free acceleration experiments under the two configurations shown in Fig. 5.2. Fig. 5.3 plots the free acceleration characteristics of the motor under $0.8 < V_s < 1.2\ pu$ with either direct connection, Fig. 5.2(a), or use of a transformer, Fig. 5.2(b). It illustrates the impacts of supply voltage V_s magnitude on the IM transient torque-speed curves. It is evident that when the IM is equipped with a transformer, the motor operates with a lower terminal input voltage V_T and the developed electromechanical torque is less. For stable motor operation with a constant torque load T_M equal to its rated torque T_r, it is necessary for the breakdown torque $T_p > T_M = T_r$ to result in two equilibrium points. The left equilibrium point with a positive torque-speed curve slope is unstable while the right point is stable with a negative slope. Since the torque of the machine is proportional to the magnitude squared of its stator terminal voltage V_T [116], both T_p and the speed range in between the two equilibrium points are reduced significantly with a reduced V_s magnitude. The above observations indicate that the motor is prone to be disconnected under a high torque load and low supply voltage,

especially with a transformer connection. With a supply voltage $V_s > 1.0\ pu$, the motor will have higher electromechanical torque T_e at a lower speed, resulting in a higher stability margin, Fig. 5.3.

When there is a small dip in the microgrid motor terminal voltage V_T, the motor may be able to slow slightly until reaching a new stable equilibrium point at a lower voltage and speed without stalling. However, under the power system fault, the terminal voltage of the IM can experience a severe sag. This condition may lead to $T_p < T_M$, and hence a continuing decline of the motor speed. The speed reduction rate is dependent on the unbalance level between T_e and T_M, which is affected by the fault types, clearing speed, as well as, the motor inertia and loading. If V_s cannot recover sufficiently in order to develop a $T_e > T_M$, the motor will be tripped [110].

In reality, the motor supply voltage V_s has a short circuit source impedance Z_s. Similar to the transformer impedance effects in Fig. 5.2(b), the excessive reactive power consumed by the IM at a low speed will result in a large current flow and inadmissible voltage drop across Z_s. Nevertheless, if one can regulate the post-islanding $V_s > 1.0\ pu$ for a time even as brief as a few cycles, it will boost the voltage across the motor terminals. This higher V_T will contribute to a higher electromechanical torque $T_e > T_M$ during the low speed condition that may permit a successful disturbance ride-through. An illustrative case is given in Fig. 5.4. It plots four torque-speed characteristics of an IM under terminal voltage V_T of different magnitudes.

Assuming that the motor carries a full load torque $T_M = T_r$, it will operate at the intersection of curve 1 and load torque within the stable region during normal operation. If a fault happens near the motor terminal, its V_T will experience a severe sag and the motor will operate under the curve 2. With $T_p < T_M$, the motor speed will decline. Under the post-fault recovery voltage $\#1$, curve 3, the IM can recover before its speed reaching S_{u_1}. Curve 4 is under the post-fault recovery voltage $\#2$ with a higher magnitude and the

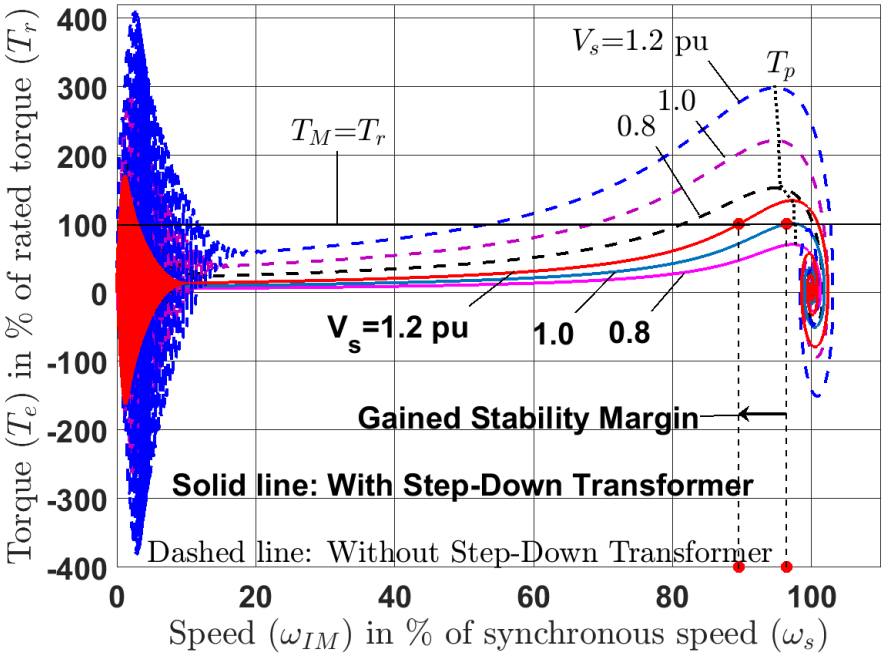

Figure 5.3: Induction motor free accelerating torque-speed curves

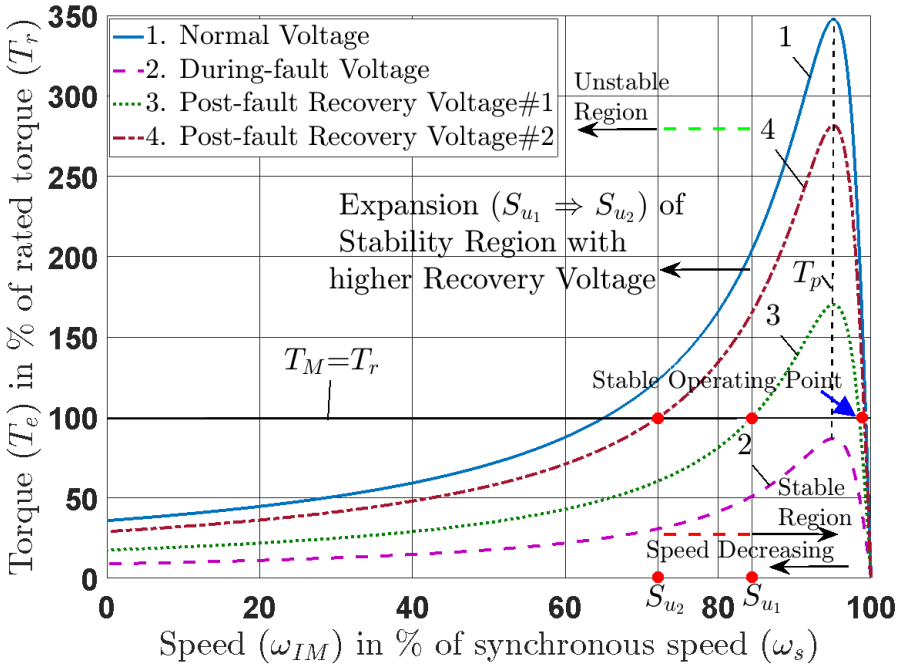

Figure 5.4: Torque-speed characteristics for an induction motor under different terminal voltage V_T

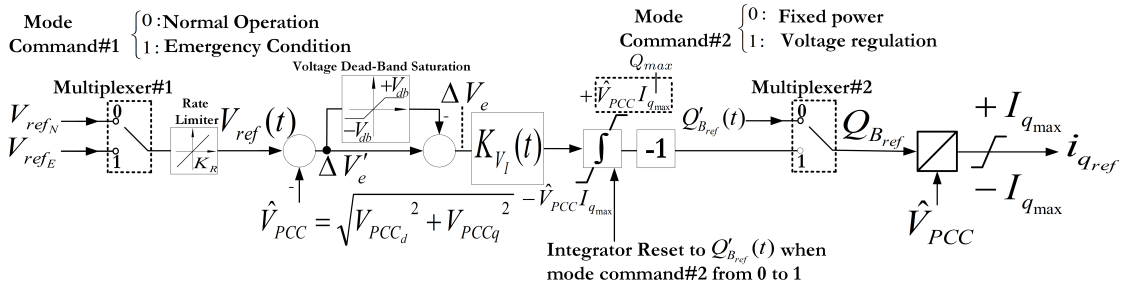

Figure 5.5: BESS PCC voltage regulator

developed electromechanical torque. Thanks to this higher voltage, the motor can recover before reaching to the S_{u_2} with a longer fault clearing time. This case shows that it is feasible to gain additional stability margin by adaptively regulating a higher post-fault V_T which is the incentive of proposed adaptive voltage regulation methodology.

This concept requires additional resources that can provide a large and rapid dynamic reactive current support. The traditional synchronous generator excitation control for voltage regulation is slow and thus is not suitable for this task [122]. Luckily, with a fast $current - mode\ control$ ability [49], the BESS converter is an ideal candidate for this type of voltage support. By helping both voltage recovery and IM speed recovery, this concept improves the stability as well as the resiliency of the overall microgrid.

5.4 Implementation

Figure 5.5 shows the block diagram of the BESS PCC voltage controller. All quantities are expressed in pu, with base values of $13.8\ kV$, $10\ MVA$ and $60Hz$.

The proposed adaptable voltage regulation strategy is implemented by setting the BESS voltage reference point $V_{ref}(t) > 1.0\ pu$ following the fault induced islanding. The converter will act like an over-excited synchronous machine, with much quicker reaction time, supplying dynamic reactive current/power to its PCC within its current rating.

5.4.1 Algorithm for adaptive voltage regulation set point: $V_{ref}(t)$

The BESS is operated under reactive power priority mode with two possible operating states: normal or emergency. The algorithm for determining the $V_{ref}(t)$, based on the previously described adaptive voltage regulation concept can be summarized in Fig. 5.6. During the normal operation when the PCC voltage magnitude $\hat{V}_{PCC} > V_{th_L}$, the PCC voltage regulator reference $V_{ref}(t)$ stays at V_{ref_N} (usually $V_{ref_N} = 1.0\ pu$) as the normal operation mode. If the $\hat{V}_{PCC} < V_{th_L}$, the regulator will switch to emergency mode and the $V_{ref}(t)$ will ramp up at a rate of K_R to V_{ref_E}, a value higher than V_{ref_N}. Then the BESS converter will inject reactive current/power within its current limit (i.e., $i_{q_{ref}} \leq I_{q_{max}} = I_{max}$; $Q_{max} = \hat{V}_{PCC} I_{q_{max}}$) to regulate PCC voltage toward V_{ref_E}. To avoid the excessive over-voltage condition caused by this operation, the algorithm will ramp down the $V_{ref}(t)$ as soon as the PCC voltage magnitude hits an upper threshold, $\hat{V}_{PCC} \geq V_{th_H}$ with $V_{ref_N} < V_{th_H} \leq V_{ref_E}$. It should also be noted that the algorithm must carefully take the system standards [5,132] and motor protection schemes [133,134] into consideration so that the actual over voltage duration is permissible (i.e., not triggering unwanted protections or sacrificing motor performance and life [135]). Moreover, the $V_{ref}(t)$ will ramp back down to V_{ref_N} at the rate of K_R if at least one of the following three conditions is true so that the BESS inverter capacity can be utilized for frequency regulation:

1. Insufficient capacity for over-excitation: $\hat{V}_{PCC} < (V_{ref_N} - V_{db})$ for a time duration t_{rs_1}, where V_{db} is the voltage regulator deadband.

2. Capacity saturation around normal voltage reference: $\hat{i}_{ref} \geq I_{sat}$ and $|\hat{V}_{PCC} - V_{ref_N}| \leq V_{db}$ for a time duration t_{rs_2}, where $\hat{i}_{ref} = \sqrt{(i_{d_{ref}})^2 + (i_{q_{ref}})^2}$ and $I_{sat} \leq I_{max}$.

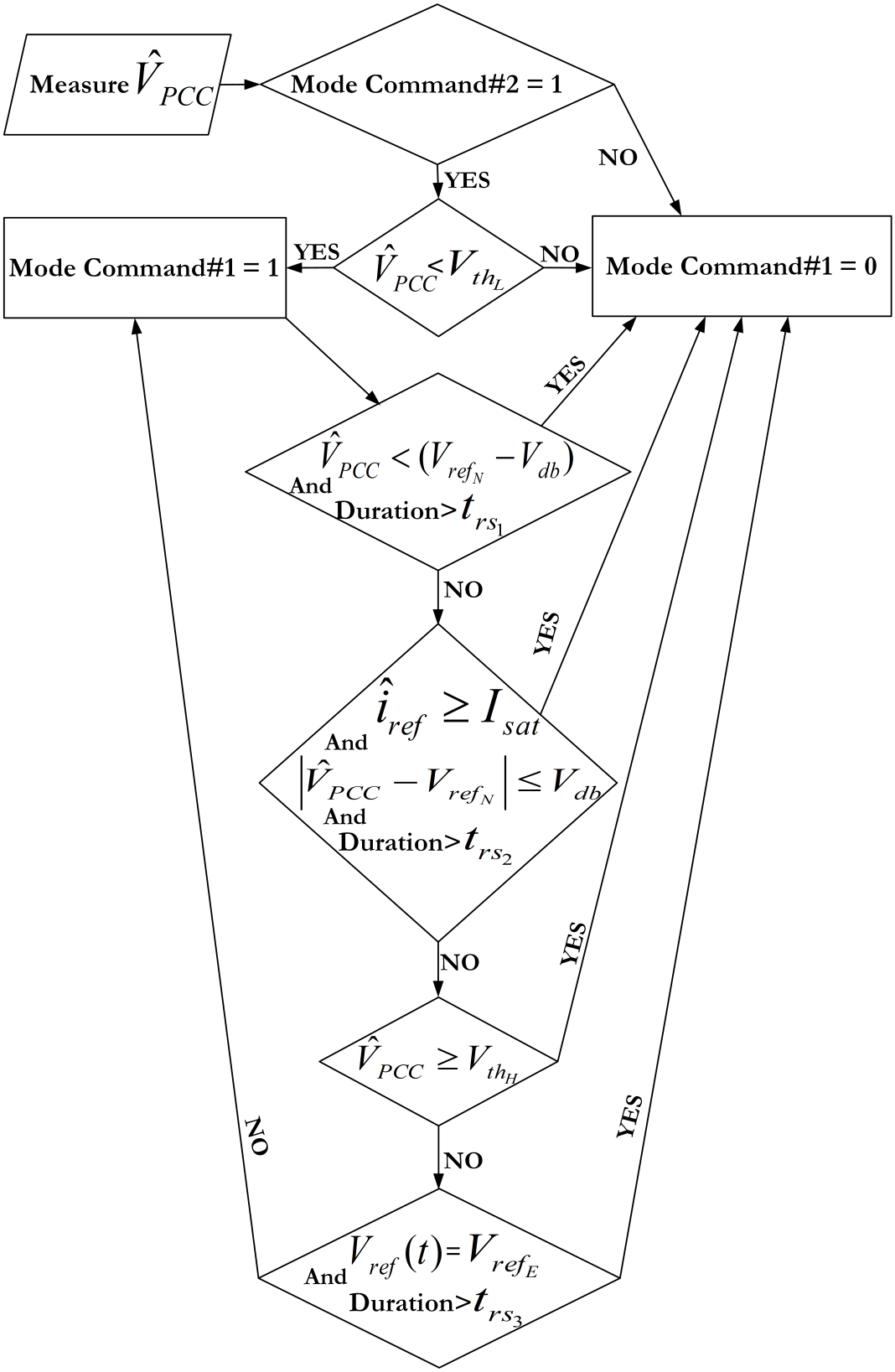

Figure 5.6: $V_{ref}(t)$ operating state decision tree

3. Insufficient capacity for a successful PCC voltage regulation to V_{th_H}: $V_{ref}(t) = V_{ref_E}$ but $\hat{V}_{PCC} < V_{th_H}$ for a time duration t_{rs_3}.

Considering the excessive amount of reactive power required by the IMs at a reduced speed, the current capacity of the BESS converter may not even be large enough for a pumped PCC voltage regulation to a value greater than V_{ref_N}. The condition 1 accounts for such situation and adaptably ramps down the $V_{ref}(t)$. Meanwhile, it does not conflict with the contributions that a BESS converter can bring for the voltage recovery and IM speed recovery since the converter has already utilized all its capacity for the microgrid stability enhancement.

The condition 2 is mainly caused by probable different voltage regulation references among the generator units in the system and thus the incentive for ramping down the $V_{ref}(t)$ under such case is for a better voltage control co-ordination among the power system apparatuses inside the microgrid.

Despite the fact that the capacity of the converter may be large enough to successfully regulate $\hat{V}_{PCC} > V_{ref_N}$ following the disturbance, it may still not be capable to contribute to $\hat{V}_{PCC} > V_{ref_H}$ in a timely manner, therefore it is appropriate to also return the $V_{ref}(t)$ back to V_{ref_N} for a better microgrid voltage profile as indicated in condition 3.

It is worth emphasizing again that this proposed adaptive autonomous voltage regulation strategy is for a rapid microgrid stability enhancement accounting the IMs speed recovery. It does not fully address the optimization issues related to reactive power reserve which traditionally disposed by many centralized voltage control methods that require communications and hence also a longer regulation time [136].

Finally, even through it is feasible to also change the voltage regulator gain $K_{V_I}(t)$ during the control for a more robust action against possible controller instability, this work uses a fixed gain: $K_{V_I} = 420$, determined by the design method promoted in [49].

5.4.2 Alternative: With Regulation Delays and Power Priority Switch

The previous algorithm for $V_{ref}(t)$ determines that the $V_{ref}(t)$ will ramp up from V_{ref_N} to V_{ref_E} whenever the $\hat{V}_{PCC} < V_{th_L}$. Similarly, $V_{ref}(t)$ will ramp down from V_{ref_E} to V_{ref_N} whenever the $\hat{V}_{PCC} \geq V_{th_H}$. Moreover, the converter is assumed to operate under reactive power priority mode. This section introduces an alternative approach that accounts the voltage regulation delays and power priority switch that could have profound impacts on the operations of the BESS and hence the real-time microgrid dynamics.

Fig. 5.7 shows this alternative $V_{ref}(t)$ algorithm. The following new conditions are implemented:

1. Voltage regulation delay $\#1$, t_{rd_1}: The voltage regulator will switch to emergency mode and ramp up $V_{ref}(t)$ at a rate of K_R from V_{ref_N} to V_{ref_E} only after $\hat{V}_{PCC} < V_{th_L}$ for an aggregate of more than t_{rd_1} s.

2. Voltage regulation delay $\#2$, t_{rd_2}: The voltage regulator will return to normal mode and ramp down $V_{ref}(t)$ at a rate of K_R from V_{ref_E} to V_{ref_N} only after $\hat{V}_{PCC} \geq V_{th_H}$ for an aggregate of more than t_{rd_2} s.

3. Power Priority Switch: The converter will switch from reactive power priority mode to real power priority mode and subsequently set voltage regulator to normal operation mode when $\hat{i}_{ref} \geq I_{sat}$ and $|\Delta f^{'}| \geq f_{sw}$ for an aggregate of more than t_{sw_1} s, where $\Delta f^{'} = f_0 - f_s$ and f_{sw} is the frequency deviation threshold value based on the standards.

The incentive for the new voltage regulation delays, t_{rd_1} and t_{rd_2}, is to avoid unnecessary mode switching for the voltage regulator. The voltage reference doesn't need to ramp up high when the voltage sag duration is short and hence the normal voltage regulation could have already contributed to a successful IM recovery. It could also be helpful

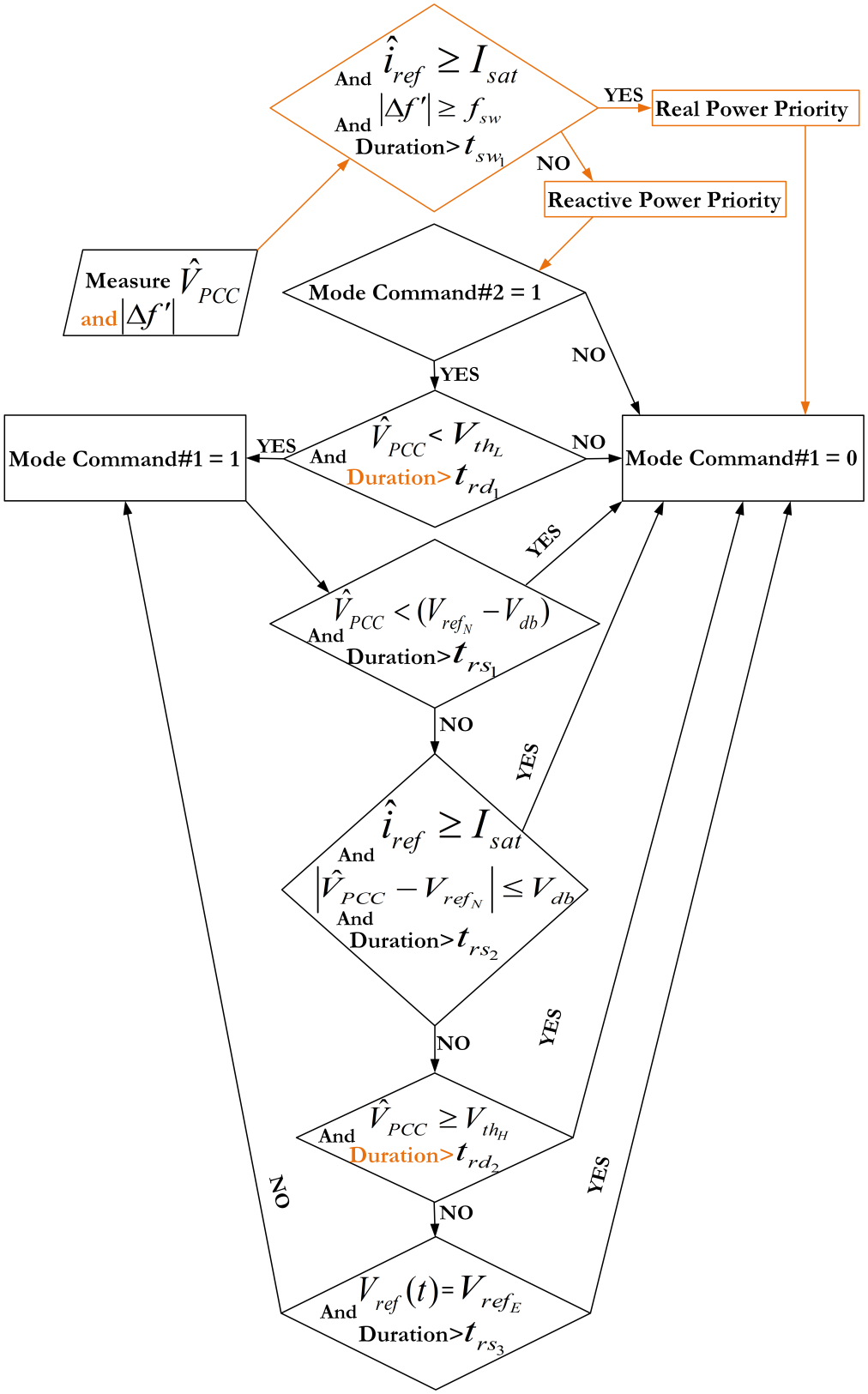

Figure 5.7: The alternative $V_{ref}(t)$ decision tree

for $V_{ref}(t)$ to stay at V_{ref_E} for a short period of time to ensure a better voltage regulation coordinations with multiple distributed DERs at different locations inside the microgrid. Furthermore, it is necessary to dedicate BESS mainly for frequency regulation when the microgrid experiences inadmissible frequency fluctuations, which is addressed by the new condition 3. To illustrate the effects of those new sets of conditions on the behaviors of BESS converter and microgrid operation, two case studies are presented in Ch. 6.3.

5.5 Simulation Studies

This section summarizes case studies for Fig. 5.1 microgrid performance. Three cases demonstrate the microgrid transients with one or multiple IMs, showing the effectiveness and advantages of the BESS adaptive voltage regulation on motor post-islanding recovery. Two additional sensitivity studies help to further estimate the normalized minimum required BESS inverter size for successful microgrid motors fault ride-through under both $symmetrical$ and $asymmetrical$ faults.

Prior to the fault, the system works in steady state with diesel synchronous generator, generating 2.5 MW (80% of its nameplate capacity) to the grid. The BESS is in the standby mode, connected to the PCC and synchronized to the host utility by its PLL. At $t = 0.55\ s$, a permanent fault strikes the middle of the feeder between circuit breaker $\#3$ and $\#4$. At $t = 0.6\ s$, 3 cycles after the fault, abnormal conditions are detected and the BESS starts to activate its converter for voltage and frequency regulation. The fault is cleared by opening breakers $\#3$ and $\#4$. As a result, part of the distribution system functions as a microgrid downstream of the PCC. The studies are based on $V_{ref}(t)$ algorithm in Fig. 5.6 with the following voltage regulator parameters: $V_{ref_N} = 1.00\ pu$, $V_{ref_E} = 1.35\ pu$, $V_{db} = 0.05\ pu$, $V_{th_L} = 0.50\ pu$, $V_{th_H} = V_{ref_E} - V_{db} = 1.30\ pu$, $K_R = 7\ V/s$, $t_{rs_1} = 0.100\ s$ (6 cycles), $t_{rs_2} = 0.067\ s$ (4 cycles), $t_{rs_3} = 1.000\ s$ and

$I_{sat} = 0.90\ I_{max}$.

5.5.1 Transient Study#A: Impacts of BESS size on motor speed recovery

In this first case, only the 2250 HP IM$_1$ is in operation with load torque equals to 90% of its rated torque, $T_{M_1} = 0.9\ T_{r_1}$. The microgrid is islanded 3 cycles after the fault. Figs. 5.8 to 5.14 illustrate the responses of the BESS and the system performance, both without and with different sizes of BESS.

Figure 5.8 presents the IM$_1$ rotor speed, ω_{IM_1}, without and with 3 different sizes of BESS inverter in the range of ($0.5 < S_B < 2.5\ MVA$) in steps of $1\ MVA$. One can find the $2.5\ MVA$ BESS inverter interface impedance to PCC and the associated $current - control$ scheme parameters in the Appendix A.6. These values are scaled according to [48] in order to account for the inverter power rating changes. The speed ω_{IM_1} is unable to recover if $S_B < 2.5\ MVA$. It is also learned that ω_{IM_1} can reach a higher value after islanding with a larger inverter's support, indicating that the motor is more likely to ride through the disturbance with a large BESS.

In order to understand the key implementation stages of the adaptive voltage regulation, it is instructive to observe the PCC voltage profiles, summarized in Fig. 5.9 for scenarios without and with a 2.5 MVA BESS. The fault causes a severe voltage sag. Without the BESS, the voltage oscillates around $0.5\ pu$ even after the islanding due to the excessive reactive power consumed by the motor. This is resolved by tripping the motor slightly after $t = 1.3\ s$. Even by doing so, the PCC voltage magnitude still does not return to its nominal value in a timely manner. Instead, it experiences a large swing due to the slow action of the diesel generator excitation system [125]. On the other hand, the $\hat{V}_{PCC}$ quickly recovers with the help of the BESS after the islanding. One can see that the

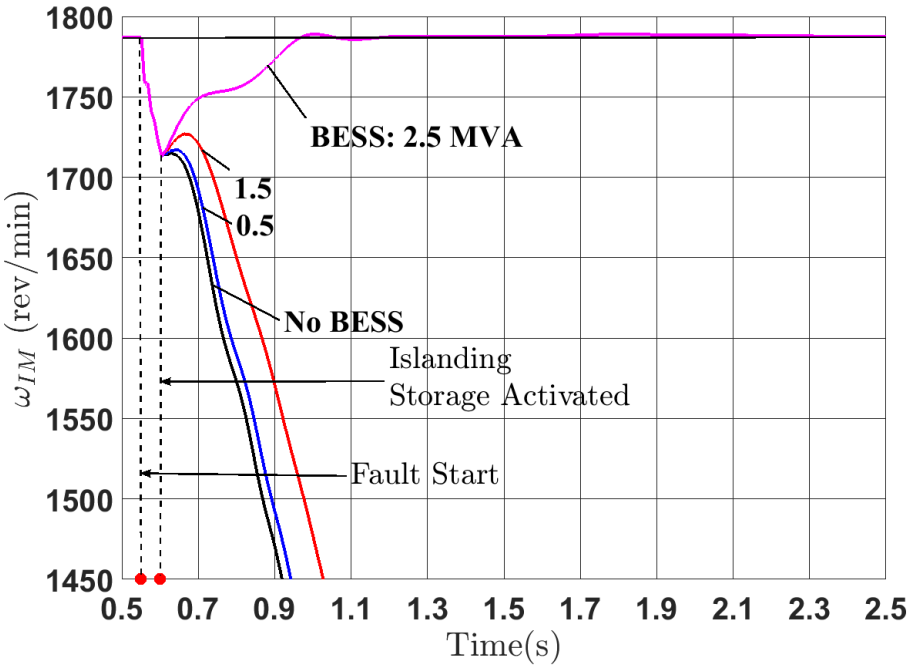

Figure 5.8: Induction motor speed ω_{IM_1} under different BESS sizes

$V_{ref}(t)$ ramps up from V_{ref_N} to V_{ref_E} after sensing the low voltage condition at $t = 0.6\ s$, $\hat{V}_{PCC} < V_{th_L} = 0.5\ pu$. In this specific case, the 2.5 MVA BESS is not large enough to regulate $\hat{V}_{PCC} > (V_{ref_N} - V_{db}) = 0.95\ pu$ within the time duration of $t_{rs_1} = 0.1\ s$ and thus $V_{ref}(t)$ ramps down at $t = 0.7\ s$. The voltage regulator then helps the $\hat{V}_{PCC}$ profile back to V_{ref_N} as the IM$_1$ recovers its speed.

The oscillograms of IM$_1$ electromechanical torque T_{e_1} with and without a 2.5 MVA BESS are presented in Fig. 5.10. Thanks to the direct contribution of the BESS to the voltage recovery, it clearly shows the immediate boost of the torque after the fault clearing. This contributes to a successful motor fault ride-through. On the other hand, without the BESS, the prolonged voltage sag leads to an unrecoverable motor torque T_{e_1}.

The IM$_1$ electromagnetic torques T_{e_1} (%) versus speed ω_{IM_1} (%) in Fig. 5.11 gives an alternative view of BESS influences on the induction motor speed recovery. A new stable equilibrium point is achieved with the help of the BESS after the islanding. It

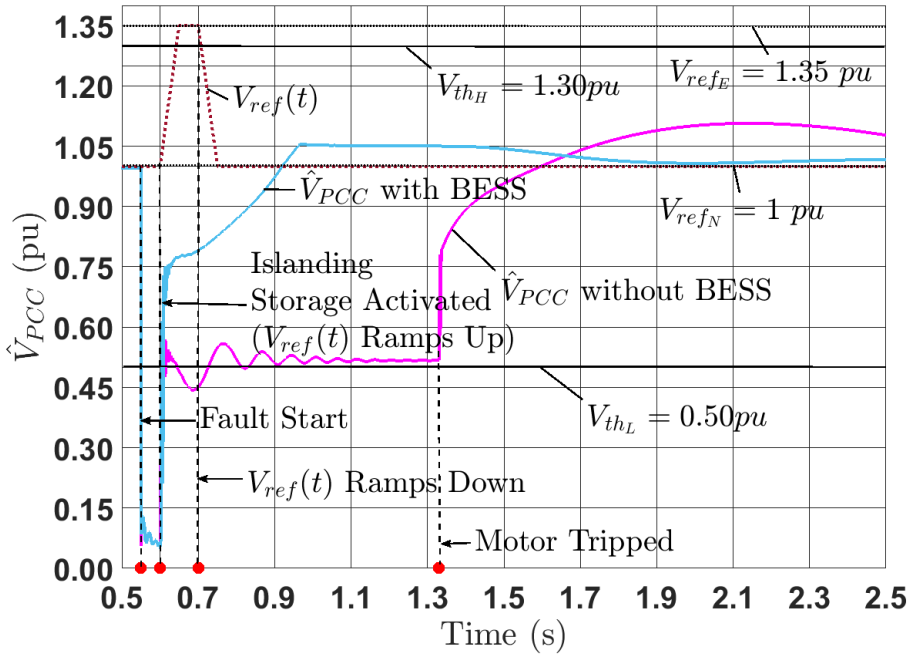

Figure 5.9: $\hat{V}_{PCC}$ with and without 2.5 MVA BESS

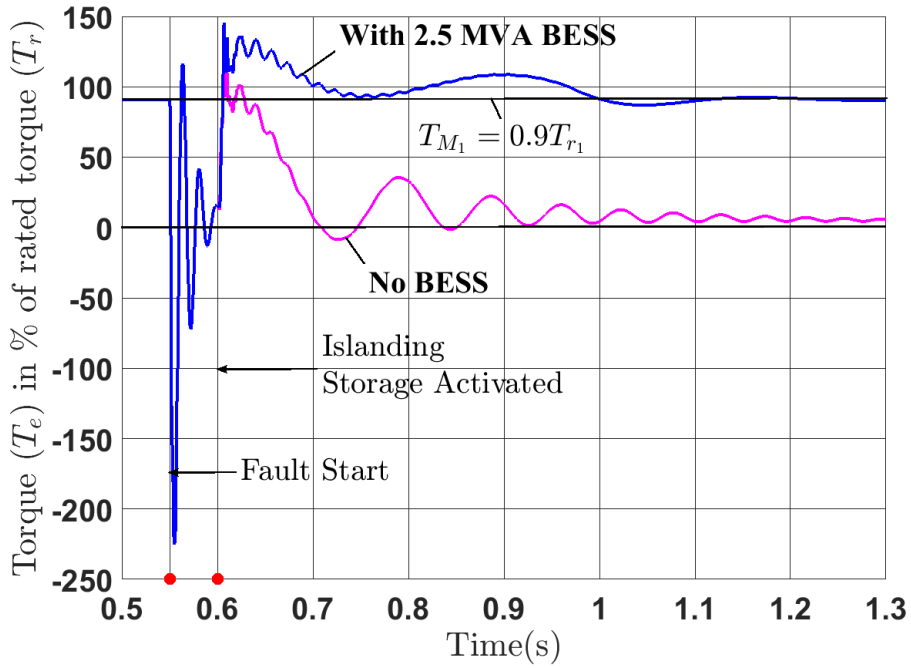

Figure 5.10: Induction motor torque (T_{e_1}) versus time with and without 2.5 MVA BESS

shows that the torque trajectory increases to the level greater than the load torque which helps the motor return to its original speed. However, without the BESS, the delivered motor torque remains low. As a consequence, its speed is decreasing toward the tripping condition.

The BESS responses during the above event are captured in Figs. 5.12 and 5.13. The converter d/q current components in time are plotted in Fig. 5.12. After sensing the fault, the i_q ramps to the negative converter current capacity limit to generate the needed maximum reactive power for the PCC voltage support. This condition is reflected in Fig. 5.13(b) reactive power response. The reactive power magnitude is increasing as the PCC voltage is recovering and eventually reaching the converter apparent power rating ($0.25\ pu$).

The BESS frequency regulator [127] is activated immediately after the $\hat{V}_{PCC}$ recovers to V_{ref_N}, Fig. 5.9. This condition results in the dynamic allocation between i_d and i_q, Fig. 5.12, meant to achieve both microgrid frequency and voltage control. Fig. 5.13(a) and (b) show the associated converter output real and reactive power in time. Their responses closely follow the reference signals.

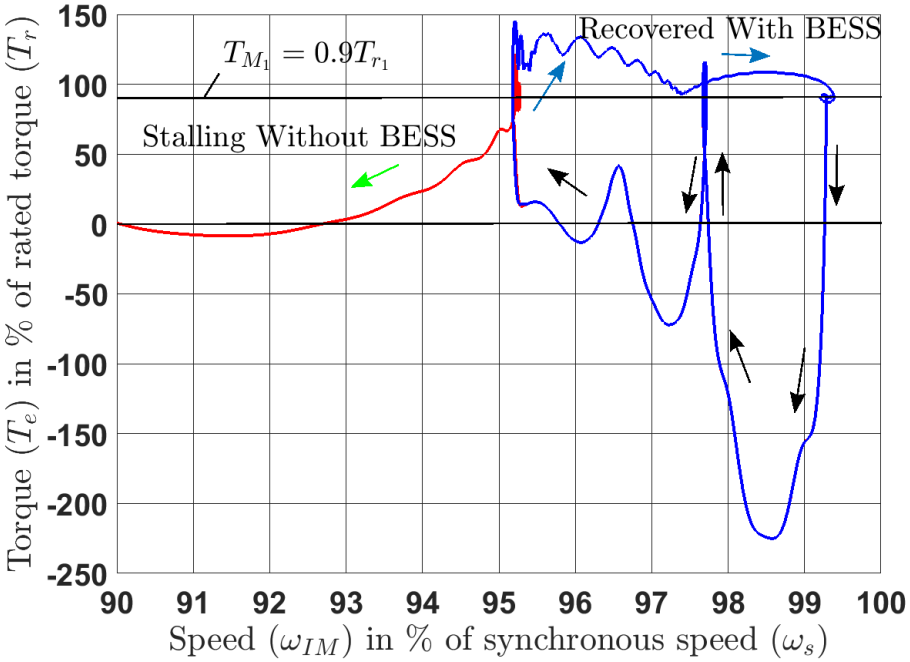

Figure 5.11: Induction motor torque (T_{e_1}) versus speed (ω_{IM_1}) with and without 2.5 MVA BESS

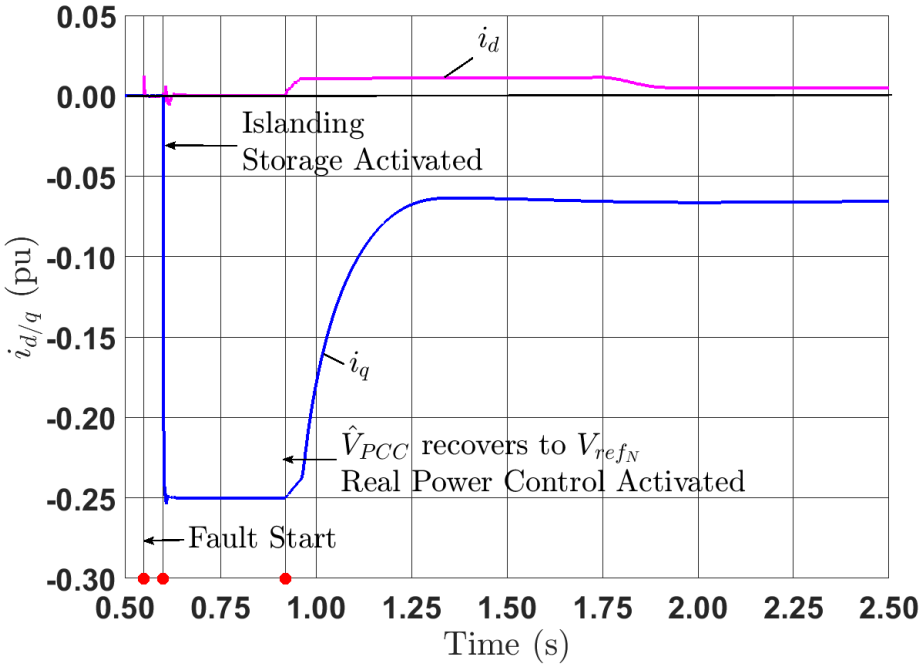

Figure 5.12: BESS converter current d/q frame components versus time

To complete the picture, the diesel generator frequency f_r oscillograms with and without the BESS are shown in Fig. 5.14. Without the BESS, the generator frequency experiences an excursion that is close to $2\ Hz$. With $2.5\ MVA$ BESS, the generator frequency stays within $0.5\ Hz$ deviation from the nominal $60\ Hz$. This clearly shows the beneficial contribution of the BESS to the microgrid frequency stability [127].

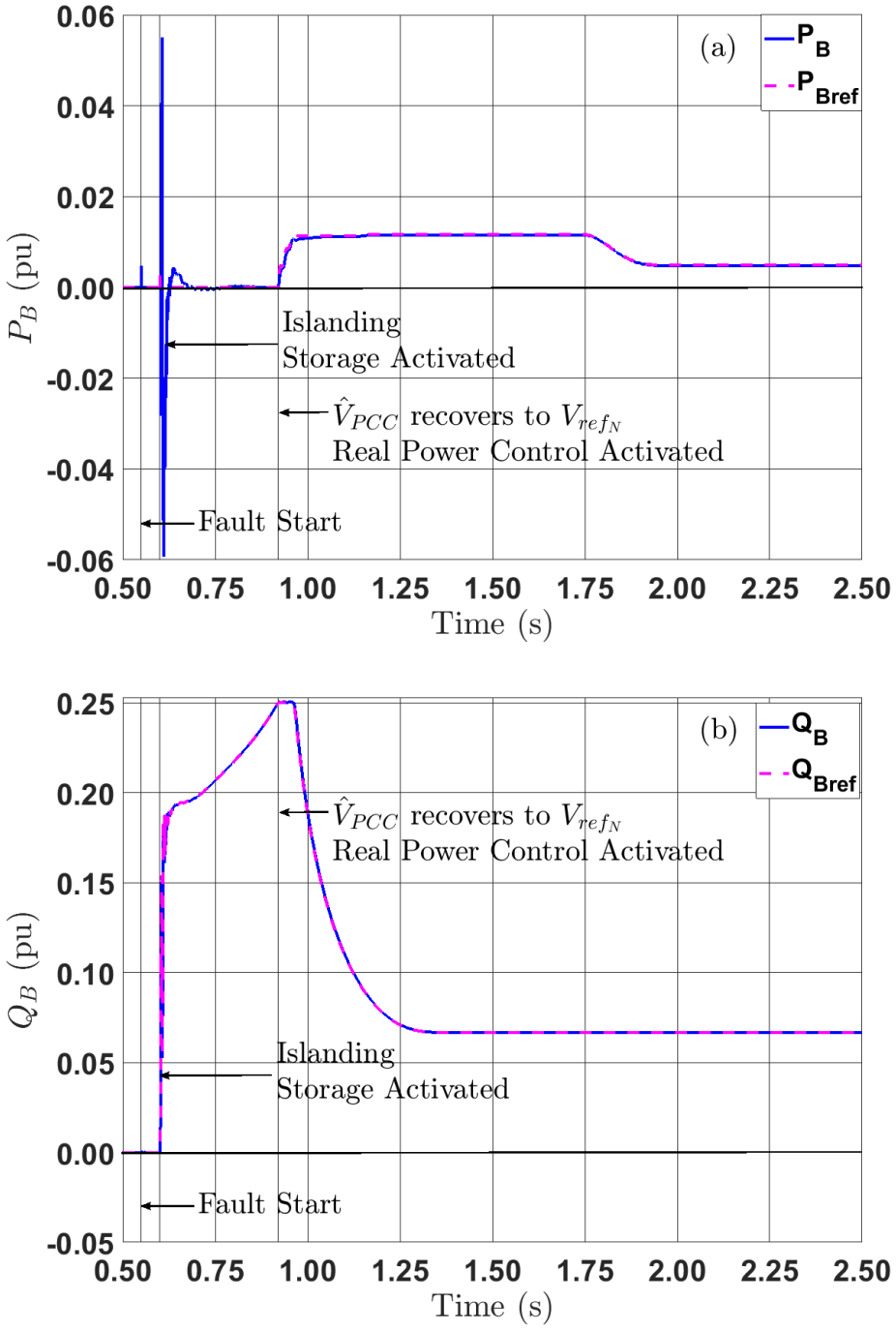

Figure 5.13: BESS power versus time: (a). Real power, (b). Reactive power.

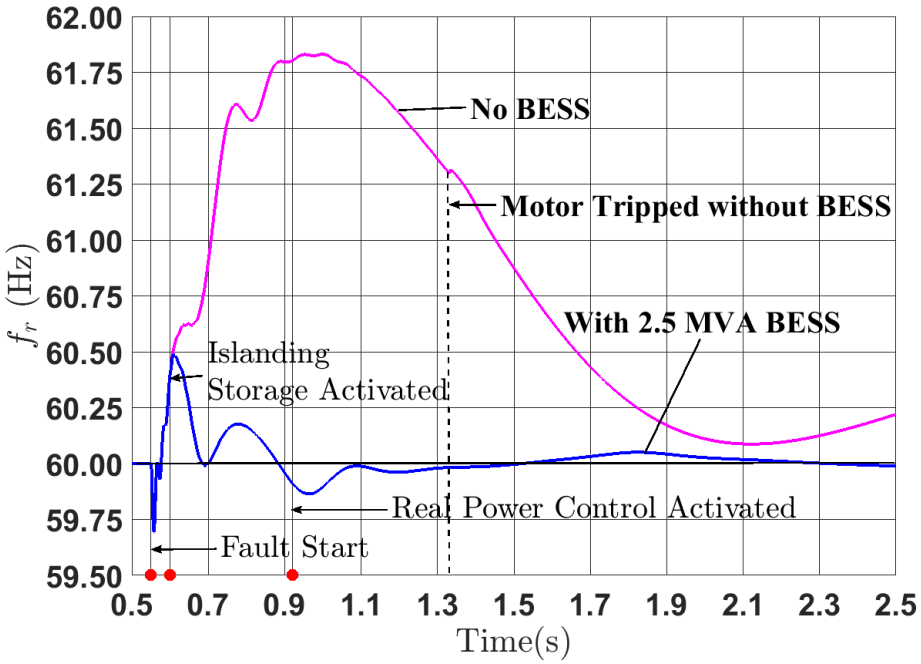

Figure 5.14: Generator frequency f_r versus time with and without 2.5 MVA BESS

5.5.2 Transient Study#B: Advantage of adaptive voltage regulation

The second Transient Analysis demonstrates the advantages of adaptive voltage regulation over the normal voltage regulation on IM recovery enhancement. The microgrid is defined by the same parameters as in Transient Analysis 1 except that the three-phase fault clearing takes 7 cycles (4 cycles longer). Consequently, it requires a large 7 MVA BESS to recover the motor, determined through the same time-domain simulation approach used in the Transient Analysis 1. Considering that the total amount of load inside the islanded microgrid is only 2.47 MW, the BESS size may seem to be too large to be economical. However, if one considers the fact that for most of the time the microgrid is operated under the grid-connected mode where the BESS can participate in multiple grid side services such as load shifting, outage avoidance or feeder deferral [19], then it is possible that a microgrid with a large BESS may be economically feasible. The BESS responses and the microgrid dynamics during the islanding event are presented in Figs.

5.15 to 5.19 under either adaptive or normal voltage regulation.

Figure 5.15 presents the IM_1 speed during transients. It shows that the IM_1 speed can recover under the adaptive voltage regulation but not with normal voltage regulation. One can interpret the concept by studying both $\hat{V}_{PCC}$ profiles in Fig. 5.16 and motor torque responses in Fig. 5.18. The prolonged fault clearing leads to a rapid decline of the motor speed. Thus, even through with the BESS's help, the $\hat{V}_{PCC}$ can recover to nominal value immediately after the islanding under normal voltage regulation, Fig. 5.16, the nonlinear transient torque T_{e_1} is still not high enough to overcome the motor load torque T_{M_1}, Fig. 5.18. As a consequence, the motor speed will decrease to the point of tripping. On the contrary, adaptive voltage regulation increases the $V_{ref}(t)$ during the post-islanding recovery phase. It helps the $\hat{V}_{PCC}$ ramp up to a higher value as shown in Fig. 5.16. This contributes to $T_{e_1} > T_{M_1}$ in Fig. 5.18; hence the motor can accelerate even from a relatively low speed with a large load torque. The $V_{ref}(t)$ immediately ramps down as soon as the $\hat{V}_{PCC} > V_{th_H} = 1.30\ pu$. Moreover, the detailed oscillograms for the V_{PCC} voltage waveform during this recovery phase ($1.40 < t < 1.55\ s$) is shown in Fig. 5.17. It illustrates the adaptive voltage regulation on the control of the PCC voltage magnitude without sacrificing the waveform quality during the transient. Additional simulations indicate that the critical islanding time for this case under normal voltage regulation is **6** cycles. It is **10** cycles with the adaptive voltage regulation. With an improvement of **66 %**, this justifies the benefits of utilizing adaptive voltage regulation on enhancing IM speed recovery.

Looking at the BESS converter current d/q frame components in time, Fig. 5.19, one can see that part of the difference between the adaptive and normal voltage regulation strategies lies in the different real time allocations between the real and reactive current components within the converter current capacity. With the adaptive voltage regulation, the converter utilizes all its capacity to regulate PCC voltage toward to a higher level. The

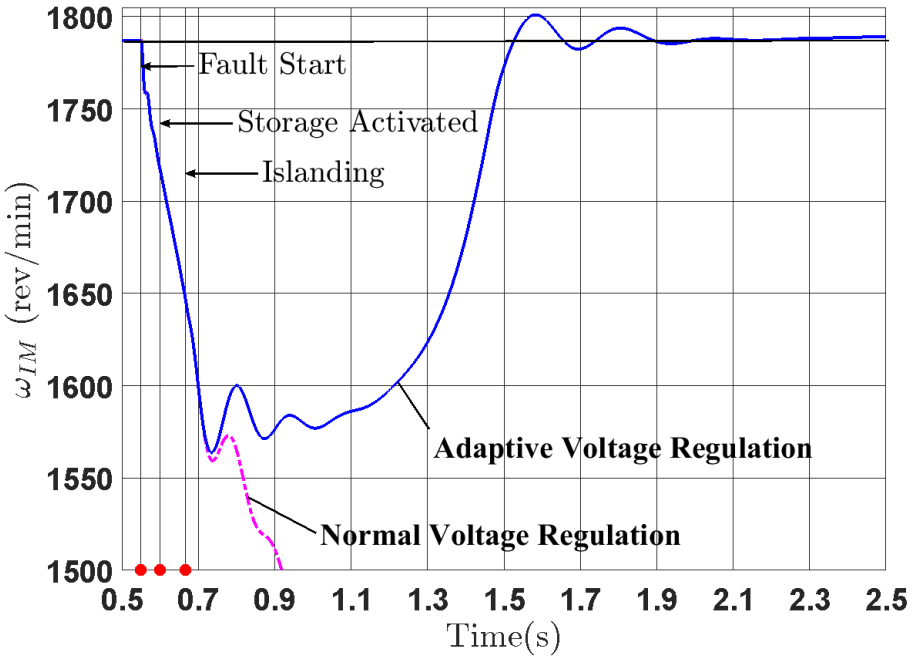

Figure 5.15: Induction motor speed ω_{IM_1} with and without adaptive voltage regulation

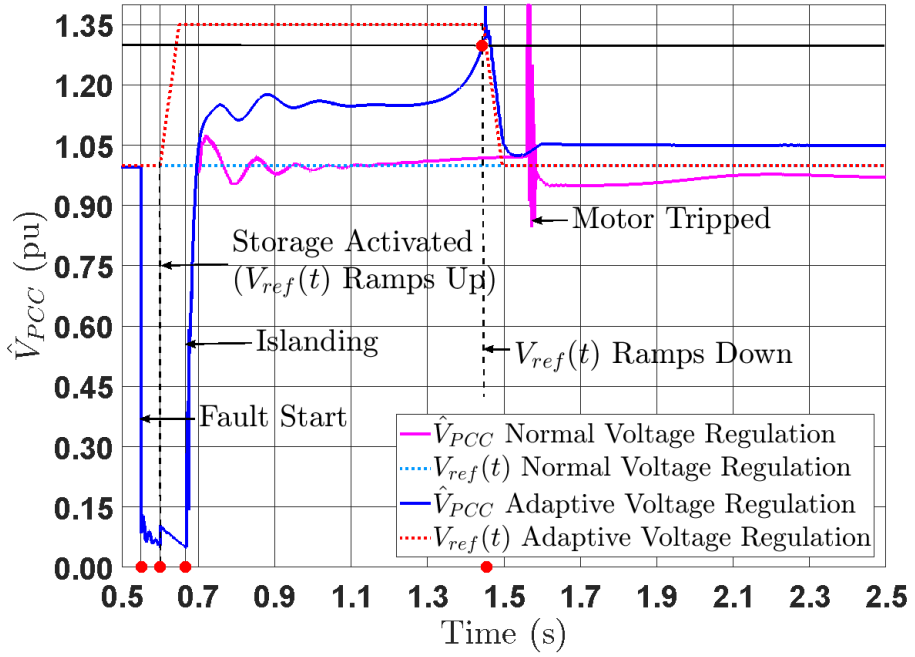

Figure 5.16: $\hat{V}_{PCC}$ with and without adaptive voltage regulation

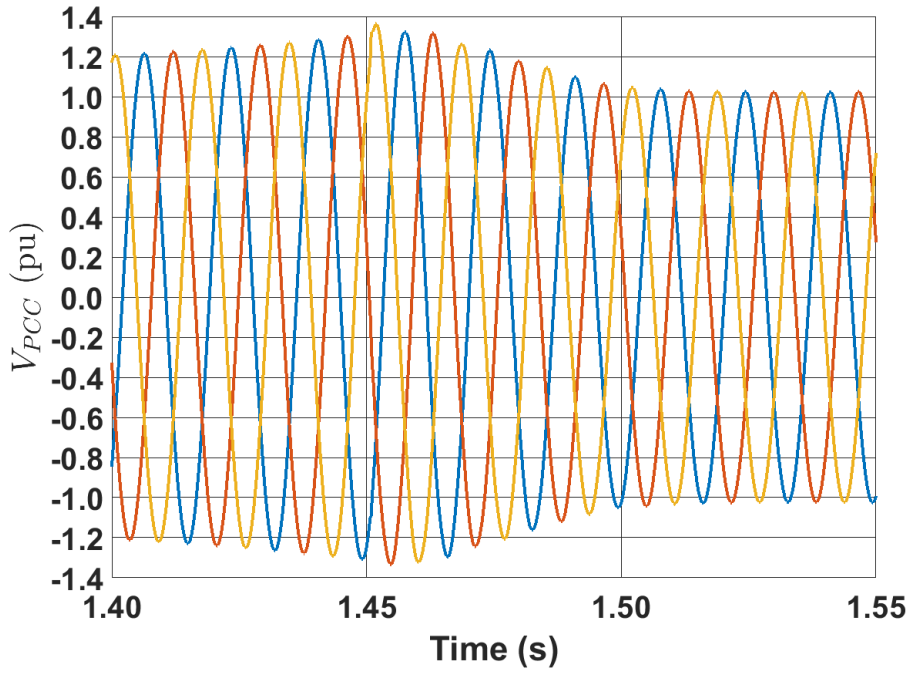

Figure 5.17: PCC voltage waveform oscillograms under adaptive voltage regulation, $1.40 < t < 1.55\ s$.

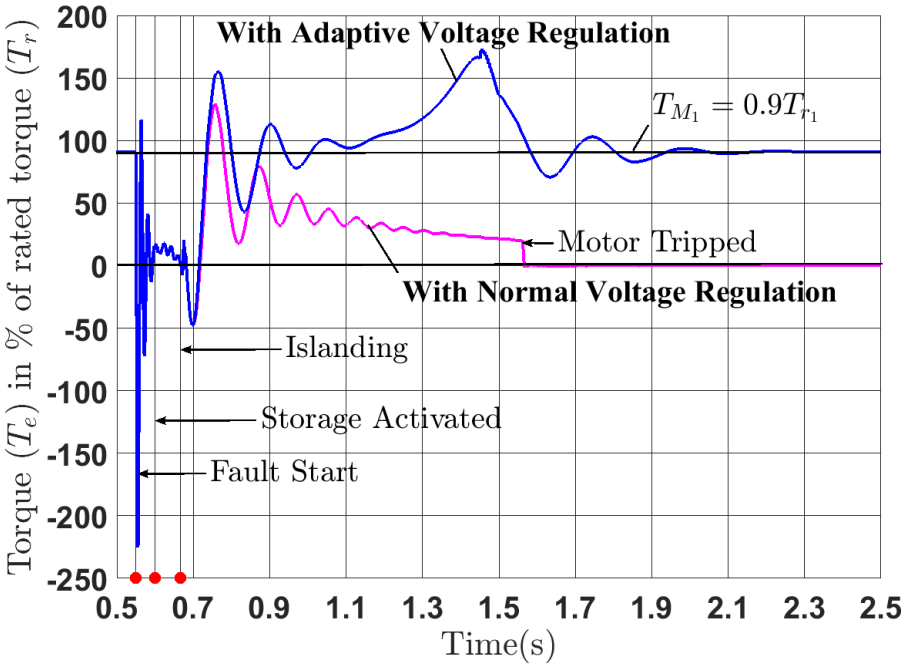

Figure 5.18: Torque of induction motor (T_{e_1}) versus time with and without adaptive voltage regulation

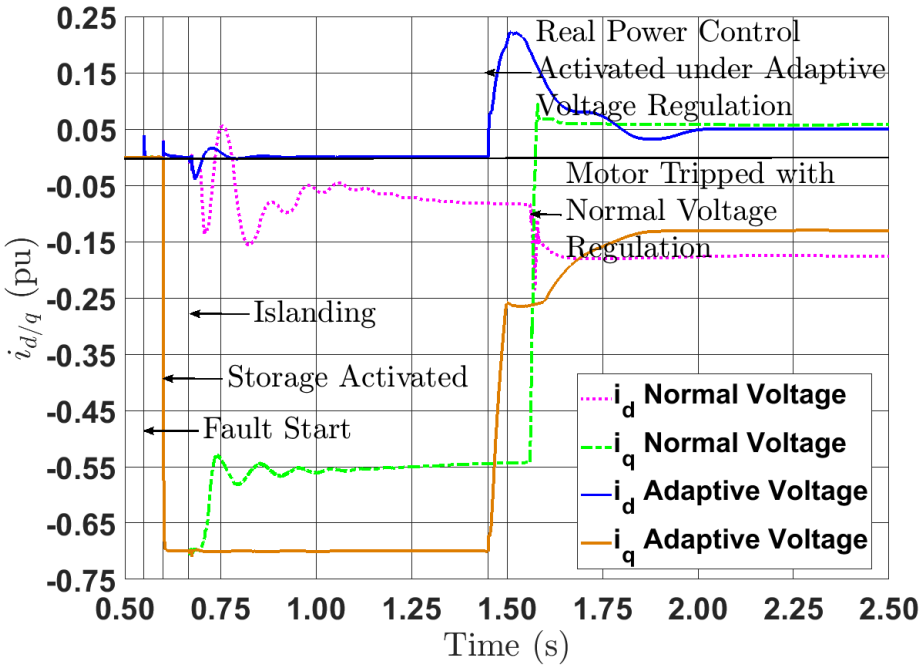

Figure 5.19: BESS converter current d/q frame components versus time, with and without adaptive voltage regulation

maximum reactive power (maximum i_q) support duration is significantly longer compared to the normal voltage regulation. This contributes to a successful motor fault ride-through. Overall, this case study helps one to understand the concept as well as the benefits of adaptive voltage regulation on enhancing the microgrid's IM speed recovery for achieving an uninterrupted high-quality power supply.

5.5.3 Sensitivity Study#A: Minimum BESS size under symmetrical fault

This case study assumes that IM_1 is carrying a constant torque load P_{IM_1} and it considers four different P_{IM_1} under the range of $30\%P_{r_1} \leq P_{IM_1} \leq 90\%P_{r_1}$ in steps of $20\%P_{r_1}$, where P_{r_1} is the IM_1 rated power. This will result in the motor load making up from 34% to 61% of the total microgrid real power demand.

As in the previous Transient Analyses $\#A$ and $\#B$, multiple simulations were conducted to find the minimum BESS inverter size for a successful motor recovery. The results under different motor loadings are then normalized with respect to their total microgrid real power demand respectively and summarized in Fig. 5.20's four sub-graphs. Each graph plots the normalized minimum BESS converter size $\overline{S}_B$ versus equivalent motor inertia constant H_{IM_E} [15], defined as:

$$H_{IM_E} = \frac{\text{stored kinetic energy in MJ at operated speed}}{\text{motor loading in MW}} \tag{5.1}$$

or

$$H_{IM_E} = \frac{\frac{1}{2}\sum_{n=1}^{N} J_{IM_n}\omega_{om_n}^2}{\sum_{n=1}^{N} P_{IM_n}} \ (s) \tag{5.2}$$

where

$$J_{IM_n} = K_{J_n} J'_{IM_n} \tag{5.3}$$

is the total polar moment of inertia for the n^{th} microgrid motor, including its rotor plus mechanical load and ω_{om_n} is the motor operated speed at the load of P_{IM_n}.

For this sensitivity study with only IM_1:

$$H_{IM_E} = \frac{\frac{1}{2} J_{IM_1}\omega_{om_1}^2}{P_{IM_1}} \ (s) \tag{5.4}$$

The effect of motor inertia is determined by simulating cases where the total inertia of IM_1's rotor and load combined is equal to K_{J_1} times the base J'_{IM_1} (Appendix A.7) as in (5.3). K_{J_1} ranges from 1-19 in steps of 3. Family of curves under fault clearing time from 3-9 cycles in steps of 2 cycles are plotted in each sub-figure, Fig. 5.20.

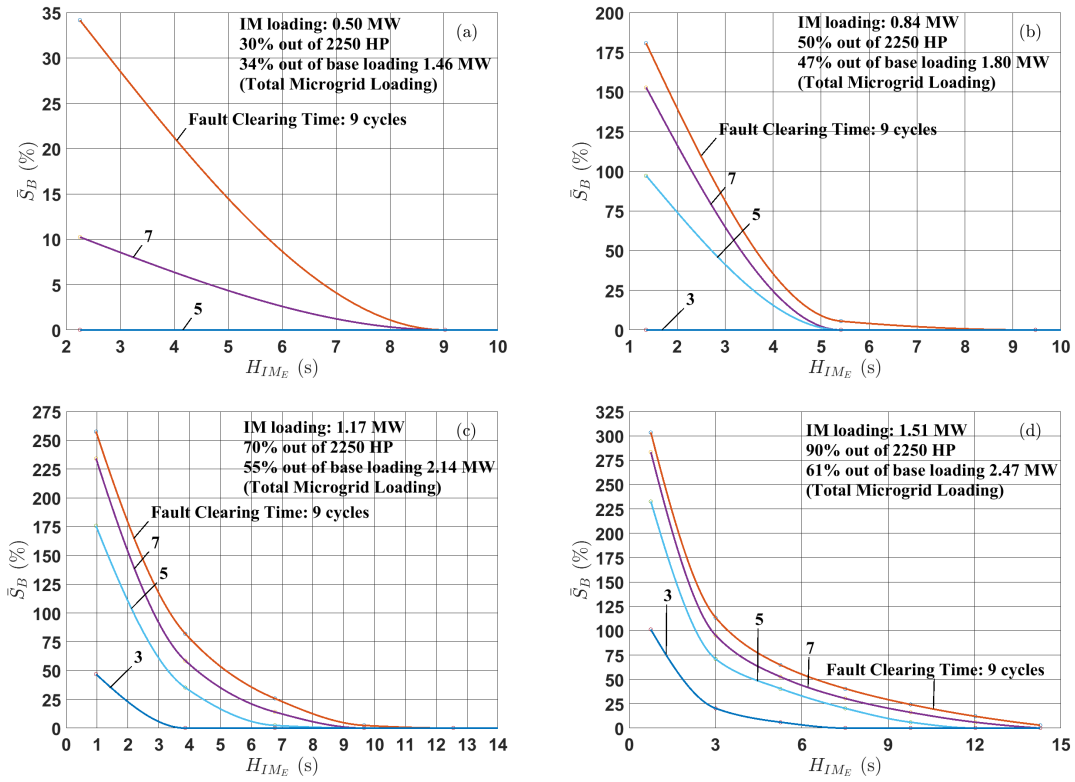

Figure 5.20: Normalized minimum BESS inverter size $\overline{S}_B$ as a function of equivalent motor inertia constant H_{IM_E} with fault clearing time as the parameter: (a). 34 % IM loading, (b). 47 % IM loading, (c). 55 % IM loading, (d). 61 % IM loading.

The combined impacts of motor inertia, loading and fault clearing time can be substantial. For example, if the IM_1 with base inertia $J_{IM_1} = J'_{IM_1}$ ($H_{IM_E} = 0.75\ s$) is 90% loaded (which accounts for approximately 60% of the total microgrid loading), the required minimum BESS inverter can be as high as 300% of the original microgrid demand under 9 cycles of fault clearing.

The results can be summarized in the following three rules:

1. A high inertia motor will require a smaller BESS.

2. As the fault clearing time increases, the motor will need a larger BESS for a successful ride-through.

3. The microgrid loading has direct impacts on the required BESS inverter size. A microgrid with larger percentage of IM loading demands a bigger size inverter to ride through the fault-triggered islanding incident.

An important advantage in generating the normalized minimum BESS converter size results, like one in Fig. 5.20, is that this kind of comprehensive presentation provides useful engineering guidelines for approximate sizing of the BESS for a given microgrid. Later on, these results are tested by sizing the BESS based on an additional transient case study with a loading of two IMs.

5.5.4 Sensitivity Study#B: Minimum BESS size under asymmetrical fault

If the fault type is asymmetrical, for example a single-phase to ground fault instead of three-phase, the minimum required BESS size versus fault clearing time is plotted in Fig. 5.21. The system is operated with the IM_1 under 90% loading and $H_{IM_E} = 0.75\ s$.

Comparing Figs. 5.20 and 5.21, one will observe the significant reduction of the size of the needed for BESS under this less severe fault, even though the fault clearing time can be much longer in the single-phase fault case than three-phase. In fact, no BESS is required for IM_1 to ride through disturbance as long as the single-phase fault is cleared within 9 cycles. Even with $H_{IM_E} = 0.75\ s$ and a prolonged fault clearing time of 30 cycles, the microgrid only needs $\overline{S}_B = 60\%$ to recover.

Similarly, though not reported in this chapter, comparing with a three-phase fault, it will require less BESS capacity to recover motors under line-to-line and double line-to-ground faults with an assumption of the same fault clearing/islanding time.

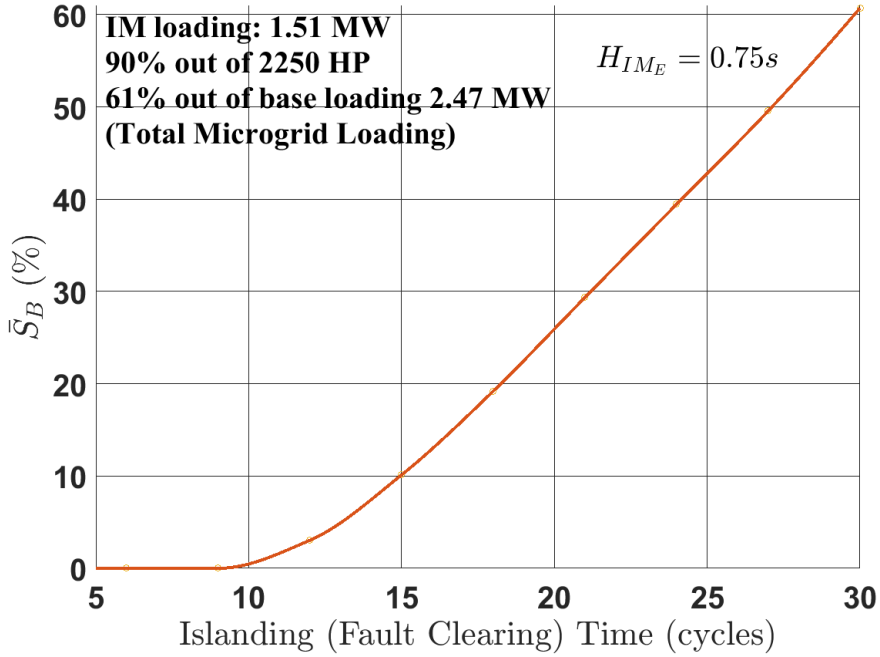

Figure 5.21: Minimum normalized BESS Size $\overline{S}_B$ as a function of fault clearing time under single-phase fault

5.5.5 Transient Study#C: Multiple IMs recovery

The final Transient Analysis is conducted under assumptions that both IM_1 and IM_2 in Fig. 5.1 are operated with 90% of their rated power under a three-phase fault and a clearing time of 3 cycles. The purpose of this case study is two-fold: first, it tests the sizing guidelines demonstrated by Sensitivity Study 1. Secondly, it verifies the effectiveness of the BESS adaptive voltage regulation strategy on enhancing multiple microgrid IMs' speed recovery during fault-induced islanding incidents.

The H_{IM_E} is calculated as $0.72\ s$ based on (5.2) with $J_{IM_1} = J'_{IM_1}$, $J_{IM_2} = J'_{IM_2}$. The IM loading accounts for 64% of the total $2.88\ MW$ microgrid demand. From Fig. 5.20(d), $\overline{S}_B = \frac{103\%}{100\%}$ under 3 cycles fault clearing with $H_{IM_E} = 0.72\ s$. The BESS

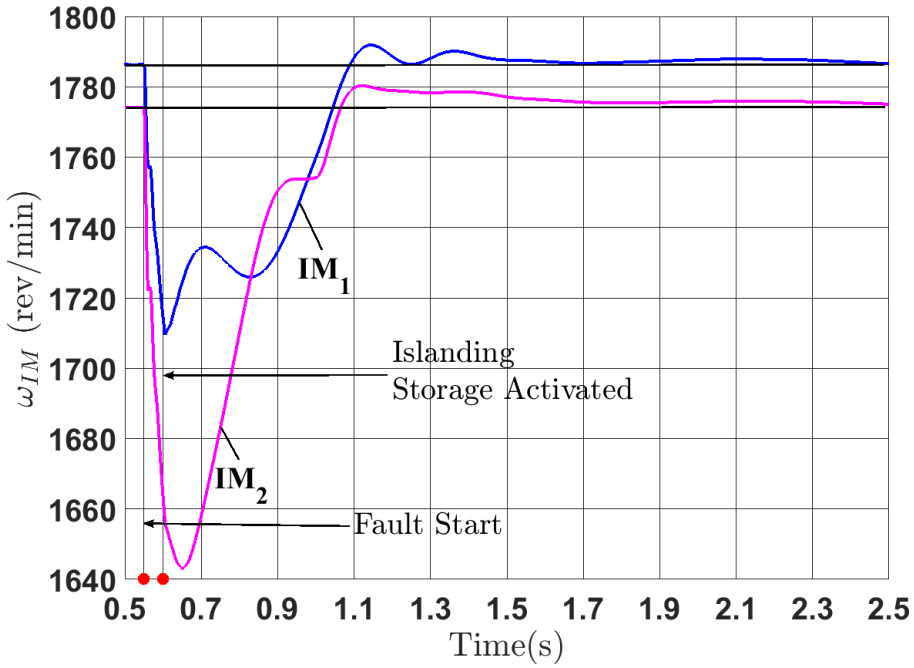

Figure 5.22: Speed of the two induction motors versus time with 3.1 MVA BESS

converter size is calculated by:

$$\begin{aligned} S_B &= \overline{S}_B S_m K_{IM} \\ &= \frac{103\%}{100\%} \cdot 2.88 \cdot \frac{64\%}{61\%} \\ &\approx 3.1\ MVA \end{aligned} \tag{5.5}$$

where

$S_m = 2.88$ is the total microgrid demand in MW.

and

$K_{IM} = \frac{64\%}{61\%}$ is the IM load linear interpolation factor.

Figs. 5.22 to 5.25 summarize the system performance and responses of the chosen 3.1 MVA BESS. With the adaptive voltage regulation, both IM_1 and IM_2's speed are

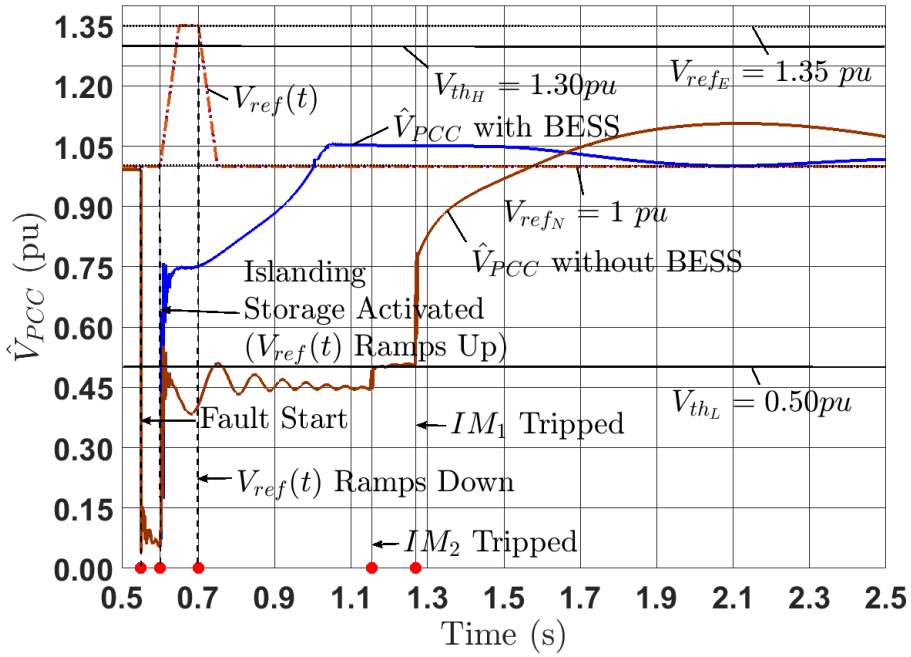

Figure 5.23: $\hat{V}_{PCC}$ with and without 3.1 MVA BESS

recovered as shown in Fig. 5.22. The PCC voltage profile is presented in Fig. 5.23. Similar to the Transient Analysis 1, the $V_{ref}(t)$ ramps up from V_{ref_N} to V_{ref_E} after sensing the low voltage condition, $\hat{V}_{PCC} < V_{th_L} = 0.5\ pu$. Due to the capacity limitation of the BESS converter, the $\hat{V}_{PCC}$ cannot immediately recover beyond $(V_{ref_N} - V_{db}) = 0.95\ pu$ and thus the $V_{ref}(t)$ ramps down after waiting for a duration of $t_{rs_1} = 0.1\ s$. Nevertheless, comparing the $\hat{V}_{PCC}$ with and without the BESS, one can see that the BESS still plays a critical role on both the voltage recovery and the IM speed recovery. And the $\hat{V}_{PCC}$ smoothly increases to V_{ref_N} as the IMs speed is recovering. The BESS initially utilizes all its inverter capacity for voltage support by injecting maximum reactive power, Fig 5.24(b). After the recovery of both voltage and IM speed, the frequency regulator controls the real power, Fig 5.24(a), which helps the diesel generator frequency return to normal as shown in Fig. 5.25.

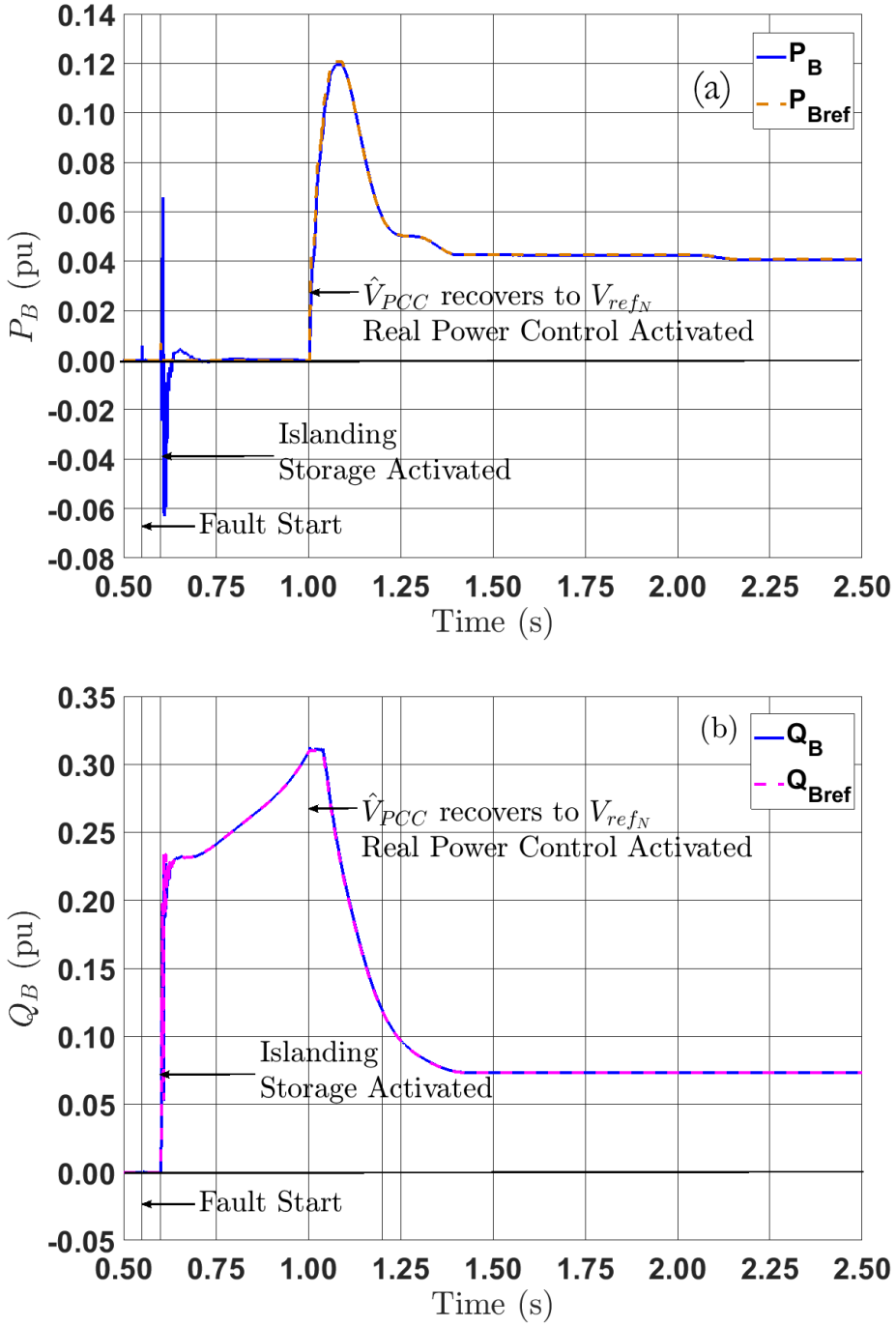

Figure 5.24: BESS power versus time under two induction motors loading: (a). Real power, (b). Reactive power.

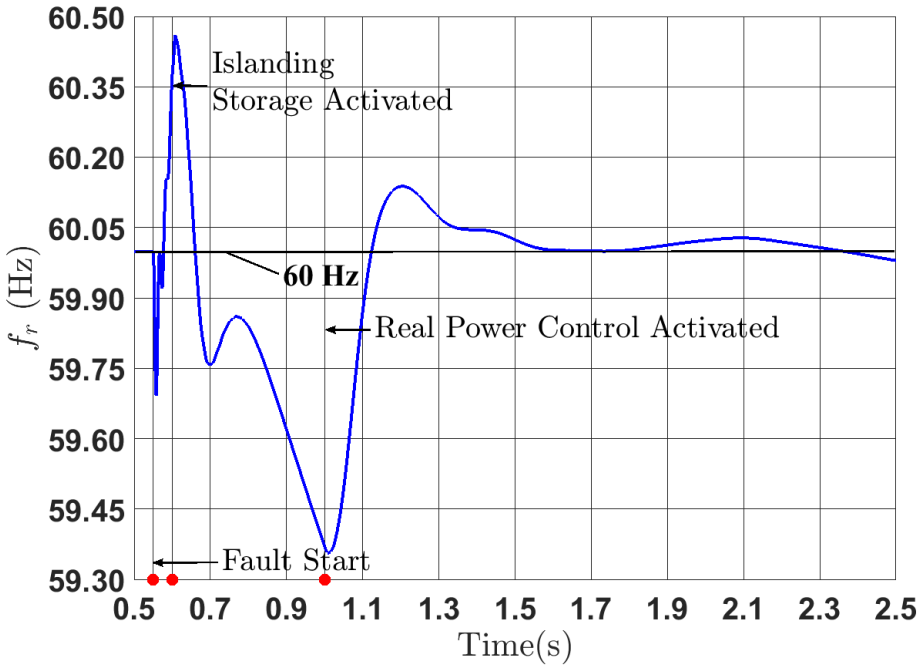

Figure 5.25: Generator frequency f_r versus time with two induction motors loading and a 3.1 MVA BESS

5.6 Chapter5 Summary

Following the previous chapter 4's work [127], this report highlights the additional benefits of adaptively controlling the BESS converter to enhance microgrid's induction motor speed recovery during fault-triggered islanding incidents by means of adaptive voltage regulation. It proposes a simple yet effective way of achieving both faster voltage recovery and longer maximum permissible fault clearing/islanding time for a microgrid with one or more IMs. The study also facilitates the microgrid design process by presenting the normalized minimum BESS inverter sizing under a wide range of microgrid motor inertia, loading and fault clearing times.

This work is mainly focused on technical considerations of the adaptive voltage regulation strategy. To determine the economic benefit, it is necessary to combine the other possible grid-support services that can be provided by the BESS [19].

Chapter 6

Adaptive Control Evaluations on CIGRE Benchmark System

This chapter presents two microgrid case studies under CIGRE MV distribution network benchmark system [14]. The pu quantities are with the base values of 12.47 kV, 10 MVA and 60 Hz for all cases. The objective is to evaluate the proposed adaptive energy storage system frequency and voltage regulation control methodologies introduced in chapters 4 and 5 with a realistic network topology.

The first study covers four cases with multiple BESSs under normal voltage regulation and adaptive frequency regulation strategies. It shows the effectiveness of BESSs and advantages of adaptive secondary control on the stability enhancement of a meshed microgrid with fault-induced feeder switching. This microgrid has unbalanced loads, multiple IMs, renewable generators with converter interfaces and distributed synchronous generators with different prime resources (diesel fuel or hydropower). Both $symmetrical$ and $asymmetrical$ faults are considered. It demonstrates the robust performance of the proposed converter controller under multiple contingencies in addition to the random power output from renewable energy sources. The second case study further illustrates the ben-

efits of adaptive voltage regulation as well as the impacts of its voltage regulation delays on the microgrid dynamics.

6.1 Microgrid System for Chapter 6

This section describes two modified CIGRE MV distribution network benchmark systems as the final microgrid systems under investigation. It is assumed that a fault happened at the high voltage (HV) subtransmission line leads to the entire MV distribution network as a fault-induced islanded microgrid. The first network contains three alternators and BESSs. The second network uses the same network topology however contains only alternators. Both microgrid systems have the similar amount of local generating capacities **(in a range between 30 to 40 MVA, including synchronous generators, BESSs and RESs)**, enough to meet the total local demands **(total of about 20 MVA)**. Appendix A.2 summarizes the detailed network and loading data.

Fig. 6.1 shows the topology of the studied microgrid network. It shows two transformers that feed two $12.47\ kV$ feeders via a $115\ kV$ subtransmission system ($X/R = 10$; 5000-MVA short-circuit capacity). It is assumed that both feeders are fed by the same substation with all five switches (S_1, S_2, S_3, S_4 and S_5) closed. Effectively, two feeders will create a meshed microgrid network if it is being islanded from the substation bus $\#0$. It should be emphasized that there are more feeders served by the two transformers that are not modeled in details in this topology [14]. This explains why there are much larger sizes of DERs and load values at the buses $\#1$ and $\#12$ at the beginning of the two feeders than those given for the other nodes.

The loadings of the system are unbalanced and distributed under a mixture of both linear RLC impedance and IM loads. Four $2.3\ kV$ IMs of various sizes (two 500 HP, two 2250 HP) are connected to their $12.47\ kV$ hosted feeders at different locations through

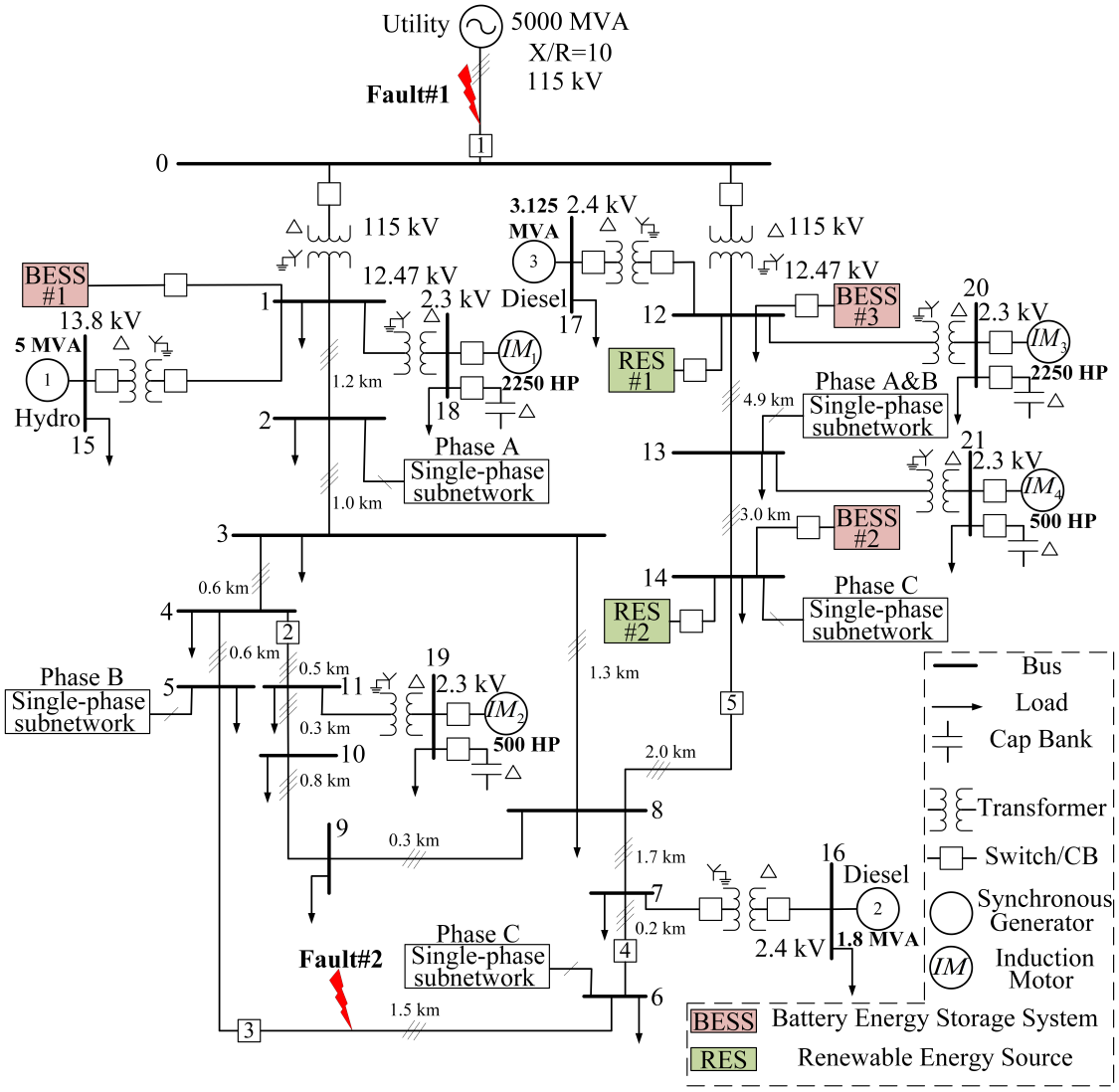

Figure 6.1: GIGRE Test Network

associated transformers. Each IM operates at 90% of its rated power. The original RLC impedance loading data [14] is modified at nodes with IMs by subtracting associated IM loading demand in order to maintain the similar amount of total local load demands.

Both synchronous generators and power inverter based DERs are added at the various nodes as shown in the schematic. One $5\ MVA$ hydroelectric generator ($R_{s_1} = 5\%$ droop) coupling with hydroelectric turbine is installed at the beginning of the feeder $\#1$, bus $\#1$. There are also two diesel generators; a smaller generator with $1.8\ MVA$ capacity ($R_{s_2} = 3\%$ droop) is at bus $\#7$ and a larger one with size of $3.125\ MVA$ ($R_{s_3} = 1\%$ droop) is at bus $\#12$. Three BESSs are installed separately at bus $\#1$, $\#12$ and $\#14$. Two renewable generators, with a random power output via their power converters under the capacity of $3.5\ MVA$ and $0.5\ MVA$, are located at bus $\#12$ and $\#14$ respectively.

The second network benchmark has the same topology as in the previous Fig. 6.1, however all three BESSs are being replaced by the diesel generators with an almost alike total output power capacity. Consequently, it is being used in the comparative case study (study #1, case #B) to show the effects of BESSs on the microgrid dynamics.

6.2 Study#1: Normal Voltage Regulation

Four cases are presented in this study. The BESSs are operated under normal voltage regulation (i.e., $V_{ref} = 1.0\ pu$) with power priority switch control, described in Ch. 5.4.2, Fig. 5.7, implemented. Case #A demonstrates the additional stability margin gained by the adaptive secondary control. Case #B compares two microgrids dynamics with and without BESSs. Case #C illustrates a Single Line-to-Ground fault in order to show the performance of microgrid and BESSs under $asymmetrical$ fault. Finally, case #D further tests the effectiveness of the proposed adaptive control strategies by applying a second fault inside an islanded microgrid along with random power supplied by the renewable

generators.

6.2.1 Case#A: Impact of BESSs secondary control approaches

This case illustrates the effects of BESS converter secondary frequency control approaches on the microgrid stability. It uses the topology shown in Fig. 6.1 as the studied microgrid system. Three BESSs (each $6\ MVA$) are all equipped with adaptive nonlinear droop control with $R_c = 3\%$. A secondary controller with $K_I = 3000$ is assumed in the first scenario for a fixed gain control approach. For the second approach with adaptive secondary control gain, it sets the $K_B = 3 \times 10^5$ which corresponds to $K_I(|\Delta f|) = 3000$ at $|\Delta f| = 1\%$ (0.6 Hz). In order to fully appreciate the advantages of adaptive secondary control, it further assumes that $K_{I_{max}} = \infty$. The only constrain for $K_I(|\Delta f|)$ during the transients in this case is a hard limitation ($15\ Hz$) for $|\Delta f|$ via converter PLL controller settings, Appendix A.6. The BESS converter frequency regulator has a frequency dead-band of $f_{db} = 6 \times 10^{-4}\ pu$ (36 mHz).

Prior to the fault, the system works in steady state with all the loads in service. All three BESSs are in the standby mode, connected to their PCCs and synchronized to the utility grid through associated PLL. The hydroelectric generator (DG#1) generates 3 MW (60% of its nameplate capacity) to the grid. Similarly, two diesel generators (DG#2: $1.8\ MVA$ and #3: $3.125\ MVA$) are delivering 1.26 MW (70% capacity) and 2.5 MW (80% capacity) respectively. The output of the renewable generators is assumed to be zero during the 2 seconds' simulation.

At $t = 0.067\ s$ (4 cycles after the simulation starts), a permanent three-phase fault strikes on the upper level subtransmission line close to the substation (bus $\#0$). This fault is cleared in 4 cycles. As the result, a meshed microrgrid is formed at $t = 0.133\ s$. Three BESSs detect the fault disturbance at different time and start to participate the frequency and voltage regulations at $t = 0.100;\ 0.117;\ 0.133\ s$ respectively, corresponding to the

fault detection time of 2, 3 and 4 cycles. Figures. 6.2 to 6.5 compare three BESSs responses and the microgrid dynamics during this fault-induced islanding event under a secondary controller with either fixed or adaptive gain.

Figure. 6.2 presents three BESSs' estimated PLL frequencies in Hz. It is evident from the left column that the fault disturbance leads to a significant fluctuation for all three PLL's frequency estimations. They further evolve into unstable oscillations around base frequency (60Hz) under the secondary controller with a fixed gain. On the contrary, the right column shows oscillograms that, with an adaptive secondary controller, all three frequency estimations have acceptable transients and quickly return to nominal frequency by the help of adaptive frequency regulation.

Figure. 6.3 summarizes three BESSs' real power responses. The BESSs controllers with a fixed secondary control gain leads to inadmissible power fluctuations. With an adaptive secondary controller, all three BESSs' power responses are stable. Moreover, it shows that each BESS quickly shares power under discharge mode and this action contributes to a fast microgrid frequency regulation. All three BESSs' power responses reach to a new equilibrium in less than one second after the start of the regulation.

Figure. 6.4 shows three BESSs' terminal (PCC) voltage magnitudes, $\hat{V}_{PCC}$ in time. The fault causes severe sags of voltage at all nodes inside the microgrid. The unstable controllers result in poor voltage supply quality as shown on the left. The right column indicates a rapid voltage recovery with stable controllers under the adaptive secondary control strategy.

Finally, three alternators' rotor speeds are summarized in Fig. 6.5. The unstable secondary frequency control causes unavoidable frequency deviations for all three generators as shown on the left. With the adaptive secondary controllers, the BESSs quickly regulate the microgrid frequency and all three generators' rotor speeds are back to $60\ Hz$ in less than a second (right column).

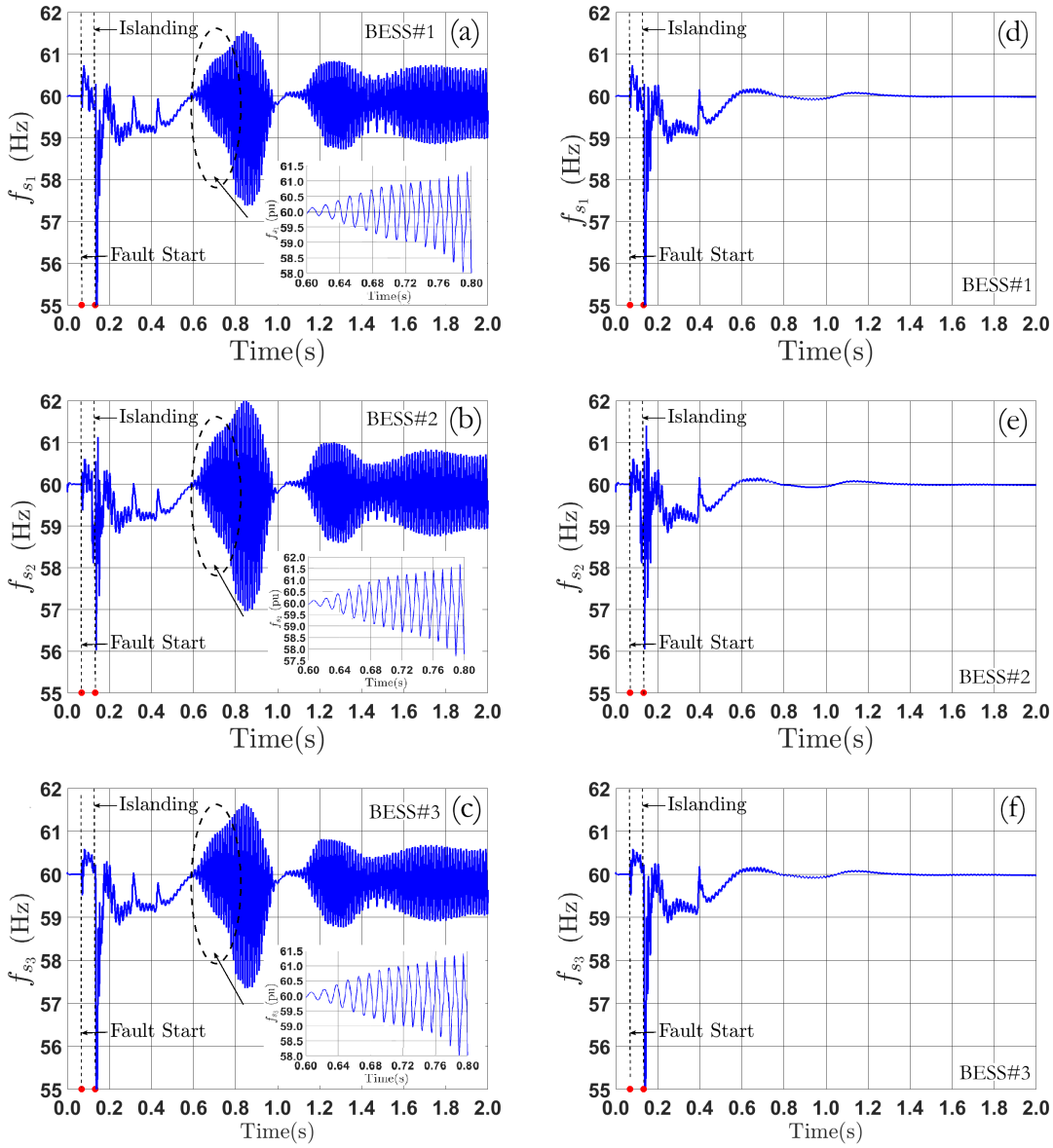

Figure 6.2: Estimated PLL Frequency f_s; (left column): unstable under secondary controller with $K_I = 3000$, (right column): stable under secondary controller with adaptive gain using $K_B = 3 \times 10^5$: (a) f_{s_1}, unstable; (b) f_{s_2}, unstable; (c) f_{s_3}, unstable; (d) f_{s_1}, stable; (e) f_{s_2}, stable; (f) f_{s_3}, stable

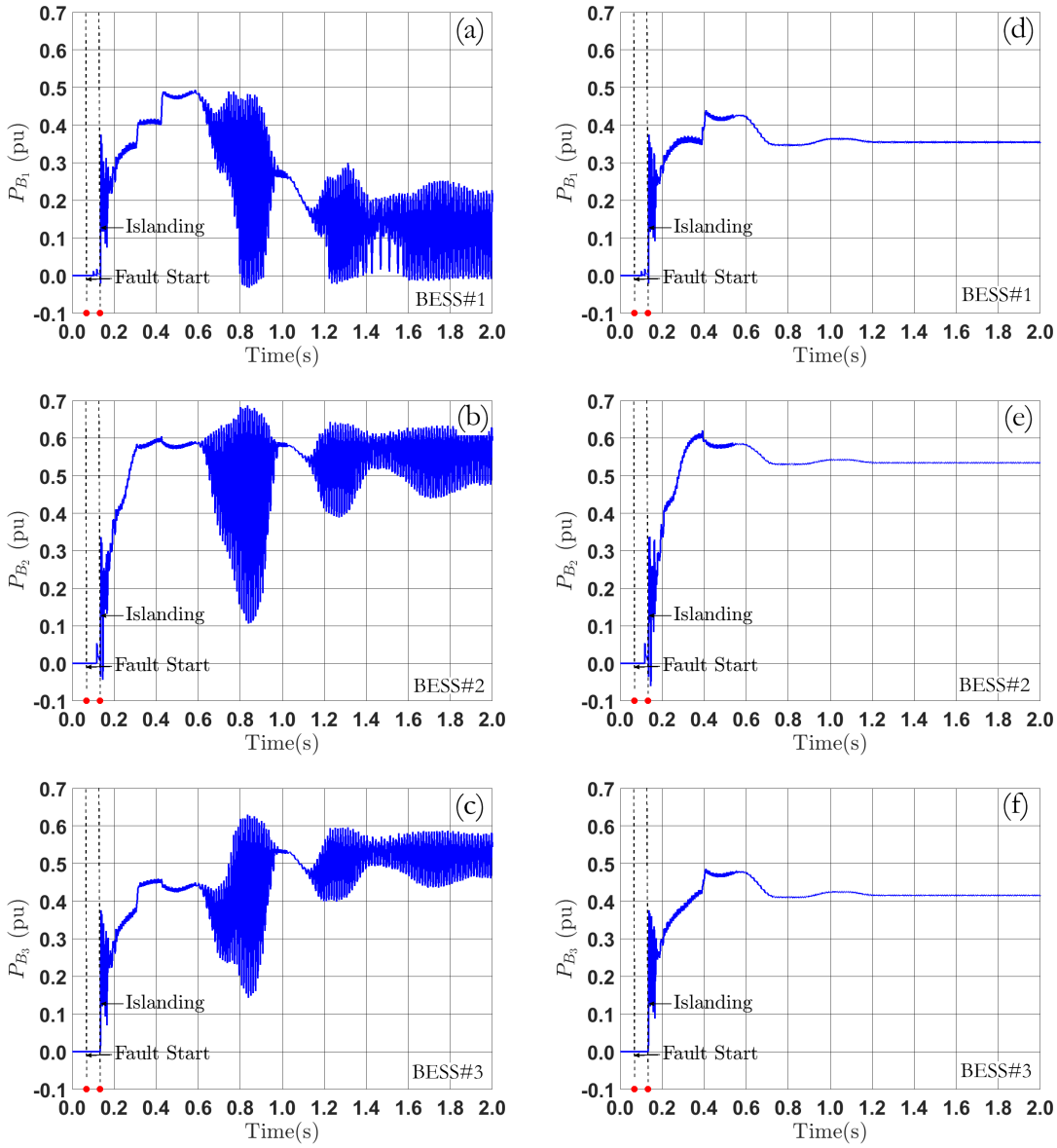

Figure 6.3: The BESSs power vs. time; (left column): unstable under secondary controller with $K_I = 3000$, (right column): stable under secondary controller with adaptive gain using $K_B = 3 \times 10^5$: (a) P_{B_1}, unstable; (b) P_{B_2}, unstable; (c) P_{B_3}, unstable; (d)P_{B_1}, stable; (e) P_{B_2}, stable; (f) P_{B_3}, stable

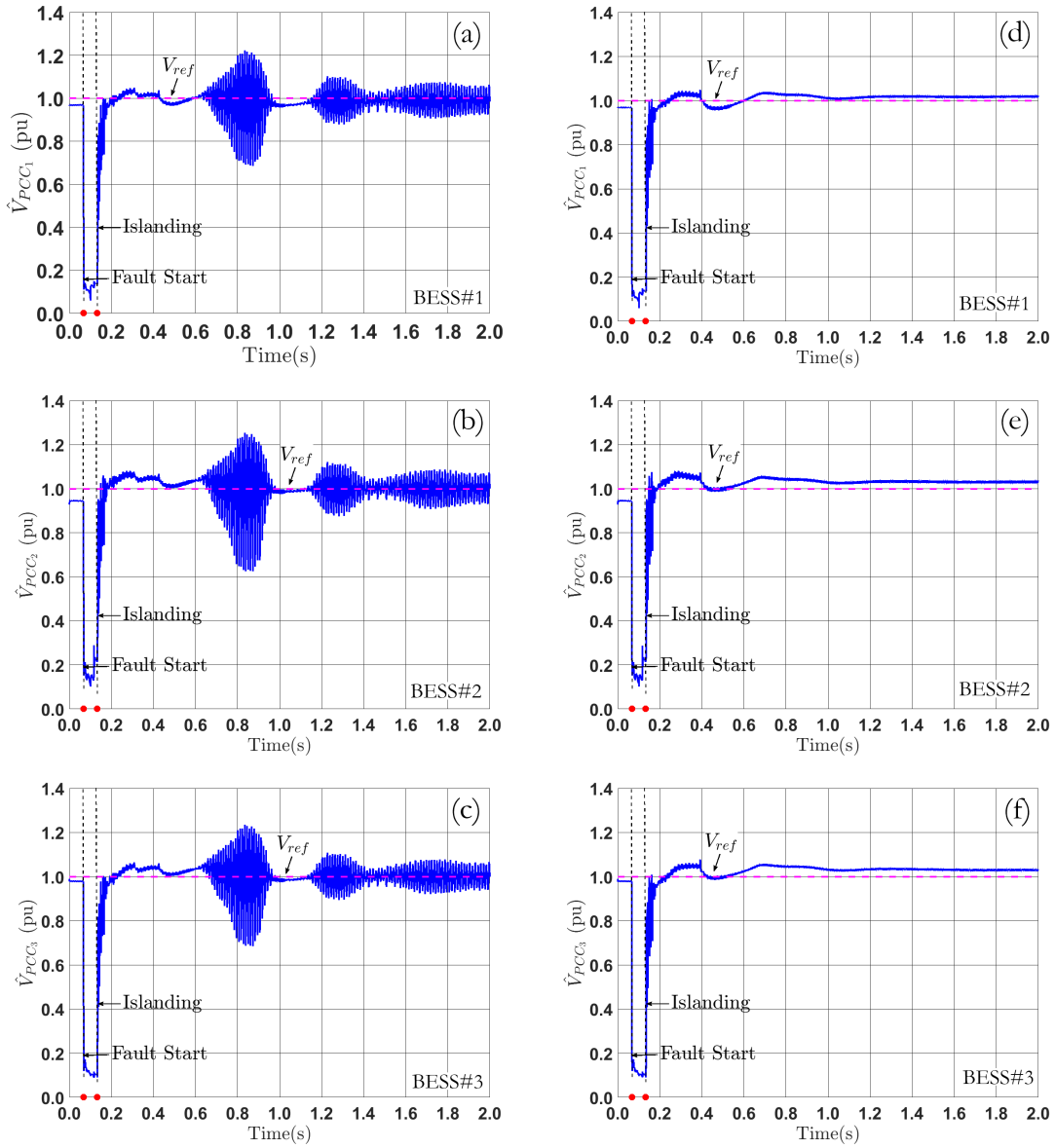

Figure 6.4: The PCCs voltage magnitude $\hat{V}_{PCC}$ vs. time; (left column): unstable under secondary controller with $K_I = 3000$, (right column): stable under secondary controller with adaptive gain using $K_B = 3 \times 10^5$: (a) $\hat{V}_{PCC_1}$, unstable; (b) $\hat{V}_{PCC_2}$, unstable; (c) $\hat{V}_{PCC_3}$, unstable; (d) $\hat{V}_{PCC_1}$, stable; (e) $\hat{V}_{PCC_2}$, stable; (f) $\hat{V}_{PCC_3}$, stable

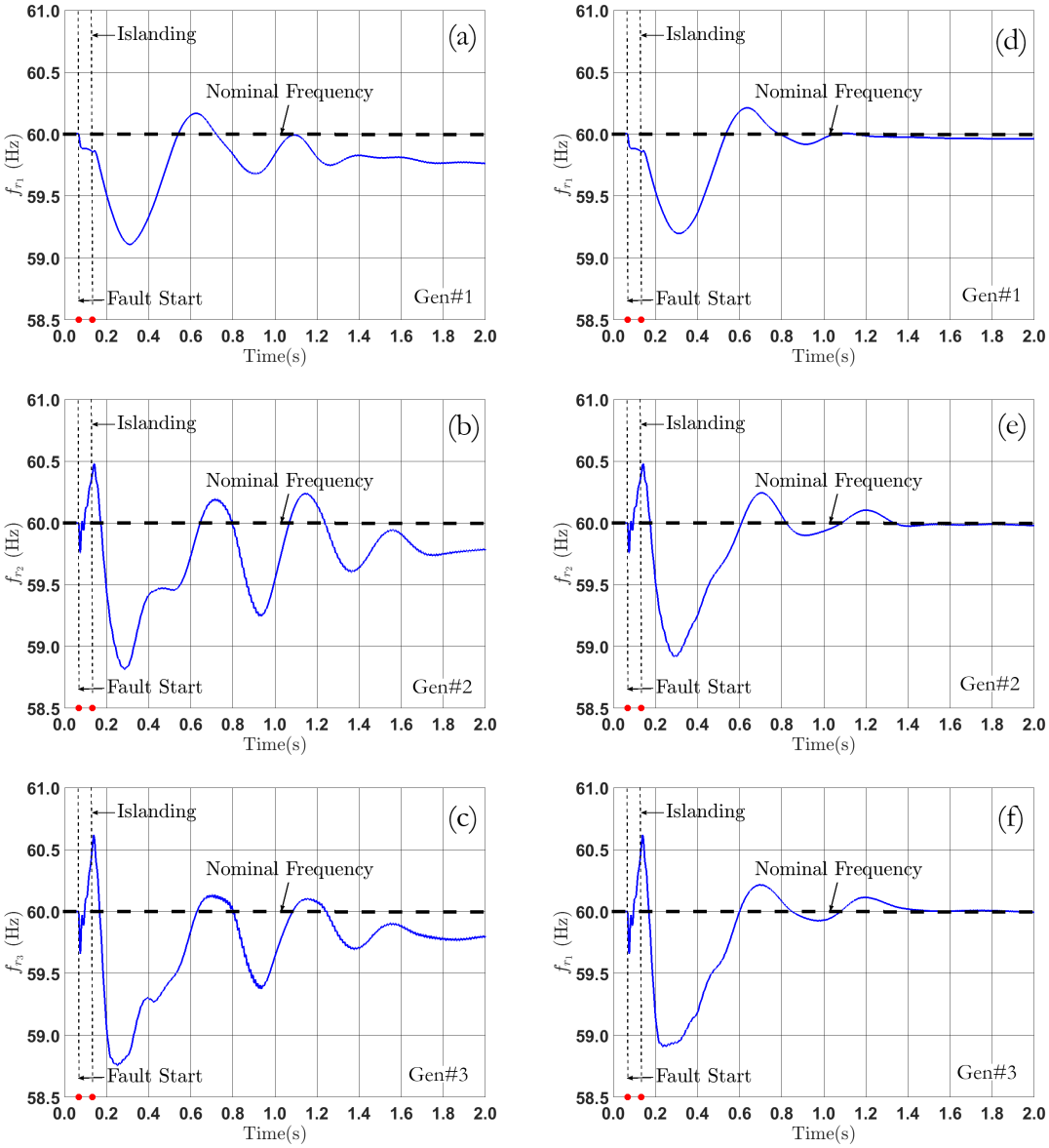

Figure 6.5: The synchronous generators rotor frequency f_r (Hz) vs. time; (left column): unstable under secondary controller with $K_I = 3000$, (right column): stable under secondary controller with adaptive gain using $K_B = 3 \times 10^5$: (a) f_{r_1}: 5 MVA hydroelectric generator, unstable; (b) f_{r_2}: 1.8 MVA diesel generator, unstable; (c) f_{r_3}: 3.125 MVA diesel generator, unstable; (d) f_{r_1}: 5 MVA hydroelectric generator, stable; (e) f_{r_2}: 1.8 MVA diesel generator, stable; (f) f_{r_3}: 3.125 MVA diesel generator, stable

6.2.2 Case#B: Microgrid with and without BESSs - A comparison study

Case #B performs two simulations based on the case #A topology, Fig.6.1. The renewable generators are assumed to have a zero output power during both simulations and hence their impacts can be omitted in this case study. The first simulated microgrid has both synchronous generators and BESSs. The second simulation is done with only synchronous generators. It can be thought as if each $6\ MVA$ BESS in Fig.6.1 is being replaced by two diesel generators (each generator size is $3.125\ MVA$) with droop setting $R_s = 1\%$ to ensure a similar generating capacity in both microgrids. Meanwhile, they are in the standby mode during the beginning of the simulation (zero output power) similar to three BESSs in case #A. The microgrid is formed under the same contingency as in the case#A. Since the fundamental difference between two simulation scenarios is their microgrid generator types, comparing two simulation results will provide good insights for the effects of BESSs on the microgrid performance.

Fig. 6.6 summarizes the rotor speeds for Fig. 6.1's three synchronous generators, under the situation either with or without BESSs. With the BESSs help, all three generators' rotors are returned to their nominal value in one second. Without the BESSs, all three generators experience a frequency deviation that is close to $2\ Hz$, despite the higher system inertia contributed by the additional diesel generators.

Looking at the IMs speed, Fig. 6.7, one will notice that all IMs can recover their speed in both simulations. Nonetheless, the scenario with BESSs has a faster IMs speed recovery thanks to a faster PCCs voltage regulation provided by the BESS's converters. One interesting observation is that the IMs' speed dips are less in the case with only synchronous generators likely because of the higher system inertia. This indicates the possible trade-off between the system rotational inertia and BESS's fast power response.

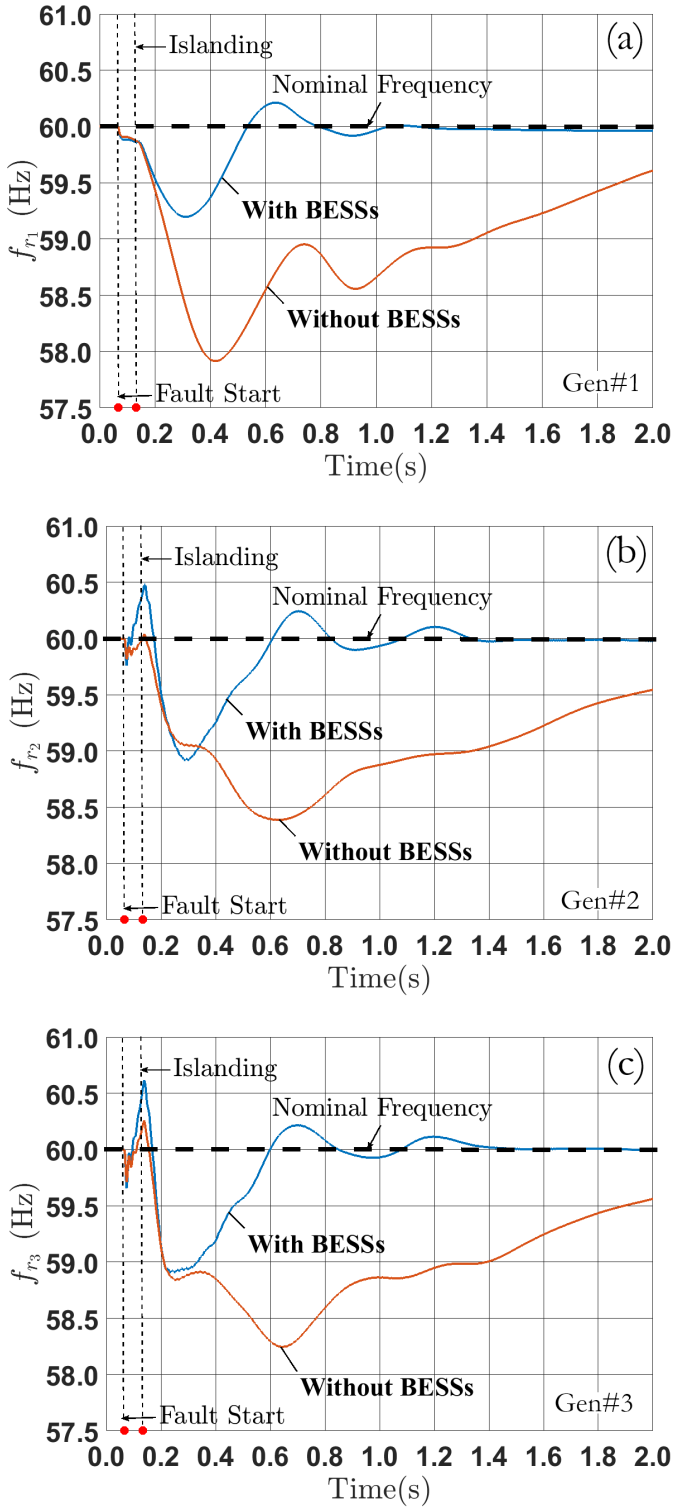

Figure 6.6: The synchronous generators rotor frequency f_r (Hz) vs. time; with and without BESSs: (a) f_{r_1}: 5 MVA hydroelectric generator; (b) f_{r_2}: 1.8 MVA diesel generator; (c) f_{r_3}: 3.125 MVA diesel generator

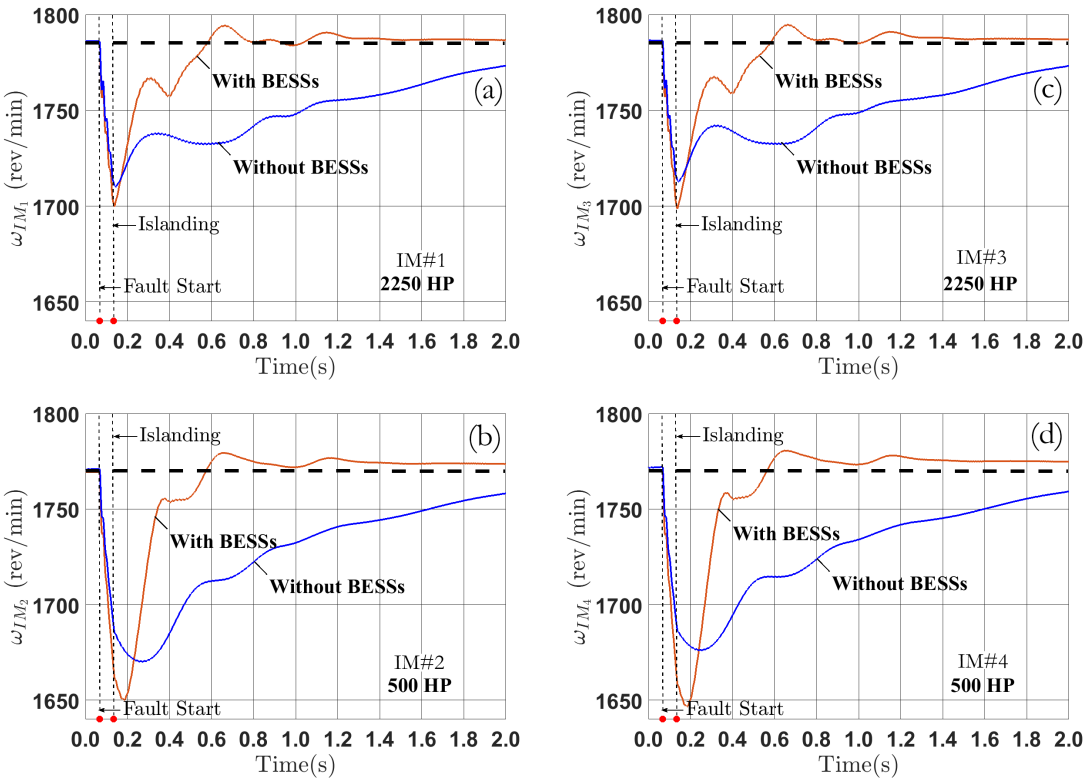

Figure 6.7: Induction motors speed ω_{IM} vs. time, with and without BESSs: (a) ω_{IM_1}: 2250 HP; (b) ω_{IM_2}: 500 HP; (c) ω_{IM_3}: 2250 HP; (d) ω_{IM_4}: 500 HP

Figure 6.8 shows that the PCCs voltage will have a higher value during the fault in the case without BESSs due to the higher short-circuit MVA contributed by the additional synchronous generators. However, the voltage takes significant longer time to recover after the fault clear because the synchronous generators' excitation system response speed is much slower than the BESS's voltage regulating action [122]. Comparing with the rapid voltage recovery in the case with BESSs, it clearly demonstrates the effectiveness of the BESSs control on the microgrid voltage quality and stability enhancement.

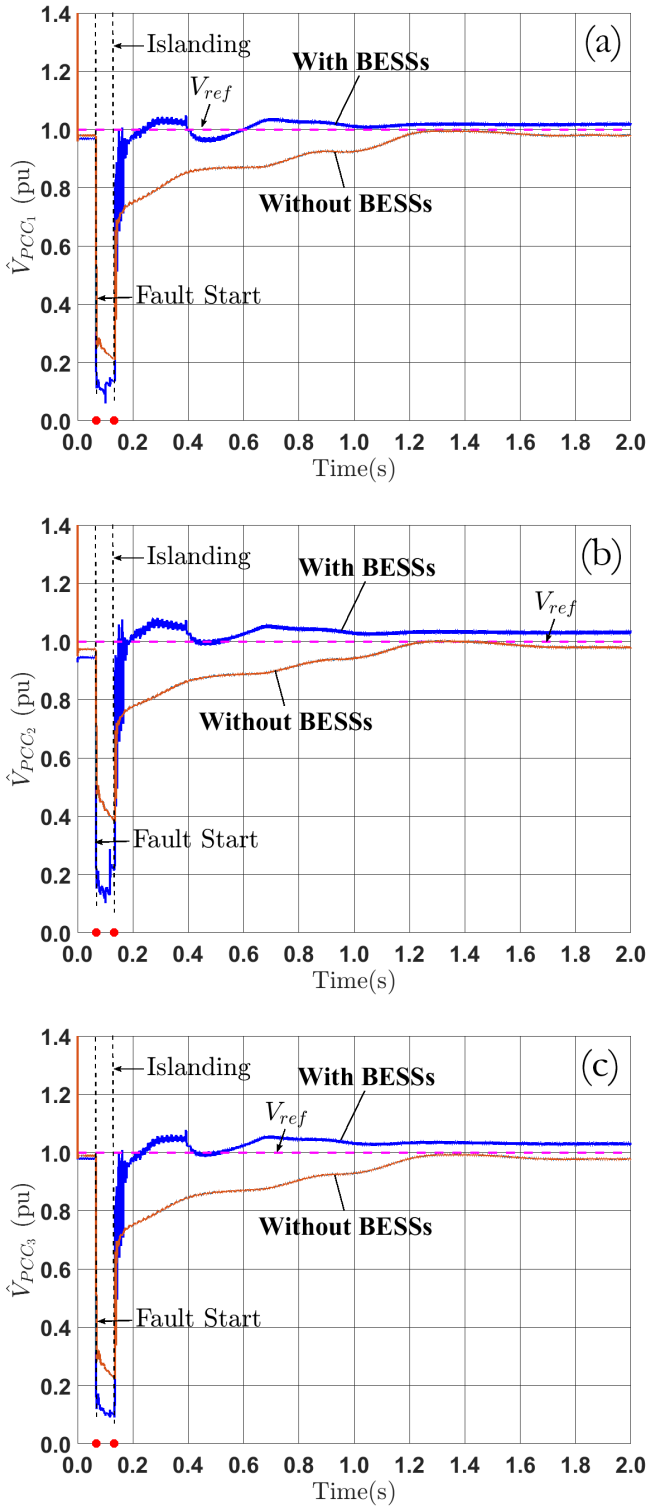

Figure 6.8: The PCCs voltage magnitude $\hat{V}_{PCC}$ vs. time; with and without BESSs: (a) $\hat{V}_{PCC_1}$; (b) $\hat{V}_{PCC_2}$; (c) $\hat{V}_{PCC_3}$

6.2.3 Case#C: Impact of asymmetrical fault

The proposed control strategies are further tested under an $asymmetrical$ fault of Single Line-to-Ground type. All three BESSs are operated under adaptive frequency control with nonlinear droop $R_c = 3\%$ and secondary adaptive gain with $K_B = 1 \times 10^5$ which corresponds to $K_I(|\Delta f|) = 1000$ at $|\Delta f| = 1\%$ (0.6 Hz). The fault location and starting moment are the same as in the previous case #A and #B, except the clearing time in this case is 12 cycles (8 cycles longer). Fig. 6.9 to 6.12 summarize the BESSs and microgrid dynamics.

Three BESSs' estimated PLL frequencies are plotted in Fig. 6.9. It shows that all three frequency estimations are stable and quickly return to nominal value with the help of BESSs after the fault disturbance. Three BESSs' power fluctuates around zero during the fault, Fig. 6.10. Nevertheless, all three BESSs rapidly share the power mismatching in the islanded microgrid and this quickly help all generators' rotor speeds recover to their nominal value as shown in Fig. 6.11. Similarly, Fig. 6.12 illustrates that the microgrid voltages at different nodes can immediately recover within $V_{db} = 5\%$ of its nominal value after the islanding event under the proposed adaptive control strategies.

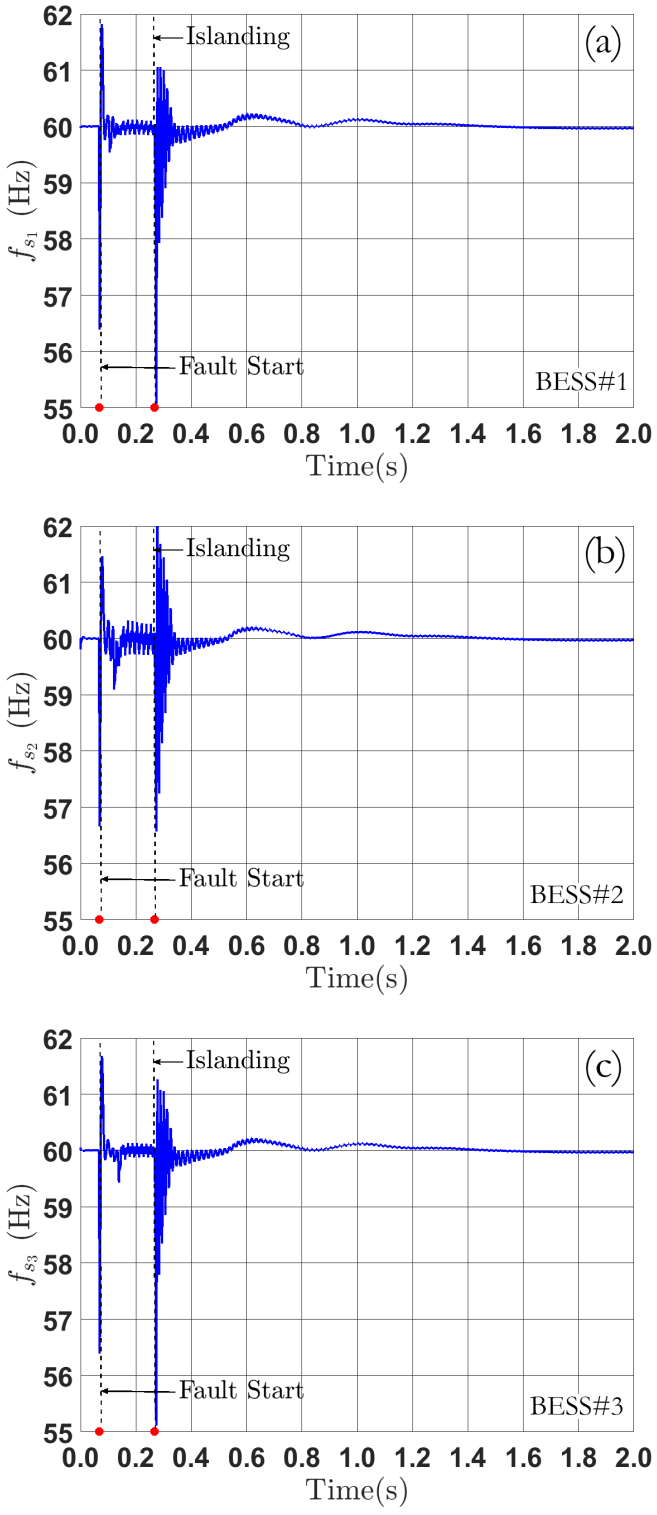

Figure 6.9: Estimated PLL Frequency f_s under 12 cycles *asymmetrical* fault: (a) f_{s_1}; (b) f_{s_2}; (c) f_{s_3}

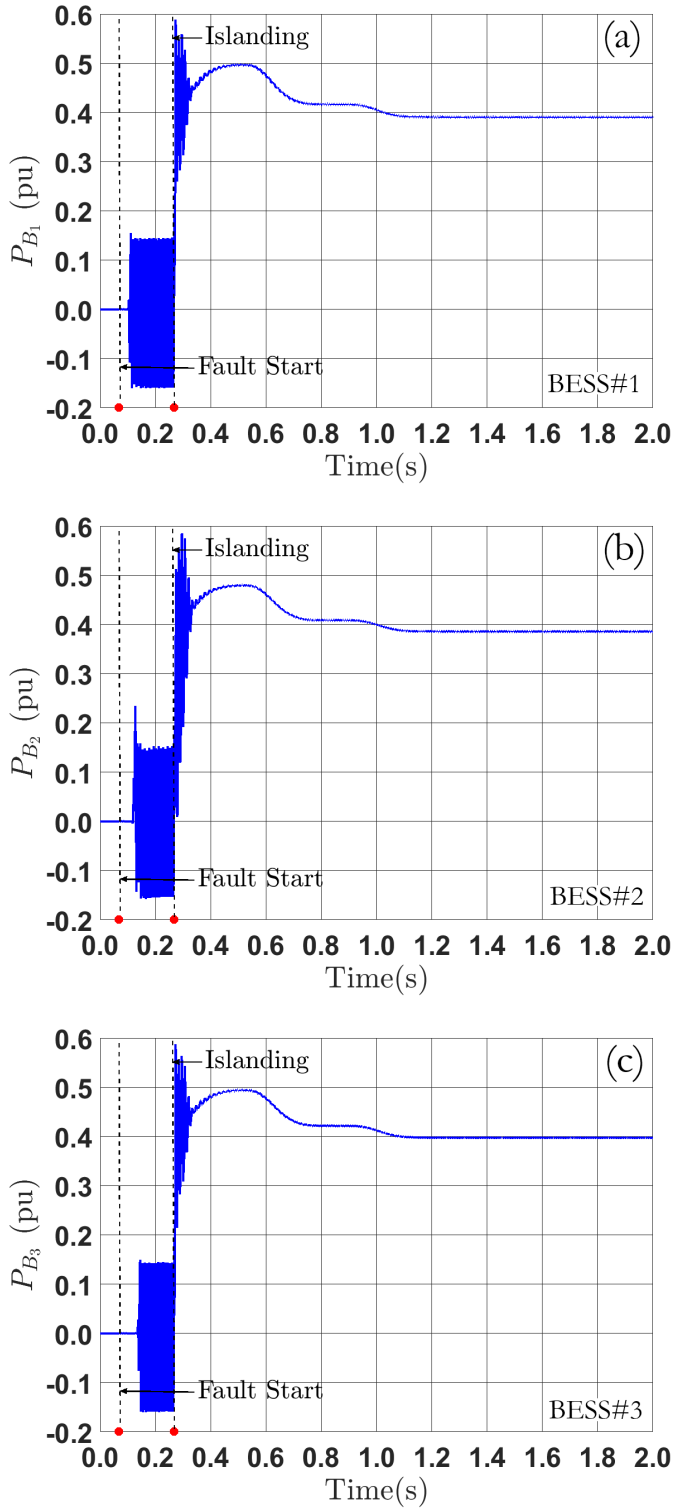

Figure 6.10: The BESSs power vs. time under 12 cycles *asymmetrical* fault: (a) P_{B_1}; (b) P_{B_2}; (c) P_{B_3}

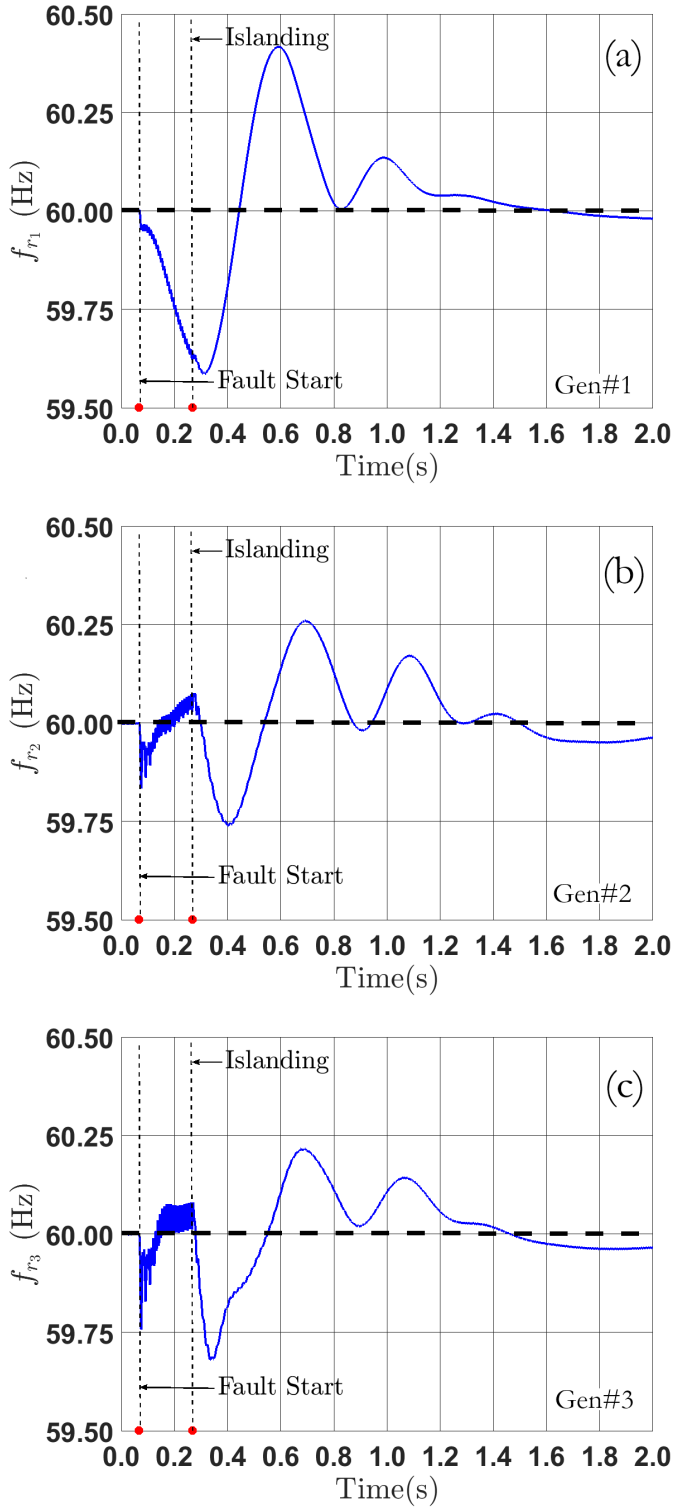

Figure 6.11: The synchronous generators rotor frequency f_r (Hz) vs. time under 12 cycles *asymmetrical* fault: (a) f_{r_1}: 5 MVA hydroelectric generator; (b) f_{r_2}: 1.8 MVA diesel generator; (c) f_{r_3}: 3.125 MVA diesel generator

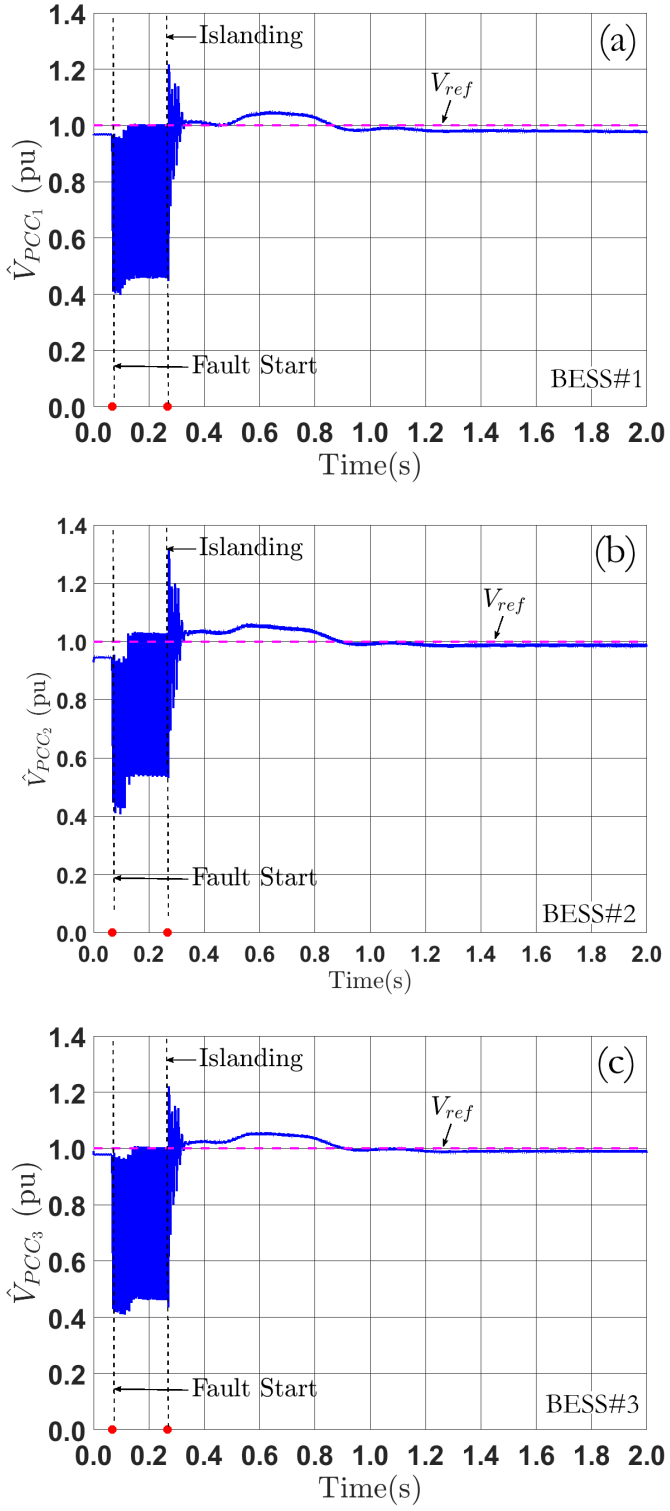

Figure 6.12: The PCCs voltage magnitude $\hat{V}_{PCC}$ vs. time under 12 cycles *asymmetrical* fault: (a) $\hat{V}_{PCC_1}$; (b) $\hat{V}_{PCC_2}$; (c) $\hat{V}_{PCC_3}$

6.2.4 Case#D: Multiple faults and renewable generation

The final case performs a $10\ s$ simulation with the system configuration shown in Fig. 6.1. The BESSs controllers have the same settings as in the case #C. The system experiences two faults. The first contingency is the same as in case #A and #B, which happens 4 cycles after the simulation begins. This leads to the fault-induced islanding 4 cycles later, at $t = 0.133\ s$. The second three-phase fault happens at $t = 3.567\ s$ inside the islanded microgrid close to bus #6. It is cleared by opening switches S_3 and S_4 at $t = 3.617\ s$, 3 cycles after the fault. As a result of this feeder switching induced by the second fault, the microgrid's topology changes. In addition, both renewable generators have their random power output with fast ramp rates as shown in Fig. 6.13. It is evident that the second fault inside the microgrid causes a glitch at the first renewable generator's power output. The responses of the BESSs and the system performance are summarized in Figs. 6.14 to 6.21.

Figure 6.14 plots three BESSs' estimated PLL frequencies. It shows multiple frequency transients caused by several disturbances. The initial fault leads to the largest frequency excursion in all three PLL estimations. They all quickly return to normal with the help of three BESSs after the islanding. The second fault inside the microgrid causes feeders to switch and results a significant frequency oscillation. Fortunately, the oscillation damps out with the help of both BESSs and power system stabilizer (PSS) equipped at the hydroelectric generator's excitation system. With the BESSs adaptive frequency regulation, the frequency fluctuations are negligible under unpredictable power generation from renewable resources. All of these observations clearly show the robustness of the proposed control strategies inside a microgrid with dynamic changing environments.

The BESSs output current in time during the above events are captured in Fig. 6.15, which includes d/q components and the resulted total current magnitude. It shows the autonomous frequency and voltage regulation actions of the three BESSs within their

current capacities. The associated real and reactive power responses are plotted in Figs. 6.16 and 6.17. All three figures clearly show the impacts of multiple disturbances on the responses of all BESSs. Similar to the previous cases, all three BESSs share the real power for a collaborative frequency regulation action. However, due to the different BESSs locations, the reactive power is not shared autonomously. Nevertheless, the microgrid stability is enhanced significantly with all four IM's speed successfully recovered under BESSs' contributions, Fig. 6.18.

Three generators' rotor frequencies are plotted in Fig. 6.19. Two faults cause significant rotor speed disturbances. The second fault has a great impact on the islanded microgrid's frequency. The hydroelectric generator rotor oscillation is damped with the help of the PSS. Under the adaptive frequency regulation of the BESSs, all of generators' rotors are returning to the nominal $60\ Hz$ shortly after the faults are cleared. Moreover, all generators' speed varies less than $0.2\ Hz$ even under the rapid random power output from the renewable resources (e.g., P_{RE_1} has a step change of $3.5\ MW$ at $t = 5\ s$, it also ramps up at a rate of $4\ MW/s$, $7.0 < t < 7.5\ s$).

Three PCCs voltage magnitudes are presented in Fig. 6.20. Two faults cause significant voltage sags. Nevertheless, all of them quickly recover to the nominal value with the help from BESSs' voltage regulator. One can also clearly see the voltage magnitudes oscillations resulted from the generators' excitation systems responses and rotor dynamics, $3.65 < t < 5.00\ s$.

Finally, Fig. 6.21 depicts the magnified PCCs voltage oscillograms before, during and after two faults, $0.05 < t < 0.45\ s$ and $3.5 < t < 3.9\ s$. Thanks to the BESSs voltage regulation action, it demonstrates the rapid voltage recovery with a high waveform supply quality under both faults at all three PCCs locations inside the microgrid. It illustrates that the microgrid resiliency is significantly enhanced with the help of proposed adaptive energy storage control methods even under multiple large disturbances.

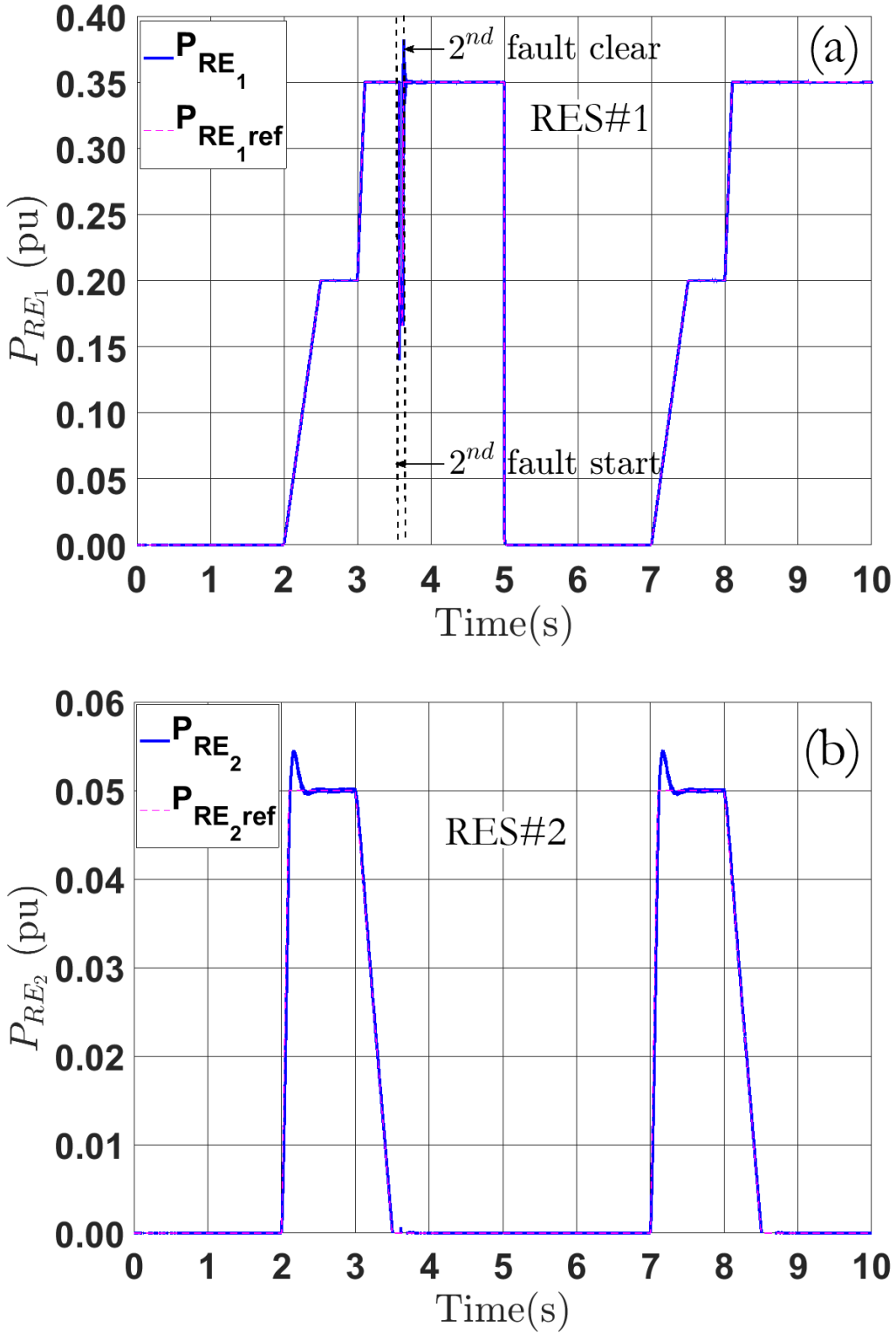

Figure 6.13: Renewable Energy Power Output P_{RE} under multiple faults (4 and 3 cycles fault clearing time respectively): (a) P_{RE_1}; (b) P_{RE_2}

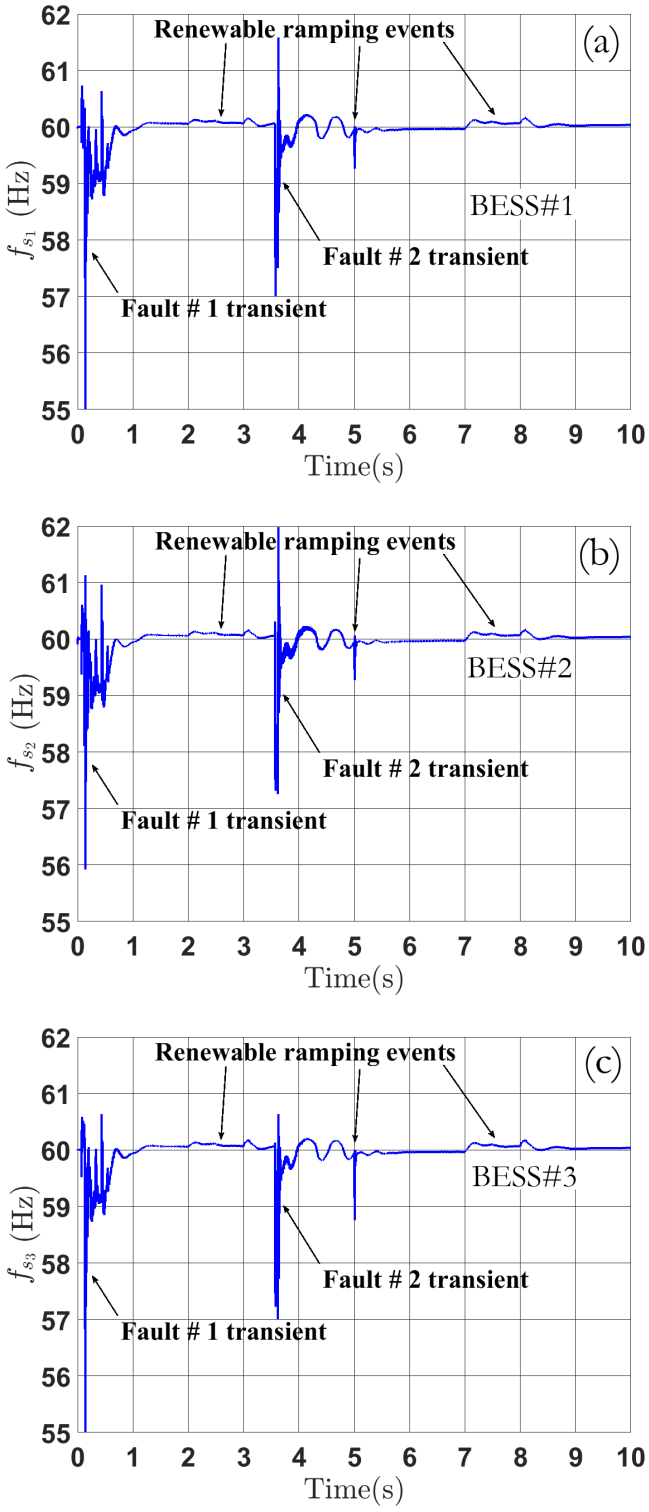

Figure 6.14: Estimated PLL Frequency f_s under multiple faults and renewable generation ramping events with normal voltage regulation: (a) f_{s_1}; (b) f_{s_2}; (c) f_{s_3}

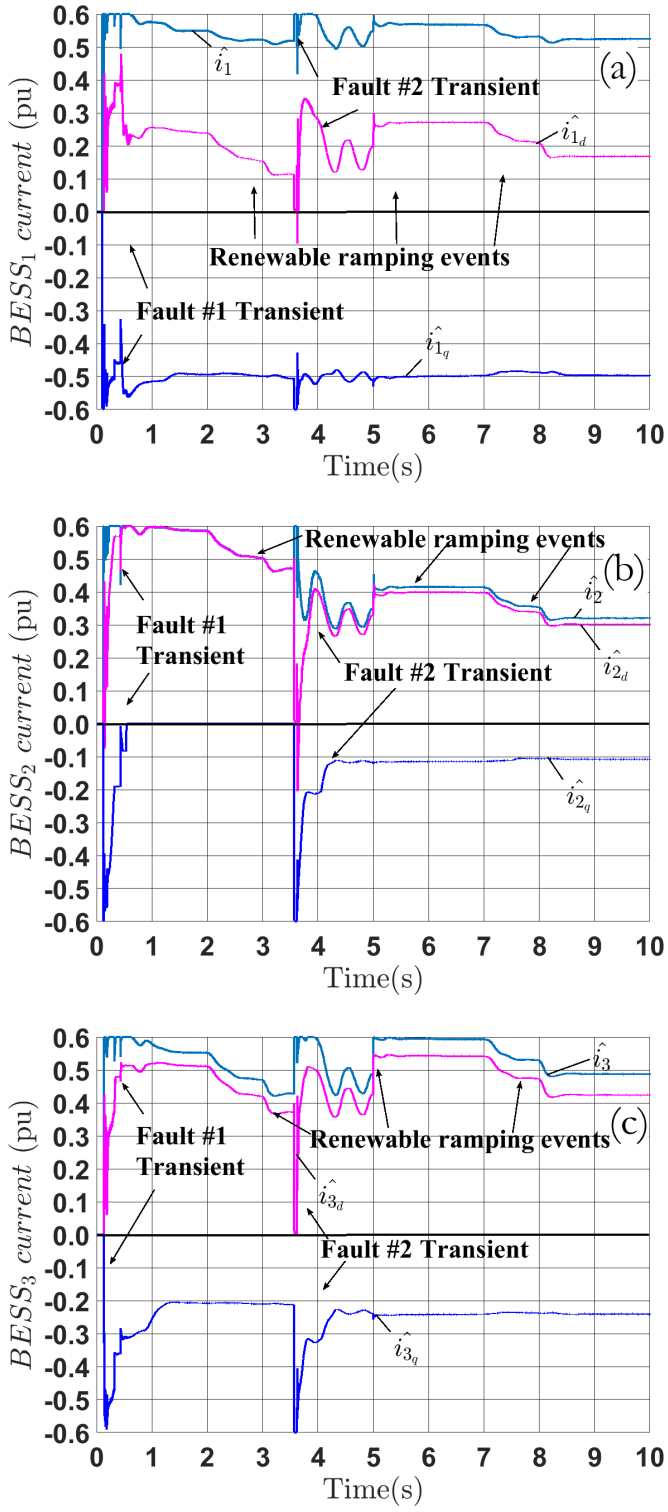

Figure 6.15: BESSs current magnitudes transients under multiple faults and renewable generation ramping events with normal voltage regulation: (a) $BESS_1$; (b) $BESS_2$; (c) $BESS_3$

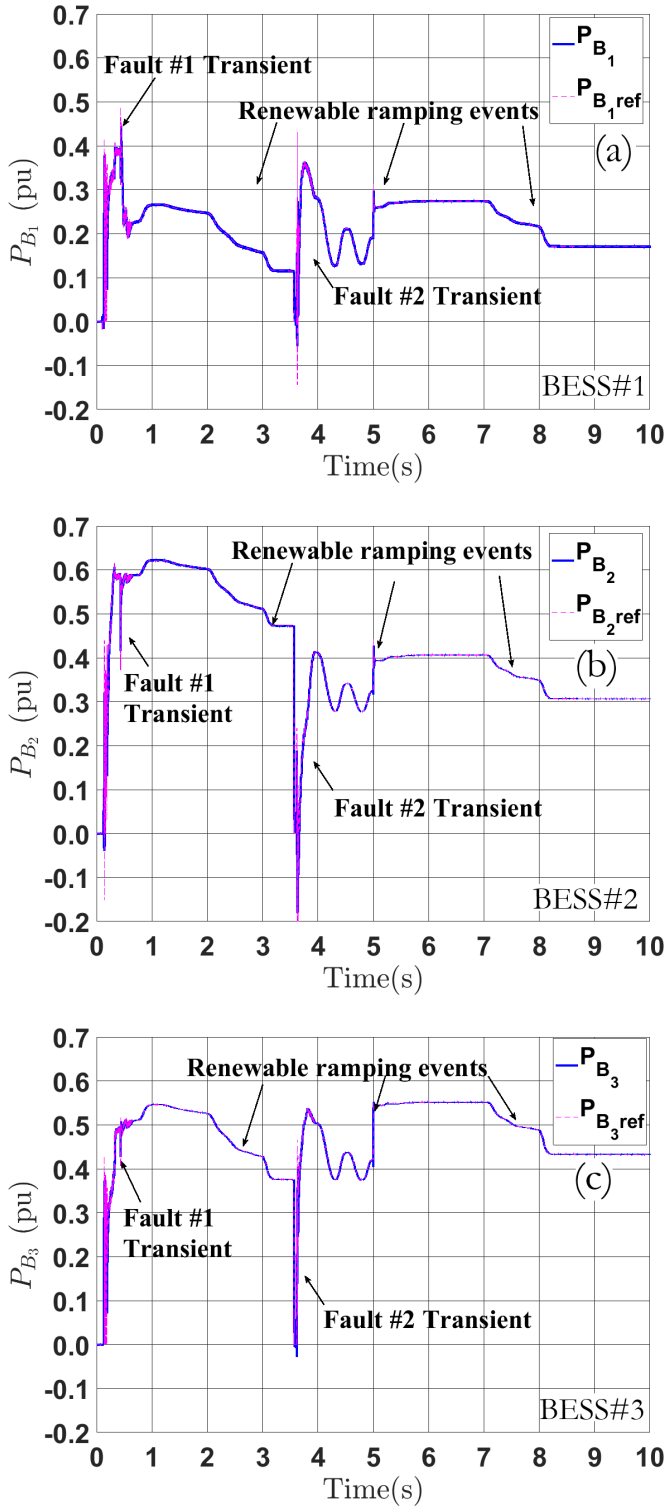

Figure 6.16: BESSs real power vs. time under multiple faults and renewable generation ramping events with normal voltage regulation: (a) P_{B_1}; (b) P_{B_2}; (c) P_{B_3}

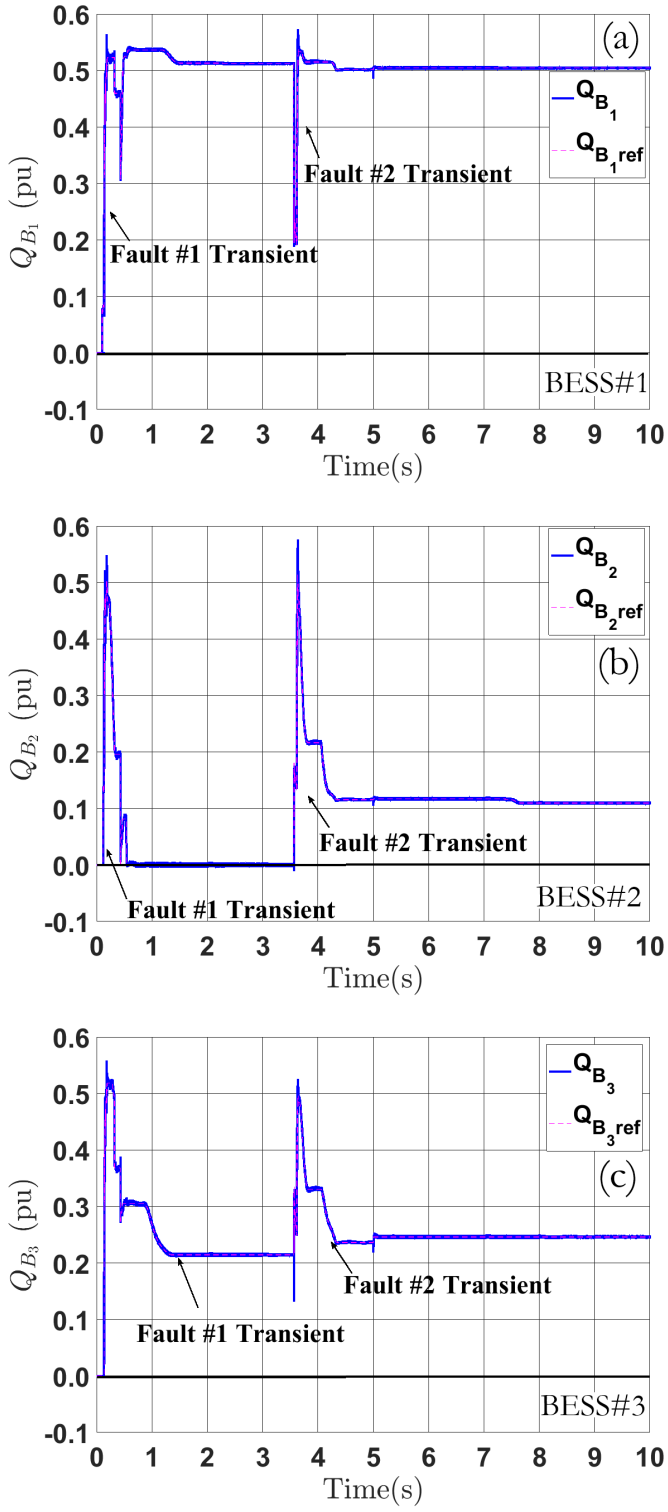

Figure 6.17: BESSs reactive power vs. time under multiple faults and renewable generation ramping events with normal voltage regulation: (a) Q_{B_1}; (b) Q_{B_2}; (c) Q_{B_3}

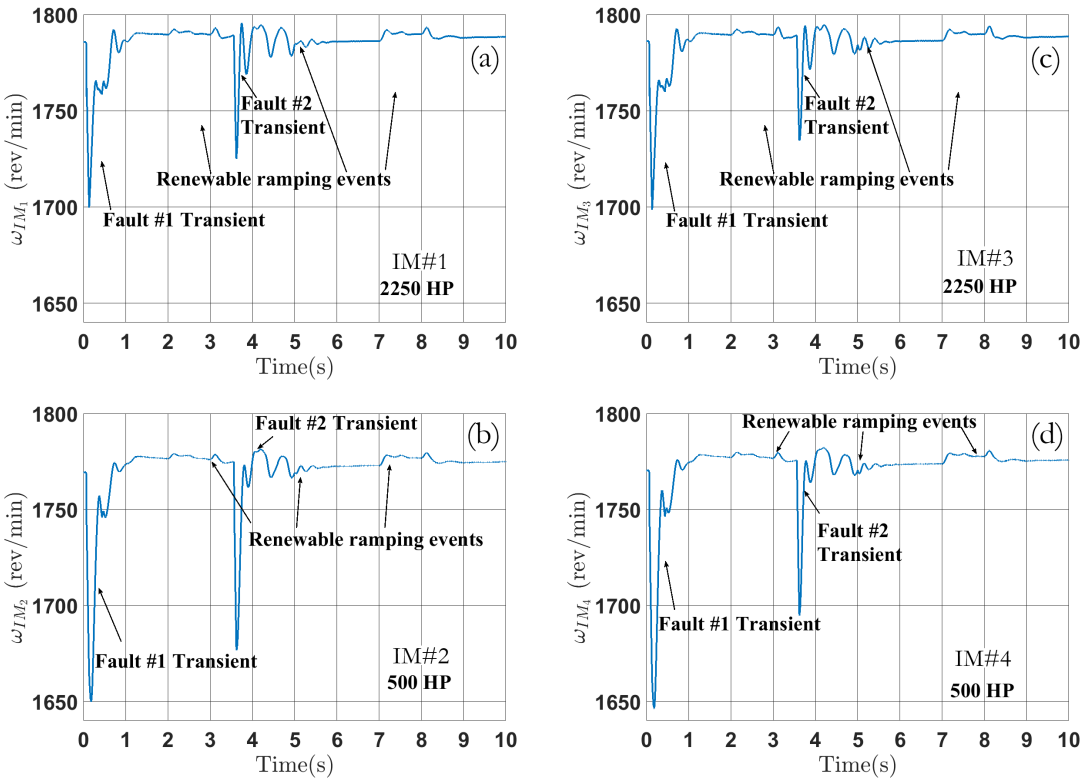

Figure 6.18: Induction motors speed ω_{IM} vs. time, under multiple faults and renewable generation ramping events with normal voltage regulation: (a) ω_{IM_1}: 2250 HP; (b) ω_{IM_2}: 500 HP; (c) ω_{IM_3}: 2250 HP; (d) ω_{IM_4}: 500 HP

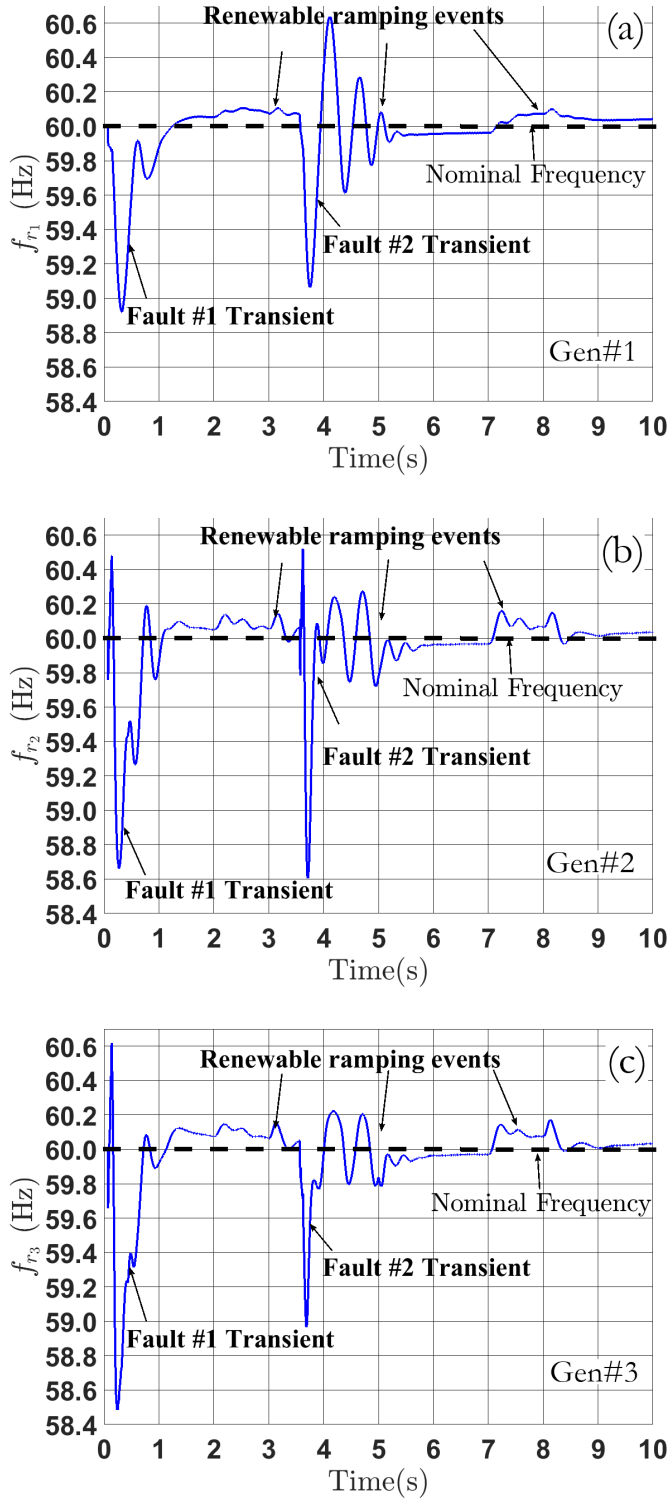

Figure 6.19: The synchronous generators rotor frequency f_r (Hz) vs. time under multiple faults and renewable generation ramping events with normal voltage regulation: (a) f_{r_1}: $5\ MVA$ hydroelectric generator; (b) f_{r_2}: $1.8\ MVA$ diesel generator; (c) f_{r_3}: $3.125\ MVA$ diesel generator

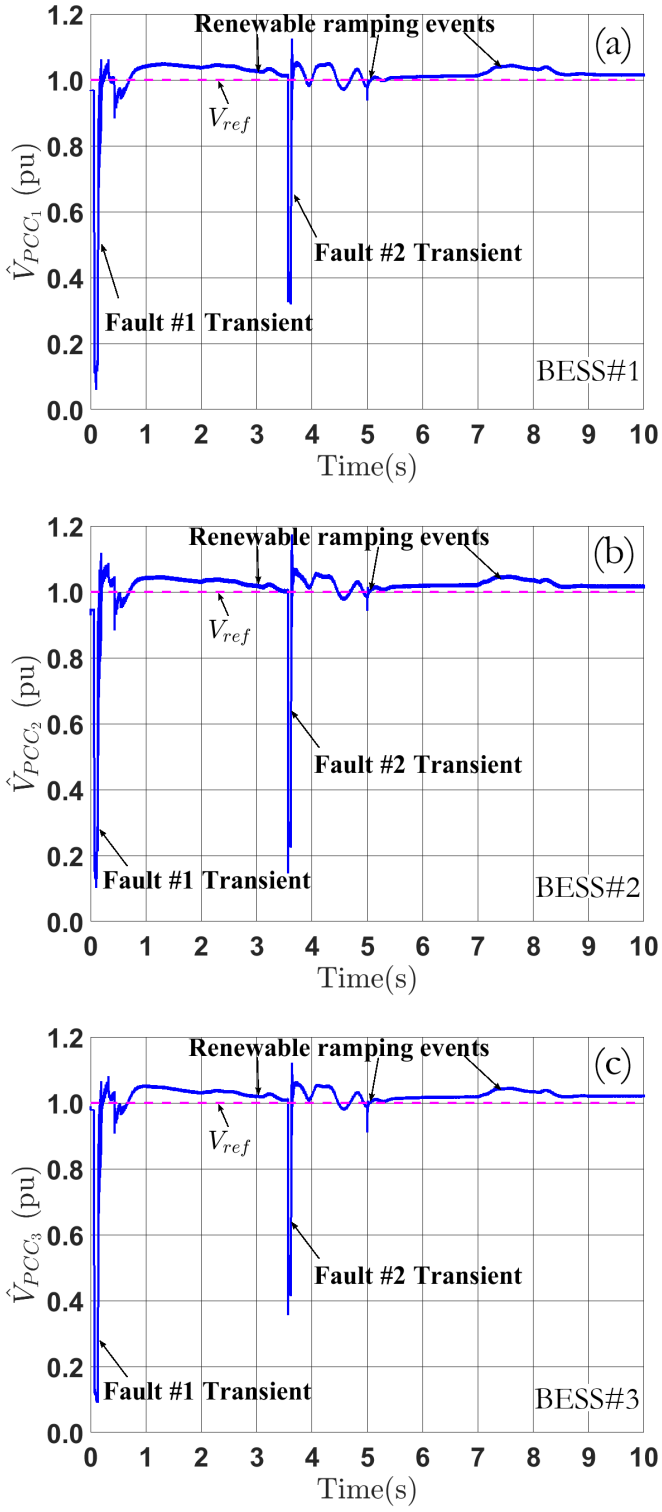

Figure 6.20: The PCCs voltage magnitude $\hat{V}_{PCC}$ vs. time under multiple faults and renewable generation ramping events with normal voltage regulation: (a) $\hat{V}_{PCC_1}$; (b) $\hat{V}_{PCC_2}$; (c) $\hat{V}_{PCC_3}$

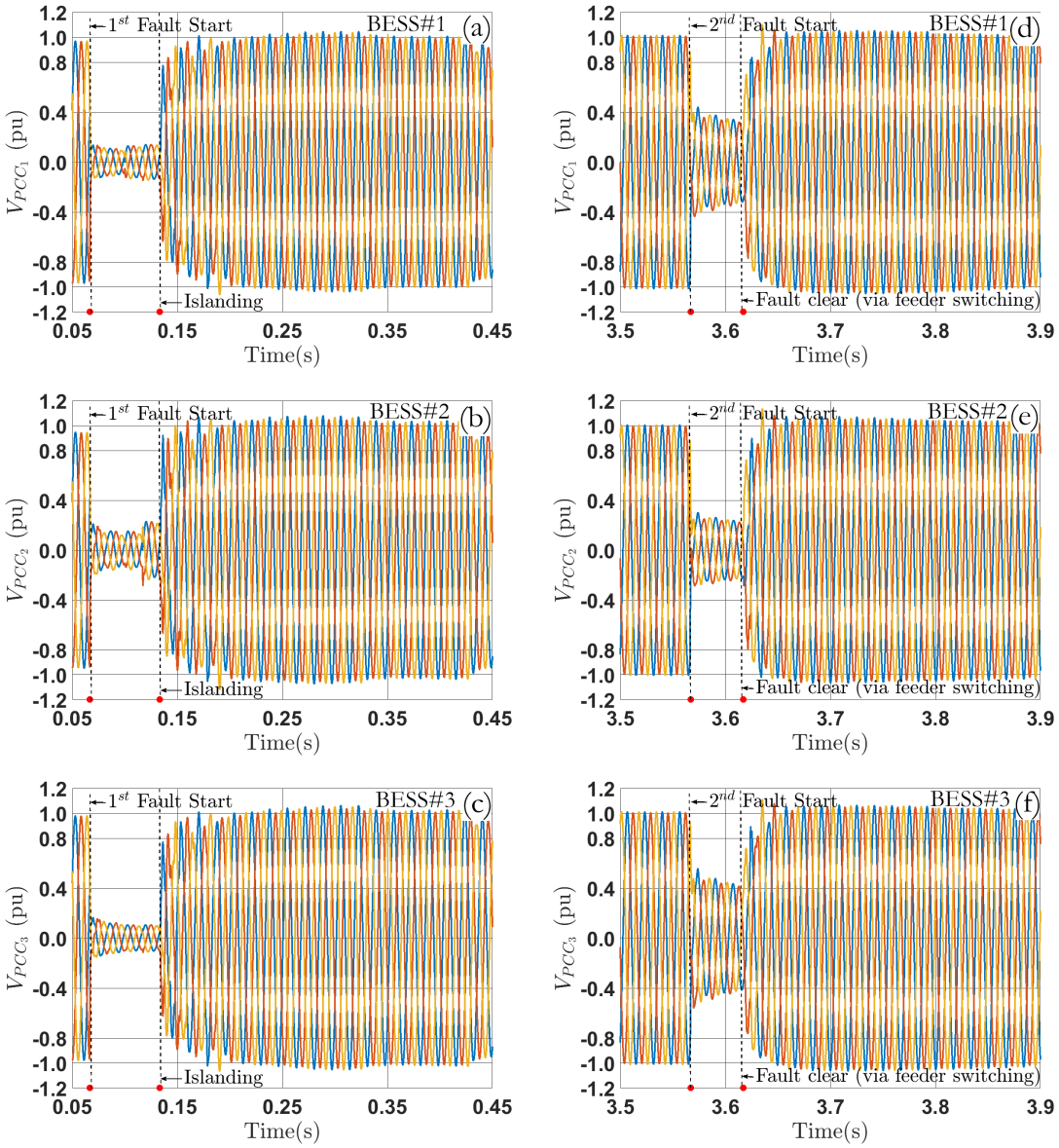

Figure 6.21: Magnified PCC voltage oscillogram vs. time under multiple faults and renewable generation ramping events with normal voltage regulation: (a) V_{PCC_1}, first fault-induced islanding transient, $0.05 < t < 0.45$ s; (b) V_{PCC_2}, first fault-induced islanding transient, $0.05 < t < 0.45$ s; (c) V_{PCC_3}, first fault-induced islanding transient, $0.05 < t < 0.45$ s; (d) V_{PCC_1}, second (islanding) fault-induced feeder switching transient, $3.5 < t < 3.9$ s; (e) V_{PCC_2}, second (islanding) fault-induced feeder switching transient, $3.5 < t < 3.9$ s; (f) V_{PCC_3}, second (islanding) fault-induced feeder switching transient, $3.5 < t < 3.9$ s

6.3 Study#2: Adaptive Voltage Regulation

Both adaptive frequency and voltage regulations are implemented in this study. Case #A shows the advantages of the adaptive voltage regulation on the microgrid recovery when a prolonged fault clearing is applied. Case #B indicates that it is possible to achieve better microgrid dynamics by including appropriate voltage regulation delays inside the adaptive voltage regulation algorithm.

Fig. 6.1 shows the studied system topology. It also experiences similar transients as in study #1, case #D with the assumption that both faults happen at the same moment ($t = 0.067\ s$ and $t = 3.567\ s$). However, the clearing time of fault#1 takes 7 cycles (3 cycles longer, at $t = 0.183\ s$) and fault#2's clearing time is 4 cycles (1 cycle longer, at $t = 3.633\ s$). Consequently, the BESS #1 and #3 sizes increase to 10 MVA to ensure the stable microgrid operation.

6.3.1 Case#A: Without voltage regulation control delay

In this first case, three BESSs have the same adaptive frequency control settings as in study #1, case #C and #D. The voltage controller $V_{ref}(t)$ is implemented based on Fig. 5.6. The power priority switch control introduced in Fig. 5.7, Ch. 5.4.2, is also in action. The adaptive voltage controller has the following settings: $V_{ref_N} = 1.00\ pu$, $V_{ref_E} = 1.30\ pu$, $V_{db} = 0.05\ pu$, $V_{th_L} = 0.50\ pu$, $V_{th_H} = V_{ref_E} - V_{db} = 1.25\ pu$, $K_R = 7\ V/s$, $t_{rs_1} = 0.100\ s$ (6 cycles), $t_{rs_2} = 0.067\ s$ (4 cycles), $t_{rs_3} = 1.000\ s$, $f_{sw} = 0.01\ pu$ (0.6 Hz), $t_{sw_1} = 0.083\ s$ (5 cycles) and $I_{sat} = 0.90\ I_{max}$. Figs. 6.23 to 6.26 picture the BESSs adaptive control contributions on the overall microgrid stability enhancement.

Two renewable generators' random power outputs are plotted in Fig. 6.22 similar to the previous study case #D. The second fault causes a short disturbance of power gener-

ation at $3.567 < t < 3.633\ s$. Both the multiple faults and the randomness of renewable power test the BESS's controller performance. Three alternators' rotor speeds are evaluated in Fig. 6.23. Similar to the previous study #1, case #D, all synchronous generators' rotor speeds experience large excursions during the faults. One can see that the longer fault durations lead to a greater deviation of rotor speeds. Nevertheless, all three synchronous generators' frequency return to $0.5\ Hz$ within their nominal value in less than one second after the fault clearing under the BESSs' contributions. Even though the system experiences the renewable output power with a $2\ MW$ ramping up in half second ($2.0 < t < 2.5\ s$), their impacts on the microgrid system frequency is inconsequential, Fig. 6.23.

The BESSs' adaptive voltage regulations contribute to a fast PCCs voltage recovery as shown in Fig. 6.24. The fault-induced low voltage conditions activate the adaptive voltage control algorithm. Therefore all three voltage reference signals are ramping up during both faults. This results a higher PCC recovery voltage magnitudes after faults clearing. One will notice that the voltage references ramp down even before the voltage magnitudes reach $V_{th_H} = 1.25\ pu$ during the fault#1 transient (this is not the case in the fault#2). The reasons can be explained as following: the prolonged low voltage condition seen by BESS#1 results an early ramping down of $V_{ref_1}(t)$ (condition 1: insufficient capacity for over-excitation). However, this is not the case for both BESS#2 and #3 and hence their voltage references are still staying at V_{ref_E}. The different voltage references among BESSs eventually lead both the $V_{ref_2}(t)$ and $V_{ref_3}(t)$ back to V_{ref_N}. This action results in a better voltage control coordination (condition 2).

Figure 6.25 depicts the detailed oscillograms for PCCs voltage waveforms during two faults transient, $0.05 < t < 0.45\ s$ and $3.5 < t < 3.9\ s$. It clearly indicates higher recovery voltage magnitudes after the fault clearing showing the effectiveness of adaptive voltage regulation. The waveforms remain sinusoidal despite a short disturbance.

Thanks to the adaptive voltage regulation, all four IMs speeds can ride-through the prolonged faults disturbances during islanding event, Fig. 6.26. Meanwhile, the effects of renewable output power on motor speed variations are inconsequential. Conversely, two 2250 HP motors (IM #1 and #3) under normal voltage regulation cannot recover their speed.

The BESSs responses are summarized in Figs. 6.27 to 6.30. All three BESSs' converters PLL remain stable under several consecutive large disturbances, Fig. 6.27. These frequency transient deviations activate the fast adaptive frequency control, which quickly brings the system frequency back to normal. Since all BESSs are equipped with both adaptive nonlinear droop and secondary control, the frequency regulation actions are very small near the nominal value but significant during the large disturbances. This is favorable for a stable operation of microgrid under a dynamic changing environment. Consequently, the renewable generation causes very little frequency deviations, well within the acceptable range.

One can see the three BESSs rapidly change their output currents during multiple transients as shown in Fig. 6.28. All of them are reaching steady state within a second after each disturbance. During the two faults-on periods, all three BESSs' currents are saturated, indicating that they all contribute their best efforts to enhance microgrid stability. During normal operations, each BESS has an adequate capacity for both voltage and frequency regulations. The associate real and reactive powers are presented in Fig. 6.29 and 6.30. Both figures demonstrate the fast BESSs' regulation actions. In addition, their responses closely follow the corresponding reference signals.

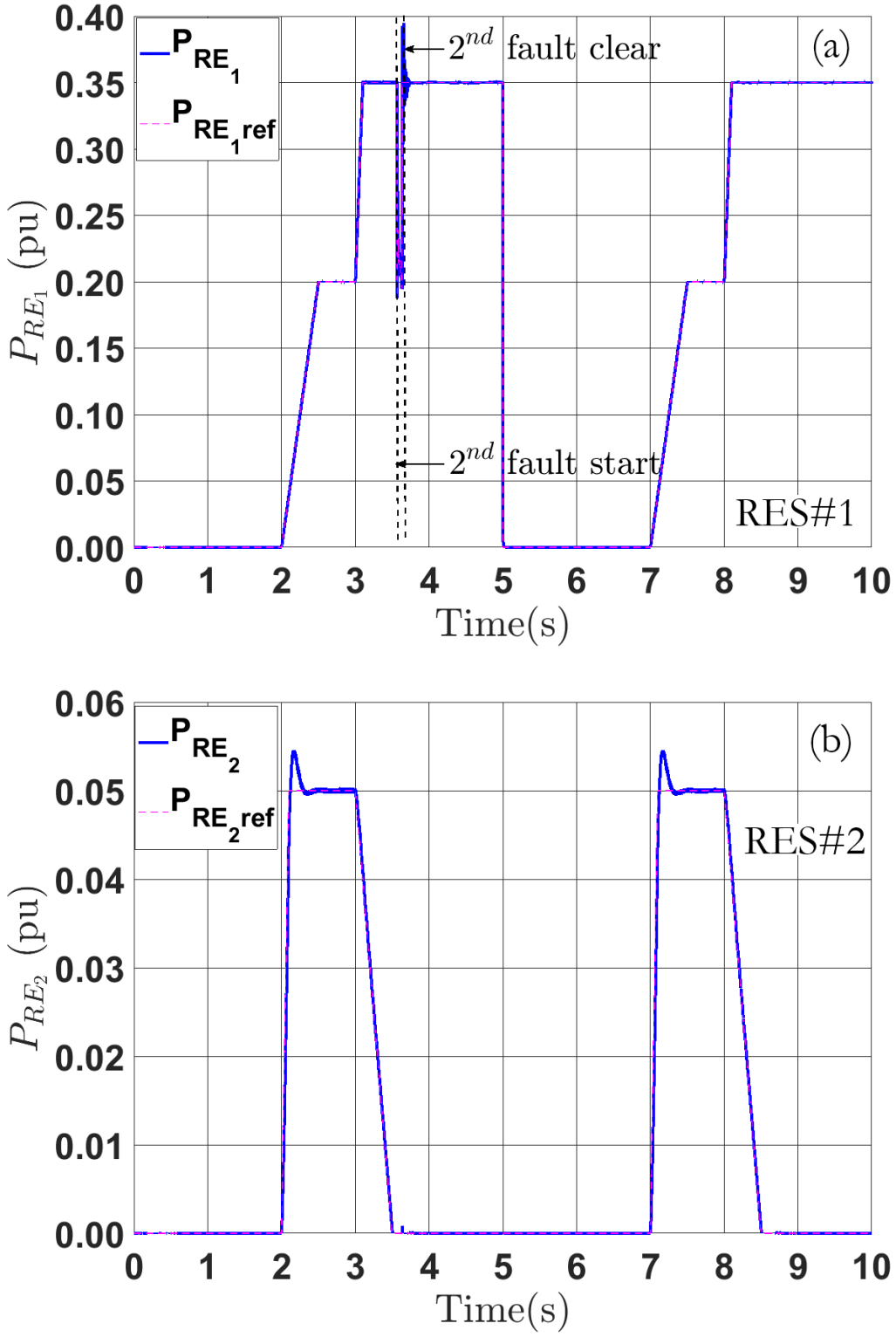

Figure 6.22: Renewable Energy Power Output P_{RE} under multiple (two) faults (7 and 4 cycles fault clearing time respectively): (a) P_{RE_1}; (b) P_{RE_2}

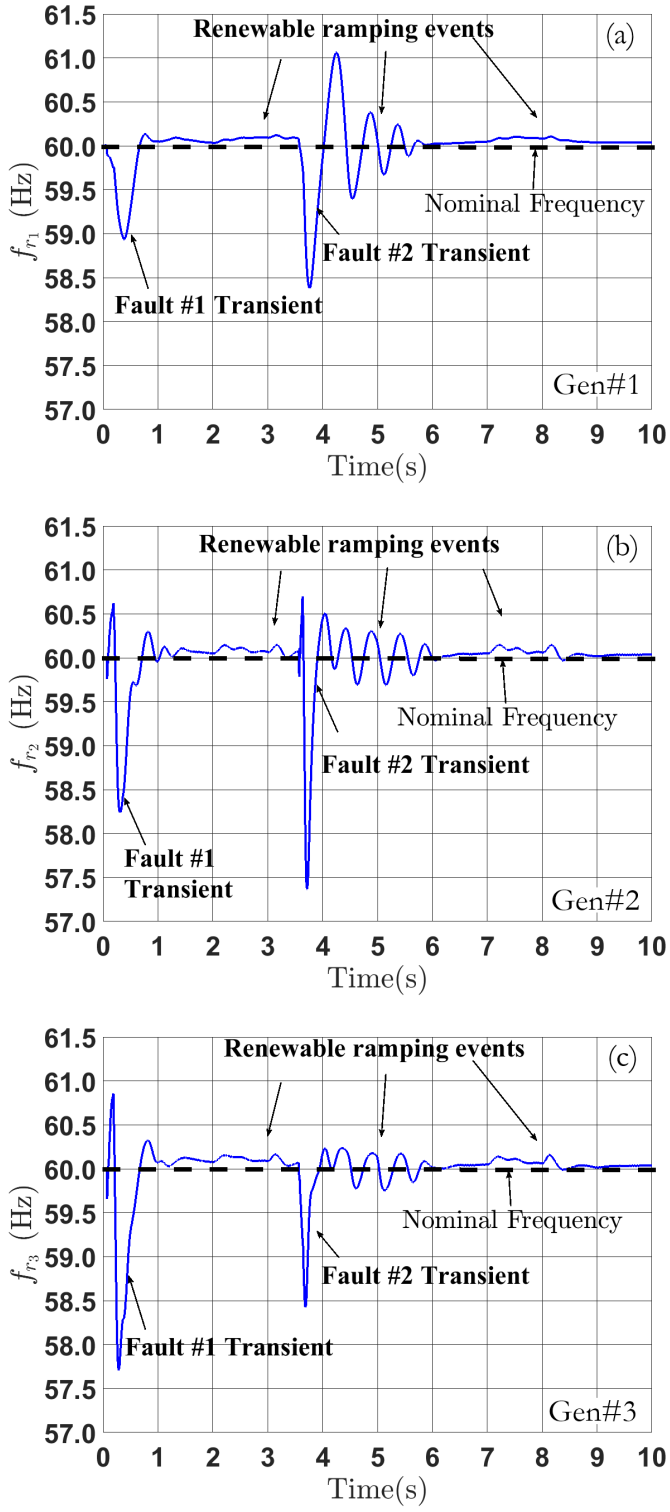

Figure 6.23: The synchronous generators rotor frequency f_r (Hz) vs. time under multiple faults and renewable generation ramping events with adaptive voltage regulation (no regulation delay): (a) f_{r_1}: 5 MVA hydroelectric generator; (b) f_{r_2}: 1.8 MVA diesel generator; (c) f_{r_3}: 3.125 MVA diesel generator

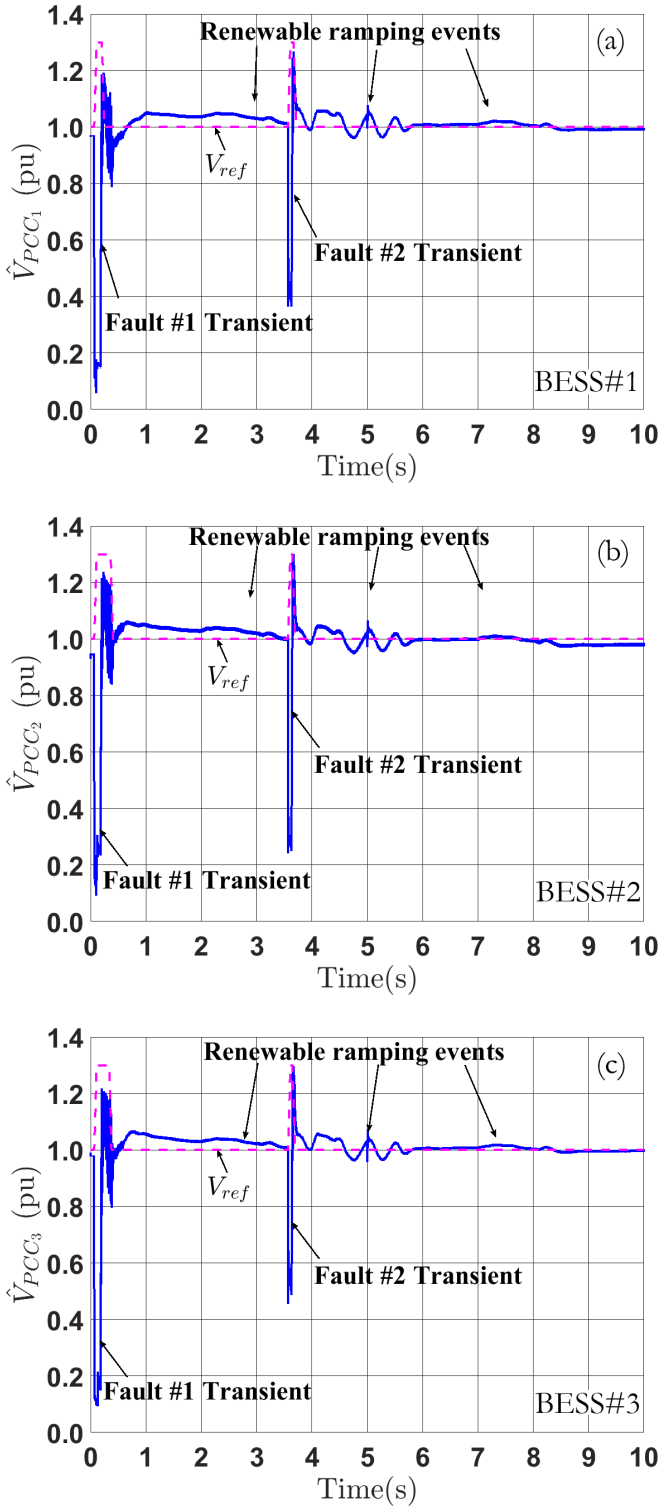

Figure 6.24: The PCCs voltage magnitude $\hat{V}_{PCC}$ vs. time under multiple faults and renewable generation ramping events with adaptive voltage regulation (no regulation delay): (a) $\hat{V}_{PCC_1}$; (b) $\hat{V}_{PCC_2}$; (c) $\hat{V}_{PCC_3}$

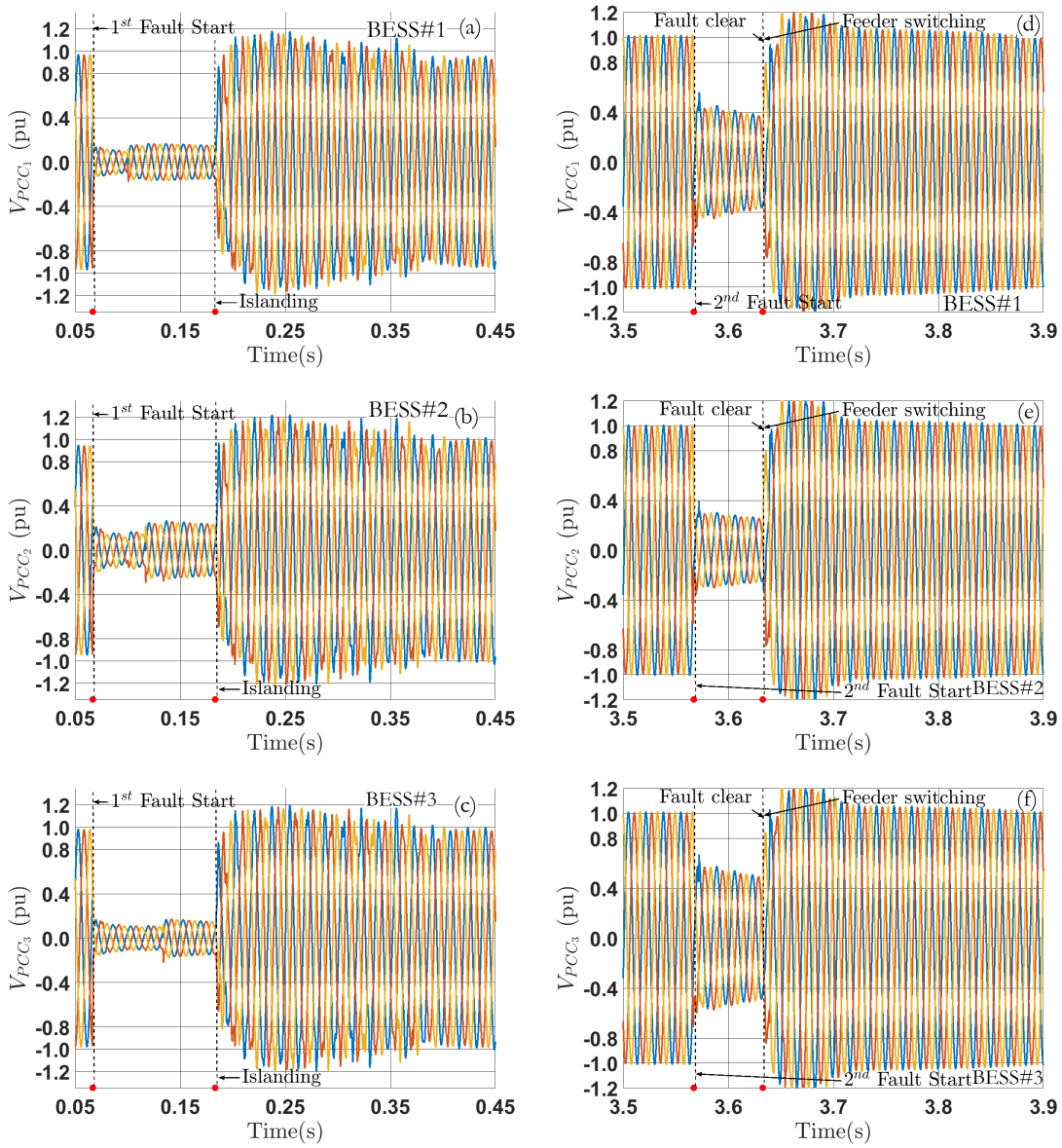

Figure 6.25: Magnified PCC voltage oscillogram vs. time under multiple faults and renewable generation ramping events with adaptive voltage regulation (no regulation delay): (a) V_{PCC_1}, first fault-induced islanding transient, $0.05 < t < 0.45$ s; (b) V_{PCC_2}, first fault-induced islanding transient, $0.05 < t < 0.45$ s; (c) V_{PCC_3}, first fault-induced islanding transient, $0.05 < t < 0.45$ s; (d) V_{PCC_1}, second (islanding) fault-induced feeder switching transient, $3.5 < t < 3.9$ s; (e) V_{PCC_2}, second (islanding) fault-induced feeder switching transient, $3.5 < t < 3.9$ s; (f) V_{PCC_3}, second (islanding) fault-induced feeder switching transient, $3.5 < t < 3.9$ s

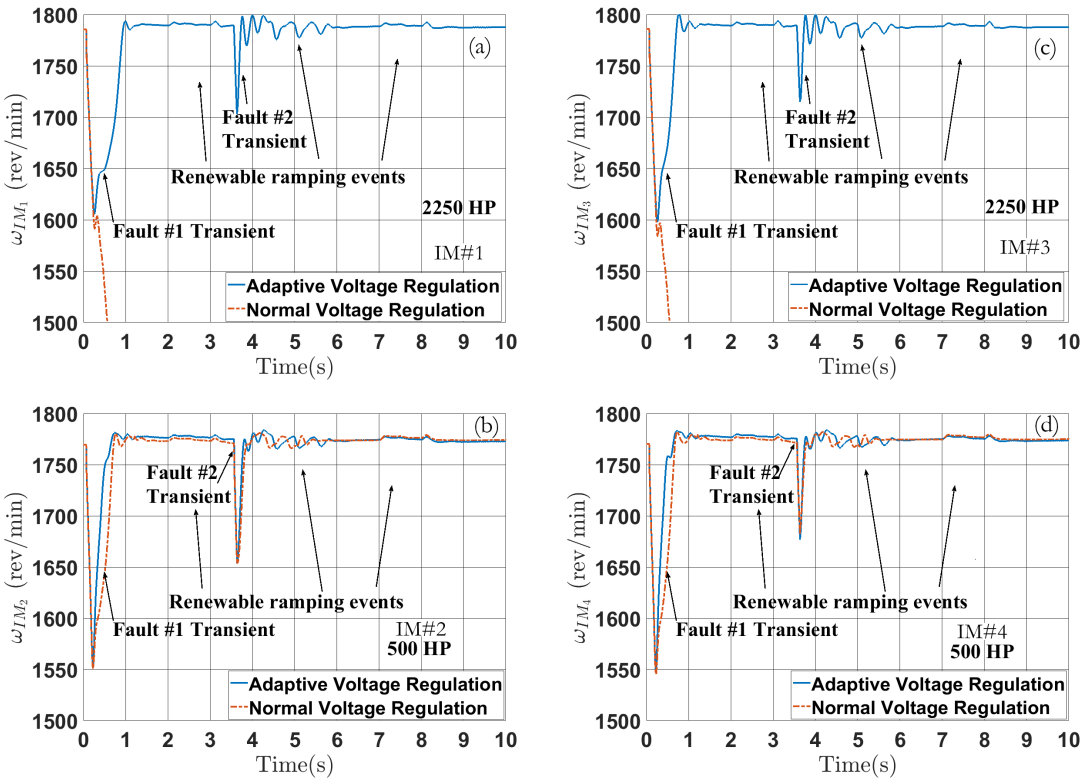

Figure 6.26: Induction motors speed ω_{IM} vs. time, under multiple faults and renewable generation ramping events with adaptive voltage regulation (no regulation delay): (a) ω_{IM_1}: 2250 HP; (b) ω_{IM_2}: 500 HP; (c) ω_{IM_3}: 2250 HP; (d) ω_{IM_4}: 500 HP

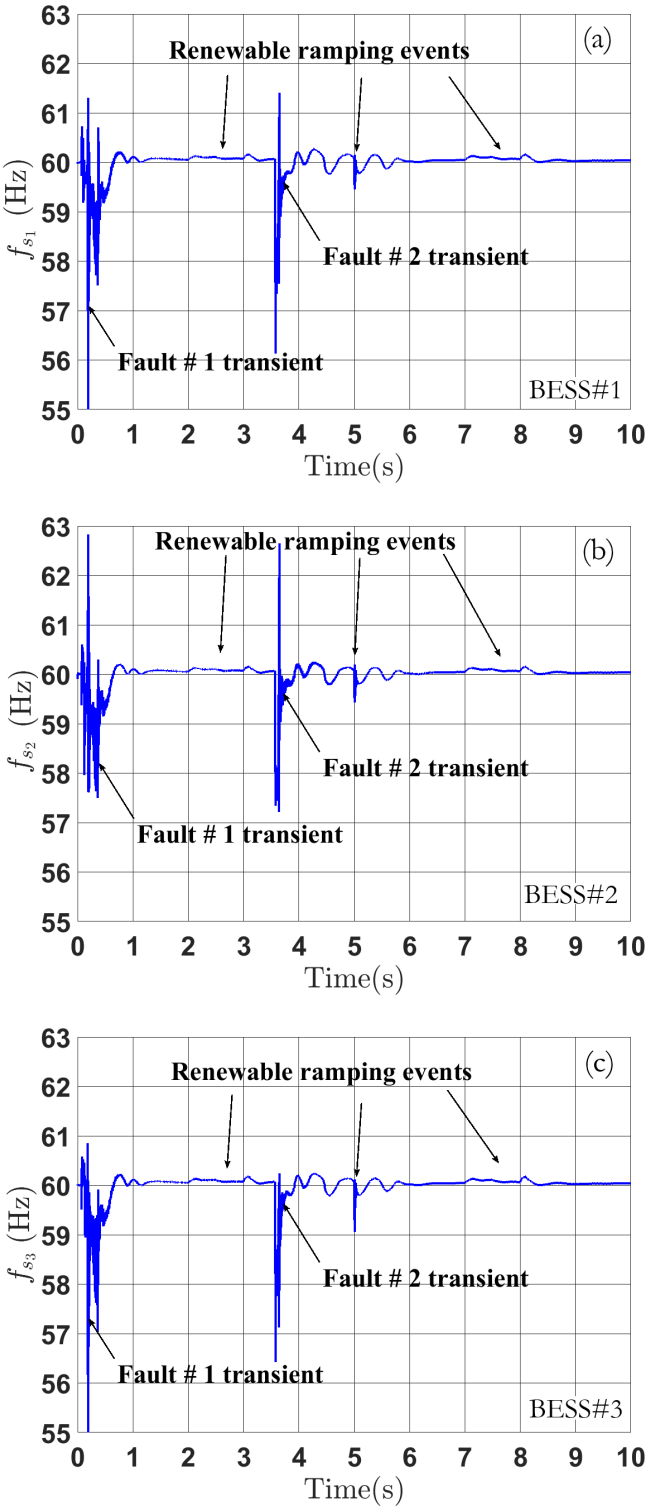

Figure 6.27: Estimated PLL Frequency f_s under multiple faults and renewable generation ramping events with adaptive voltage regulation (no regulation delay): (a) f_{s_1}; (b) f_{s_2}; (c) f_{s_3}

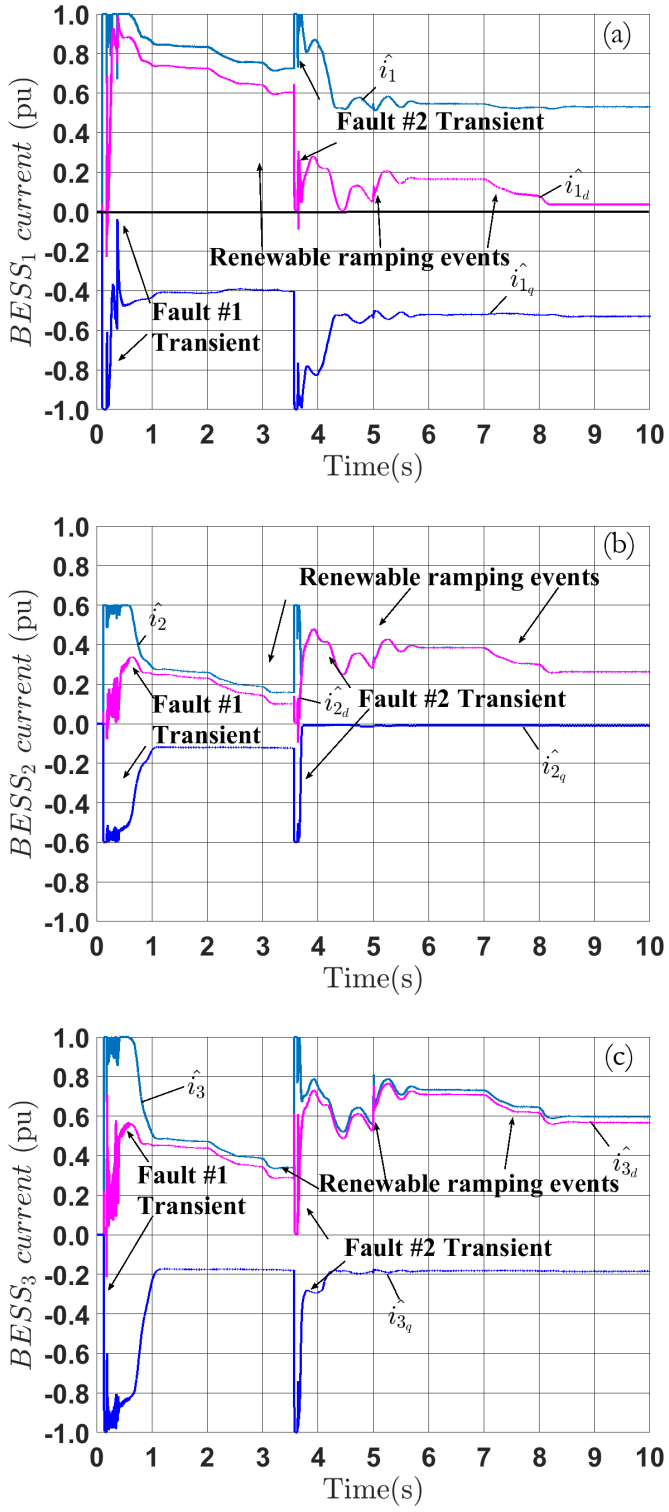

Figure 6.28: BESSs current magnitudes transients under multiple faults and renewable generation ramping events with adaptive voltage regulation (no regulation delay): (a) $BESS_1$; (b) $BESS_2$; (c) $BESS_3$

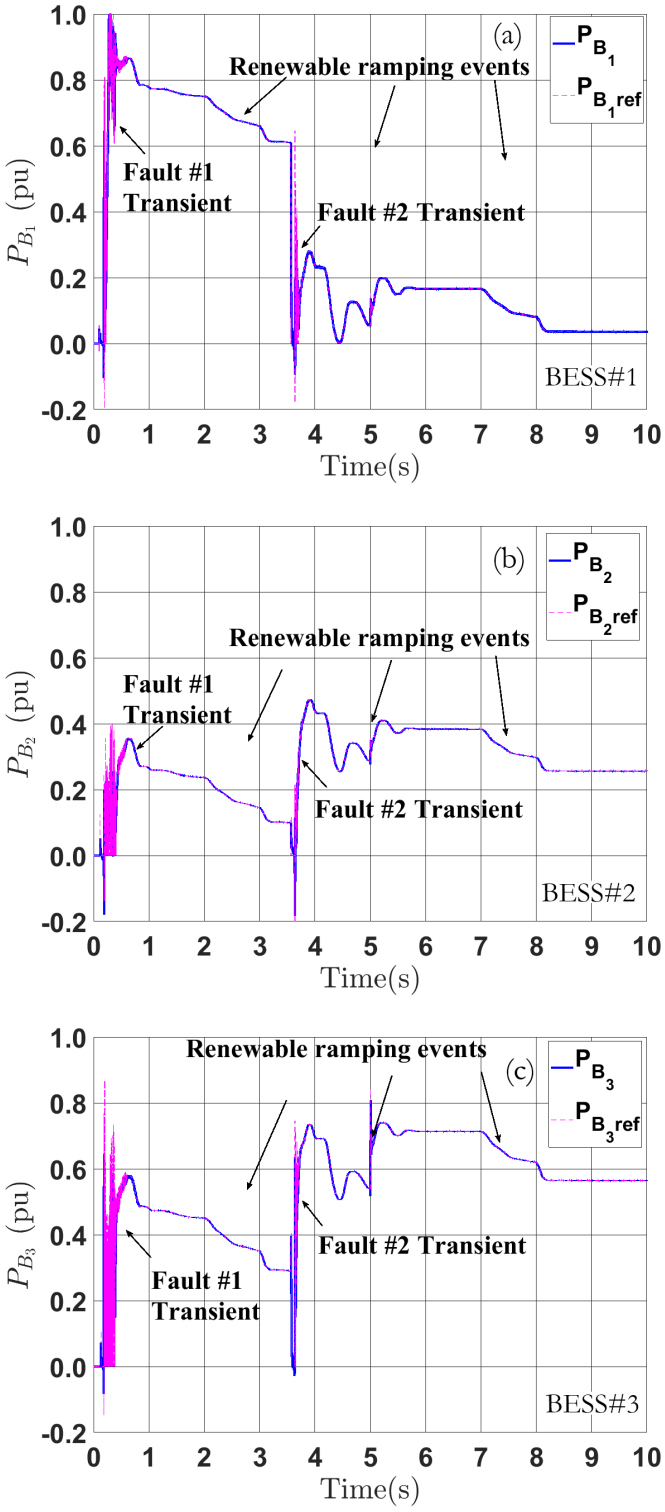

Figure 6.29: BESSs real power vs. time under multiple faults and renewable generation ramping events with adaptive voltage regulation (no regulation delay): (a) P_{B_1}; (b) P_{B_2}; (c) P_{B_3}

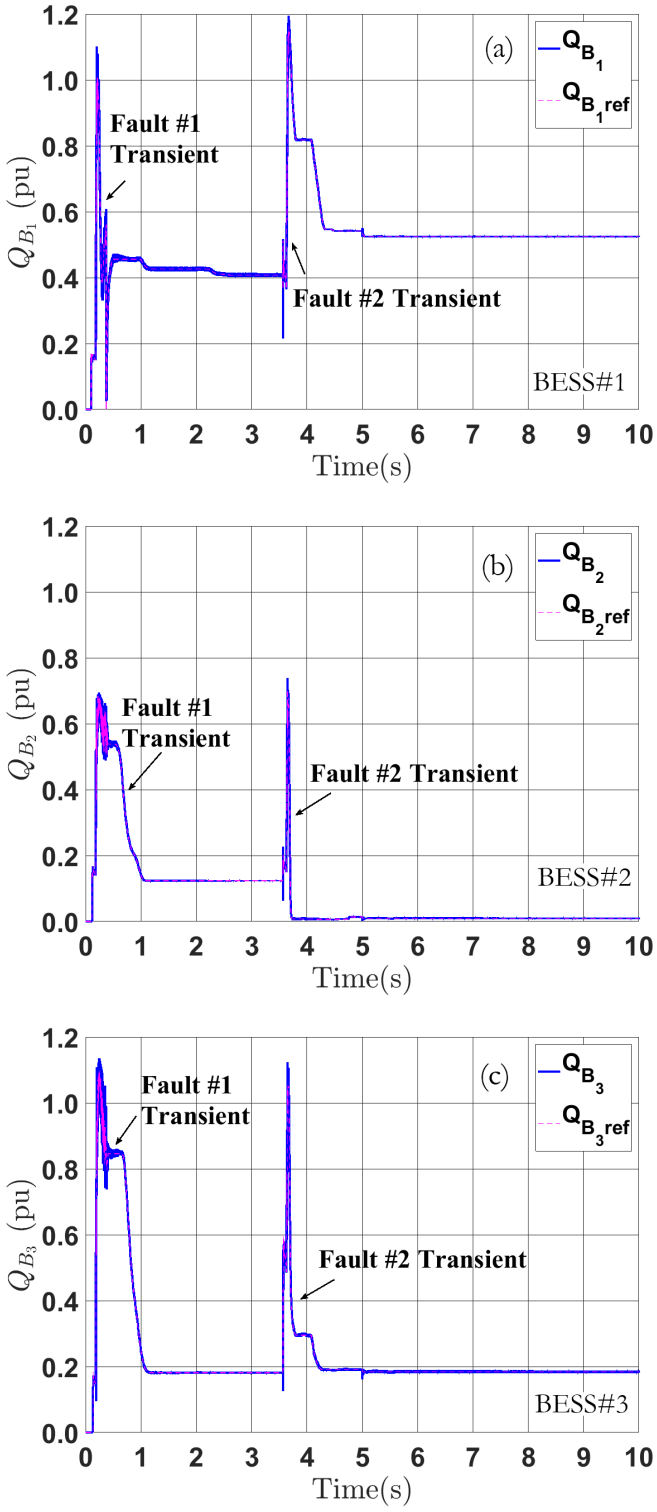

Figure 6.30: BESSs reactive power vs. time under multiple faults and renewable generation ramping events with adaptive voltage regulation (no regulation delay): (a) Q_{B_1}; (b) Q_{B_2}; (c) Q_{B_3}

6.3.2 Case#B: With voltage regulation control delay

The purpose of this case study is to show that it is beneficial to introduce appropriate control delays in the voltage regulation process. Such approach helps to avoid unnecessary voltage fluctuations and to achieve better microgrid frequency regulation. For this purpose, the BESSs' voltage regulators use the alternative decision tree as shown in Ch. 5.4.2, Fig. 5.7. In order to determine the $V_{ref}(t)$, this alternative algorithm introduces two voltage regulation delays. The adaptive voltage controller has the following settings: $V_{ref_N} = 1.00\ pu$, $V_{ref_E} = 1.25\ pu$, $V_{db} = 0.05\ pu$, $V_{th_L} = 0.50\ pu$, $V_{th_H} = V_{ref_E} - V_{db} = 1.20\ pu$, $K_R = 7\ V/s$, $t_{rs_1} = 0.100\ s$ (6 cycles), $t_{rs_2} = 0.067\ s$ (4 cycles), $t_{rs_3} = 1.000\ s$, $f_{sw} = 0.01\ pu$ (0.6 Hz), $t_{sw_1} = 0.083\ s$ (5 cycles), $t_{rd_1} = 0.100\ s$ **(6 cycles),** $t_{rd_2} = 0.017\ s$ **(1 cycles)** and $I_{sat} = 0.90\ I_{max}$. Figs. 6.31 to 6.34 highlight the results for this case study.

The PCC voltage profiles under this alternative adaptive voltage regulation strategy are shown in Fig. 6.31. The $V_{ref}(t)$ only ramps up after waiting for t_{rd_1} (6 cycles) under the low voltage condition. Since the first fault lasts 7 cycles, it triggers the adaptive voltage regulation actions. As the result, all three PCC voltages magnitudes have a higher post-fault/islanding value as indicated. This is beneficial for all IMs speed recover as shown in Fig. 6.32. Moreover, the $V_{ref}(t)$ does not immediately ramp down when $\hat{V}_{PCC}$ hits $V_{th_H} = 1.20\ pu$. Instead, it ramps down to V_{th_N} after waiting for t_{rd_2} (1 cycles). By doing so all BESSs can have time to regulate their $\hat{V}_{PCC}$ to the V_{th_E}. Meanwhile, it can achieve both higher probability for successful IMs speed recovery and a more uniformed voltage profiles across the microgrid.

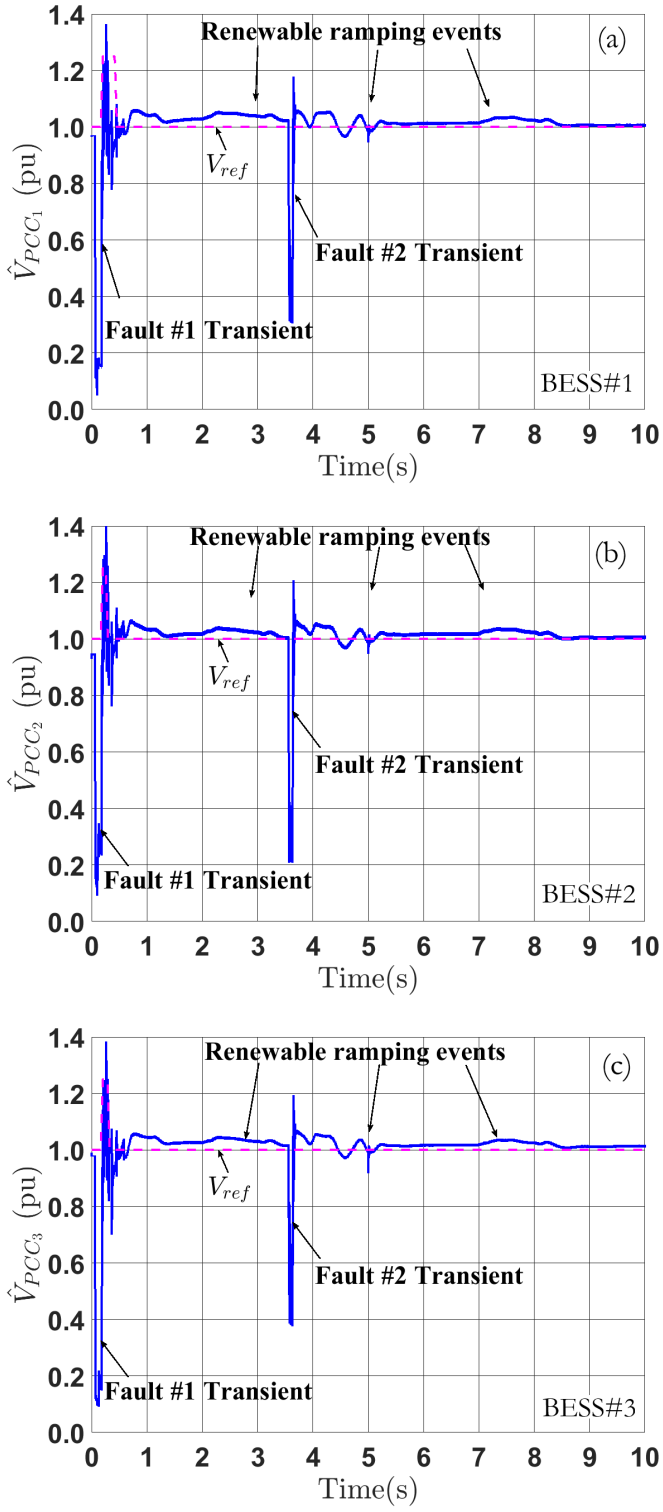

Figure 6.31: The PCCs voltage magnitude $\hat{V}_{PCC}$ vs. time under multiple faults and renewable generation ramping events with adaptive voltage regulation (including regulation delay): (a) $\hat{V}_{PCC_1}$; (b) $\hat{V}_{PCC_2}$; (c) $\hat{V}_{PCC_3}$

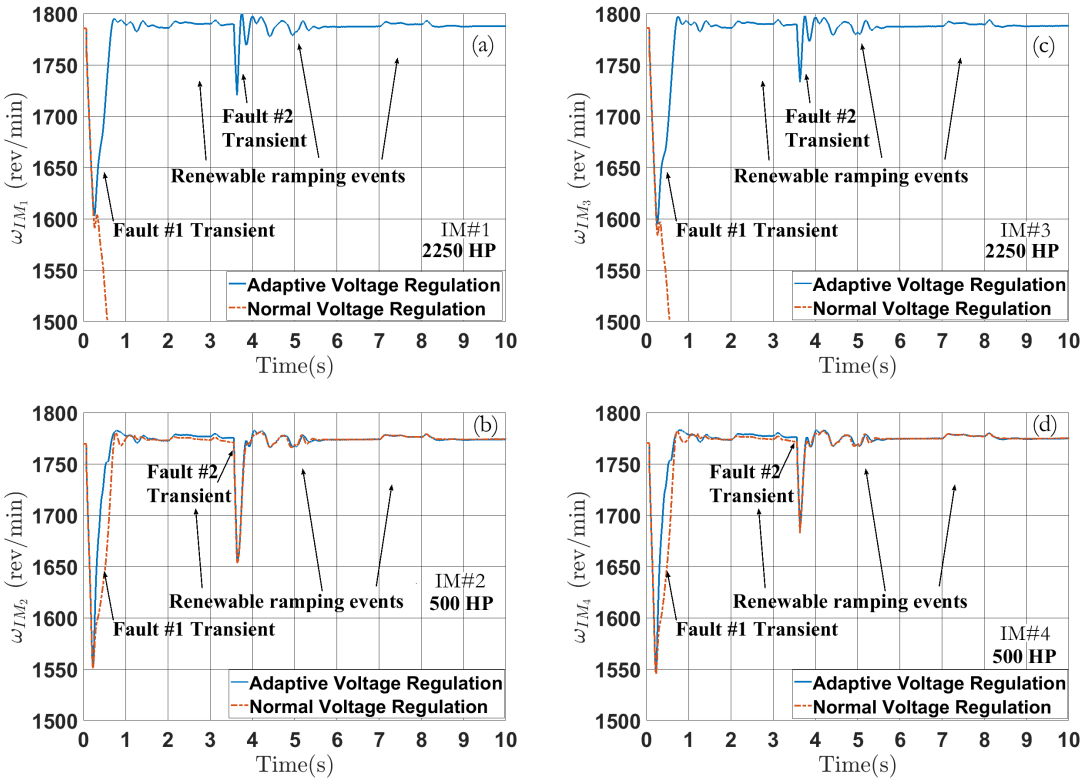

Figure 6.32: Induction motors speed ω_{IM} vs. time, under multiple faults and renewable generation ramping events with adaptive voltage regulation (including regulation delay): (a) ω_{IM_1}: 2250 HP; (b) ω_{IM_2}: 500 HP; (c) ω_{IM_3}: 2250 HP; (d) ω_{IM_4}: 500 HP

Since the true benefits of adaptive voltage regulation can only be shown under the cases with a prolonged fault clearing, it is unnecessary to ramp the $V_{ref}(t)$ up during a short fault disturbance. Therefore, the $V_{ref}(t)$ stays at V_{th_N} during the second fault event because it only takes 4 cycles to clear the fault. Nevertheless, all PCC's voltages quickly recover to their nominal values which contributes to a successful IMs fault ride-through. This setting also gives more converter capacity for a better microgrid frequency regulation, which is evident in Fig. 6.33. Comparing with generator rotor speeds in previous case #A, Fig. 6.23, $3 < t < 4\ s$, one can see that this new alternative achieves $1\ Hz$ less frequency excursions during the second fault for all three alternators. This additional accomplishment demonstrates the benefits of having appropriate control delays inside the adaptive voltage regulation algorithm. Finally, Fig. 6.34 details the magnified PCC voltage oscillograms during both faults. The adaptive voltage regulation contributes to a higher voltage magnitude shortly after clearing the fault #1. This higher voltage magnitude only lasts about 6 cycles and then quickly goes back to the nominal value. On the contrary, the voltage magnitude directly recovers to nominal value under fault #2. The quality of the voltage waveforms are excellent during both disturbances recovery.

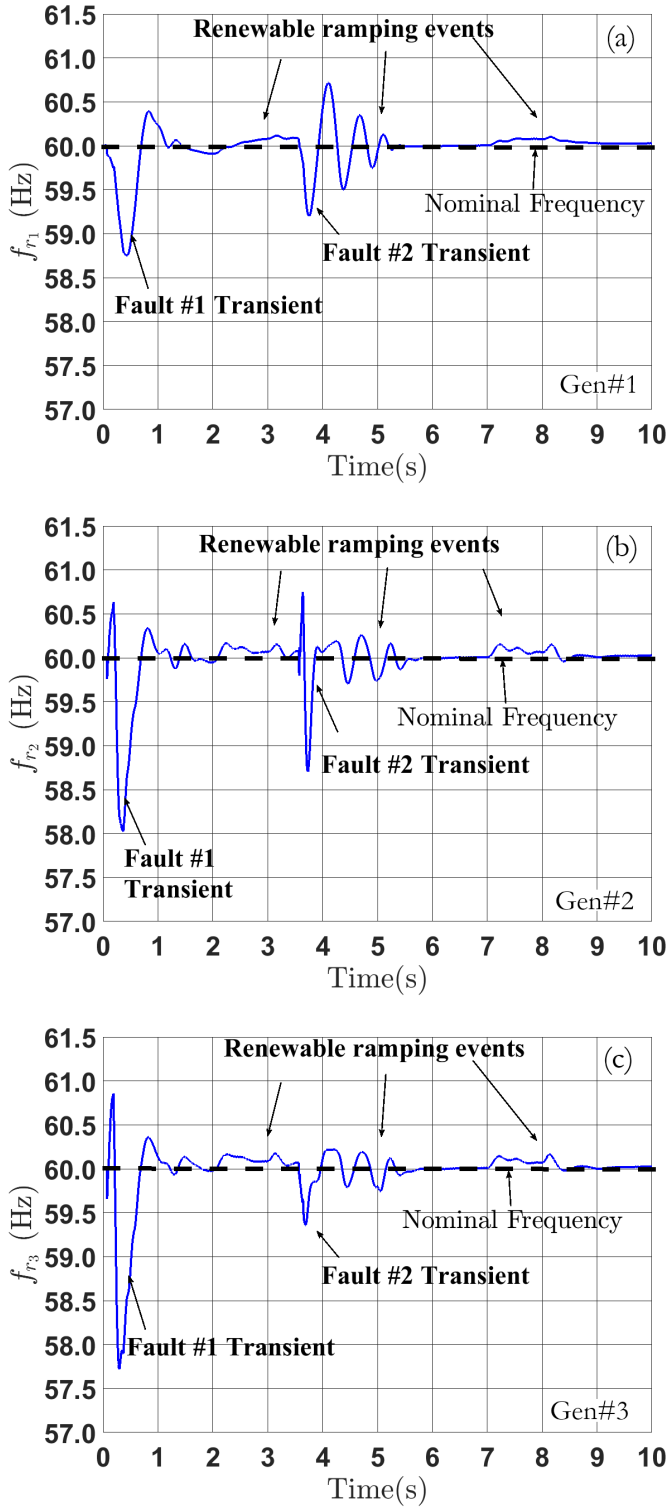

Figure 6.33: The synchronous generators rotor frequency f_r (Hz) vs. time under multiple faults and renewable generation ramping events with adaptive voltage regulation (including regulation delay): (a) f_{r_1}: 5 MVA hydroelectric generator; (b) f_{r_2}: 1.8 MVA diesel generator; (c) f_{r_3}: 3.125 MVA diesel generator

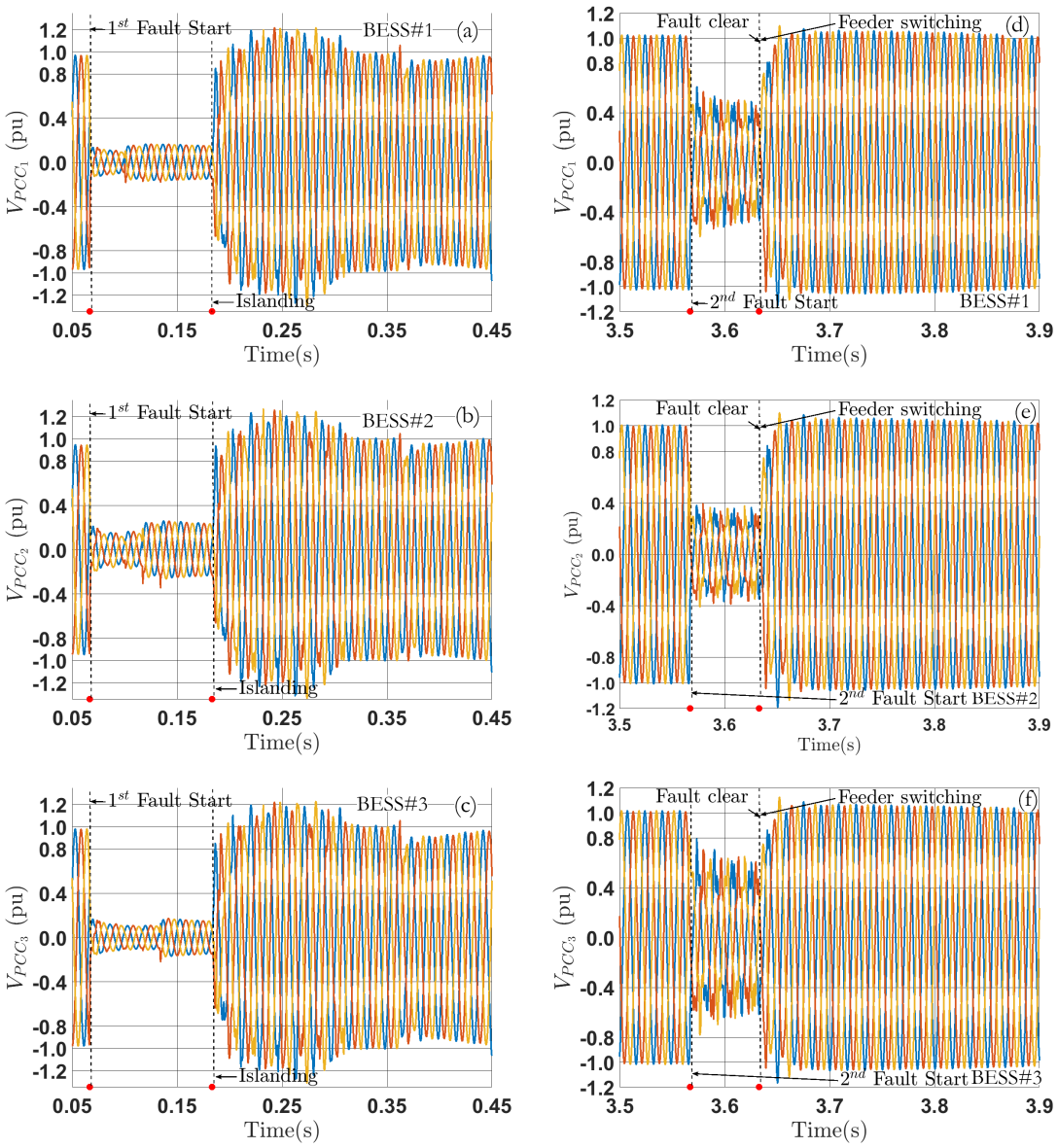

Figure 6.34: Magnified PCC voltage oscillogram vs. time under multiple faults and renewable generation ramping events with adaptive voltage regulation (including regulation delay): (a) V_{PCC_1}, first fault-induced islanding transient, $0.05 < t < 0.45$ s; (b) V_{PCC_2}, first fault-induced islanding transient, $0.05 < t < 0.45$ s; (c) V_{PCC_3}, first fault-induced islanding transient, $0.05 < t < 0.45$ s; (d) V_{PCC_1}, second (islanding) fault-induced feeder switching transient, $3.5 < t < 3.9$ s; (e) V_{PCC_2}, second (islanding) fault-induced feeder switching transient, $3.5 < t < 3.9$ s; (f) V_{PCC_3}, second (islanding) fault-induced feeder switching transient, $3.5 < t < 3.9$ s

6.4 Chapter6 Summary

This chapter presents extensive microgrid case studies under CIGRE MV distribution network with both synchronous generator and inverter based resources. They help to evaluate the effectiveness and robustness of proposed adaptive energy storage control methods under a meshed microgrid with topology change induced by feeder switching. The microgrid loadings are mixed with RLC impedance and IM loads. It has been shown that the microgrid stability and resiliency can be greatly enhanced under multiple disturbances with the help of the proposed BESSs' autonomous control actions. The transient events under investigation include fault-induced islanding (with both $symmetrical$ and $asymmetrical$ fault types), isolated microgrid internal fault, as well as, random power generating from renewable resources. The obtained results also demonstrate the advantages of both adaptive secondary frequency control and appropriate voltage regulation delays inside the adaptive voltage regulation algorithm.

Chapter 7

Conclusions

This dissertation research highlights the efficacy of flexibly utilizing the battery energy storage systems (BESSs) to enhance the stability of microgrids. This study introduces a set of autonomous adaptive control strategies for BESS converters to achieve fast microgrid frequency and voltage regulations. The following two sections summarize the main discoveries, contributions and suggest the future studies.

7.1 Summary

This work discovers the following aspects of adaptive energy storage system control:

- By adaptively changing the frequency controller gains based on the estimated Phase-Locked Loop (PLL) frequency deviation, the resulted nonlinear droop and secondary control can work together to achieve an enhanced microgrid frequency regulation with additional stability margins.
- By adaptively setting the voltage regulator reference point after sensing the low voltage condition, it enables the inductor motors to achieve a higher electromechanical torque for a successful fault-ride through.

- Although it is viable to help a heavily loaded induction motor ride-through a prolonged fault clearing time under the proposed adaptive voltage regulation with a large storage capacity, its economical feasibility needs further justifications.

- The real/reactive power/current allocations within the converter capacity limitation have significant impacts on the microgrid dynamic performances. It may be necessary to switch the converter power priority settings during real-time operations to meet the microgrid systems requirements, e.g., switching the priority from reactive power to real power when the microgrid experiences inadmissible frequency.

- The adaptive voltage regulation may not be necessary when the detected voltage sag durations are short. Therefore, some appropriate voltage regulation delays inside the adaptive voltage regulation settings can indeed be favorable.

- The proposed adaptive energy storage system control strategies are expandable under different microgrid configurations. They are also very robust under an unpredictable dynamic changing microgrid environment.

The dissertation has accomplished the following major contributions:

1. The study proposes a set of improved robust autonomous adaptive energy storage control strategies for both microgrid frequency and voltage regulation.

2. The study thoroughly investigates the proposed adaptive energy storage control strategies effects on microgrid stability and dynamic performances via extensive simulation case studies. The results verify the control efficacy, facilitate the microgrid design process and inspire the further methodology improvements.

7.2 Future Work

The following areas, in continuations of this study, can be worth exploring:

- This research has demonstrated the additional stability margins gained by adaptive nonlinear droop and secondary frequency control. The following technical concerns regarding the adaptive control demand additional painstaking investigations: (i): real-time adjustments for R_c based on locally available information for a better regulation performance, (ii): possibilities of other nonlinear control laws based on the PLL frequency measurement, e.g., the controller gains are resulted from nonlinear function of measured frequency deviation, and (iii): development of stability criterion for the proposed nonlinear frequency control law.

- This research has verified the effectiveness of proposed adaptive control for a short-term microgrid stability enhancement, it can expand to account the effects of a microrgrid controller with communication capabilities in order to study the coordinated control strategies among distributed generators and associated energy/power managements/optimizations over longer period of time.

- A future study may plan to tackle the optimization of the adaptive voltage regulation settings under different system standards, protection schemes and motor shaft load/torque-speed characteristics.

- The additional studies may take other un-modeled dynamics into consideration, such as the dynamics of converters DC sources or other types of nonlinear loads.

- The possible reconfigurations between multiple microgrids via multi-stages of islanding events or resynchronizations can be used to further examine the proposed control methodologies and study the aggregated impacts of microgrids on higher level grid dynamics.

Appendix A

System Parameters

A.1 Radial Feeder for Chapter 4 and 5

The studied microgrid in Ch. 4 and 5 are modeled using the following feeder data [114]. The Figs. 4.1 and 5.1 show the lengths of the feeder.

Positive-sequence impedance and susceptance:

$$Z_1 = 0.1906 + j0.3896\ \Omega/km,\ B_1 = 4.301\ \mu S/km$$

Zero-sequence impedance and susceptance:

$$Z_0 = 0.4806 + j1.2058\ \Omega/km,\ B_0 = 2.003\ \mu S/km$$

A.2 Microgrid data for Chapter 6 CIGRE Benchmark System

A.2.1 Feeder

The feeder line parameter for CIGRE benchmark system is shown below:

Positive-sequence impedance and susceptance:

$$Z_1 = 0.282 + j0.703\ \Omega/km,\ B_1 = 3.193\ \mu S/km$$

Zero-sequence impedance and susceptance:

$$Z_0 = 0.466 + j1.243\ \Omega/km,\ B_0 = 1.826\ \mu S/km$$

A.2.2 Transformer

The information below details the two transformers' parameters at CIGRE system HV-MV substation.

Transformer connects node 0 and 1: $Z = 0.104 + j1.24\ \Omega$ at 12.47 kV side;
$S_{rated} = 15\ MVA$.

Transformer connects node 0 and 12: $Z = 0.13 + j1.55\ \Omega$ at 12.47 kV side;
$S_{rated} = 12\ MVA$.

A.2.3 Loads

The Fig. A.1 below provides a table that summarizes the CIGRE system loading conditions implemented in Chapter 6 case studies.

The single-phase subnetwork has the loading of: 172.25 kVA with power factor of 0.94 inductive. In addition to the above table, there is a parasitic load (10% of their individual rated power) at each synchronous generator and IM terminal, Fig.6.1 (Bus #15: 0.5 MW; #16: 0.18 MW; #17: 0.3125 MW; #18: 0.168 MW; #19: 0.037 MW; #20: 0.168 MW; #21: 0.037 MW). The terminal capacitor bank values for IMs are: Bus #18: 0.6 Mvar; #19: 0.15 Mvar; #20: 0.6 Mvar; #21: 0.15 Mvar.

Node	Apparent Power, S [kVA]						Power Factor, pf	
	Phase A		Phase B		Phase C			
	Residential	Commercial or Industrial	Residential	Commercial or Industrial	Residential	Commercial or Industrial	Residential	Commercial or Industrial
1	1600	450	1600	280	1300	620	0.93	0.87
2	100 + Subnetwork	200	50	300	200	300	0.95	0.85
3	---	80	200	80	50	80	0.90	0.80
4	200	---	100	---	100	---	0.90	---
5	200	50	Subnetwork	200	---	50	0.95	0.85
6	50	---	100	---	Subnetwork	---	0.95	---
7	---	100	100	100	---	100	0.95	0.95
8	100	---	150	---	---	200	0.90	0.90
9	100	---	150	---	100	---	0.95	---
10	150	---	100	---	250	---	0.90	---
11	50	---	50	---	---	---	0.95	0.85
12	700	250	700	250	700	250	0.90	0.87
13	Subnetwork	75	Subnetwork	75	---	75	0.95	0.85
14	---	90	---	90	Subnetwork	90	0.90	0.90

Figure A.1: CIGRE system loading

A.3 Synchronous generators

The synchronous machines' parameters can be found in the following table [1, 125]:

Generator number	1	2	3
Power rating (MVA)	5	1.8	3.125
Voltage rating(KV)	13.8	2.4	2.4
X_d (pu)	2.86	2.38	1.56
X_q (pu)	2.0	1.1	1.06
$X_d^{'}$ (pu)	0.7	0.264	0.296
$X_d^{''}$ (pu)	0.22	0.201	0.177
$X_q^{''}$ (pu)	0.21	0.376	0.177
X_l (pu)	0.2	0.2	0.088
$T_{d0}^{'}$ (pu)	3.4	2.47	3.7
$T_{d0}^{''}$ (pu)	0.01	0.018	0.05
$T_{q0}^{''}$ (pu)	0.05	0.009	0.05
H (s)	2.9	1.035	1.0716

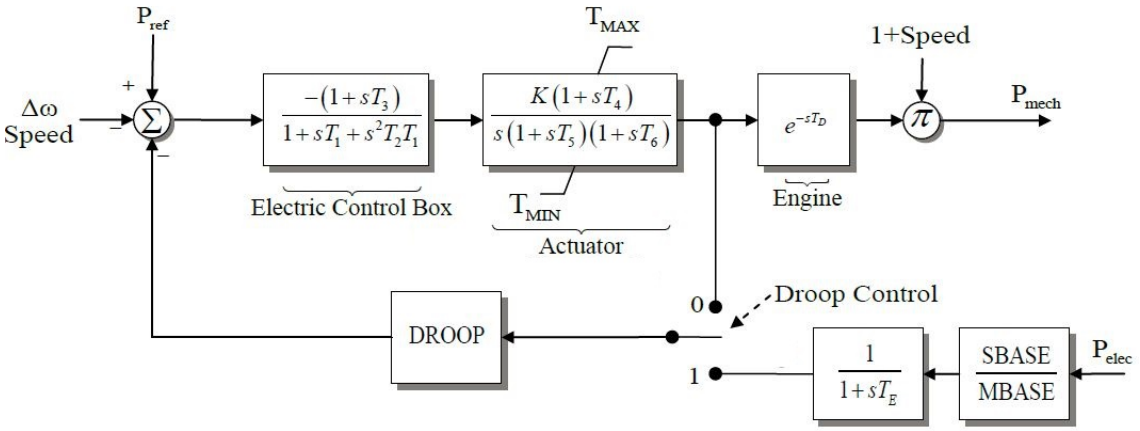

Figure A.2: Diesel governor block diagram

A.4 Prime movers and governing systems

This appendix describes the two types of synchronous generator's prime movers used in this research work: diesel engine and hydraulic turbine with their governing system.

A Woodward diesel engine control system shown in Fig. A.2 is used in the study [125, 137] and its block diagram is shown below:

The information below summarized the parameters used in this diesel governor model:

$K = 40$; $T_1 = 0.01\ s$; $T_2 = 0.02\ s$; $T_3 = 0.2\ s$; $T_4 = 0.25\ s$; $T_5 = 0.009\ s$; $T_6 = 0.0384\ s$; $T_D = 0.024\ s$; $T_{MIN} = 0$; $T_{MAX} = 1.1$.

Similarly, the hydraulic turbine and governing system MATLAB block diagram is shown in the following Fig. A.3 [119].

The following parameters are used in this study:

Servo-motor: $K_a = \frac{10}{3}$; $T_a = 0.07\ s$, Position ranging (pu): [0.01, 0.97518], speed limits range (pu/s): [-0.1, 0.1].

Droop setting and main PID regulator: 5 % droop, PID settings: $K_P = 1.163$; $K_I = 0.105$; $K_D = 0$; Time constant for derivative (s): 0.01.

Hydraulic turbine: beta=0; turbine gain=1.0361; $t_w = 2.67\ s$.

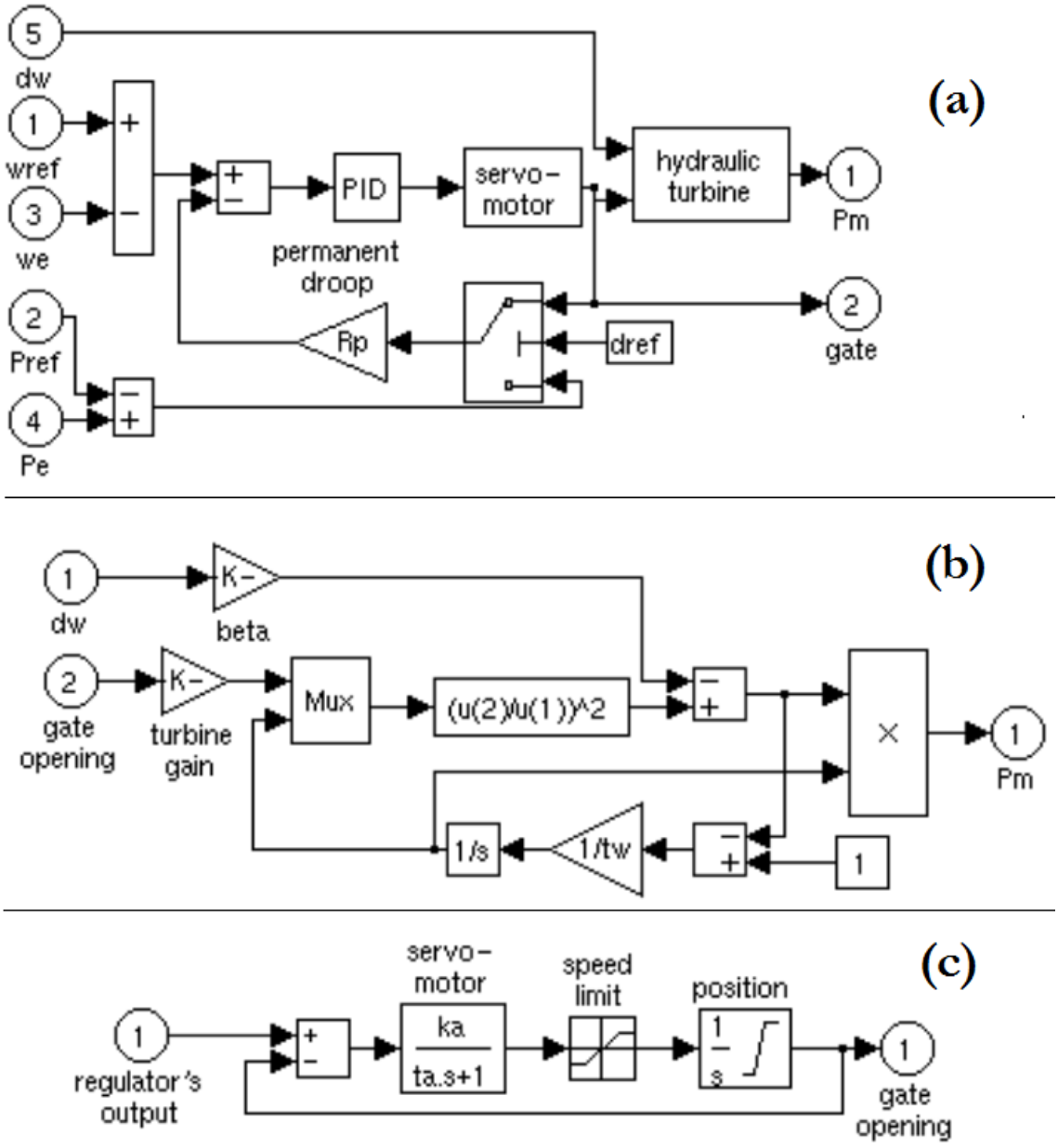

Figure A.3: MATLAB hydraulic turbine and governing system block diagram: (a). Overall model; (b). hydraulic turbine; (c). gate servomotor

A.5 Excitation systems

The excitation systems parameters used in this study according to Fig. 3.6 are summarized as below:

DC excitation system for hydro generator:

$K_A = 300$; $\tau_A = 0.001\ s$; $K_E = 1$; $\tau_E = 0\ s$; $V_{R_{max}} = 11.5$;

AC excitation system for diesel generator:

$K_A = 400$; $\tau_A = 0.02\ s$; $K_E = 1$; $\tau_E = 0.8\ s$; $K_D = 0.38$; $V_{R_{max}} = 14.5$; Exciter saturation function pairs: [$V_{E_1} = 4.18$, $S_E(V_{E_1}) = 0.1$], [$V_{E_2} = 3.14$, $S_E(V_{E_2}) = 0.03$].

A.6 Inverter

The data for a $2.5\ MVA$ converter used in Ch. 5 is presented below. The values can be scaled according to [48] for different sizes of inverter.

Interface impedance to PCC (refer to the $13.8\ kV$ side) [127]:

$Z = 0.3809 + j3.8090\ \Omega$

Current controller [49]:

$K_p = 0.5305$, $K_i = 20$

Phase-Locked Loop (PLL)

Figure A.4 shows the schematic diagram for the PLL and associated control block diagram. It utilizes the feedback control to realize voltage phasor $abc-$ to $dq-$ transformation phase shift ρ such that $\omega t - \rho = 0$ ($V_q = 0$). The integrator in the Fig. A.4(a) refers

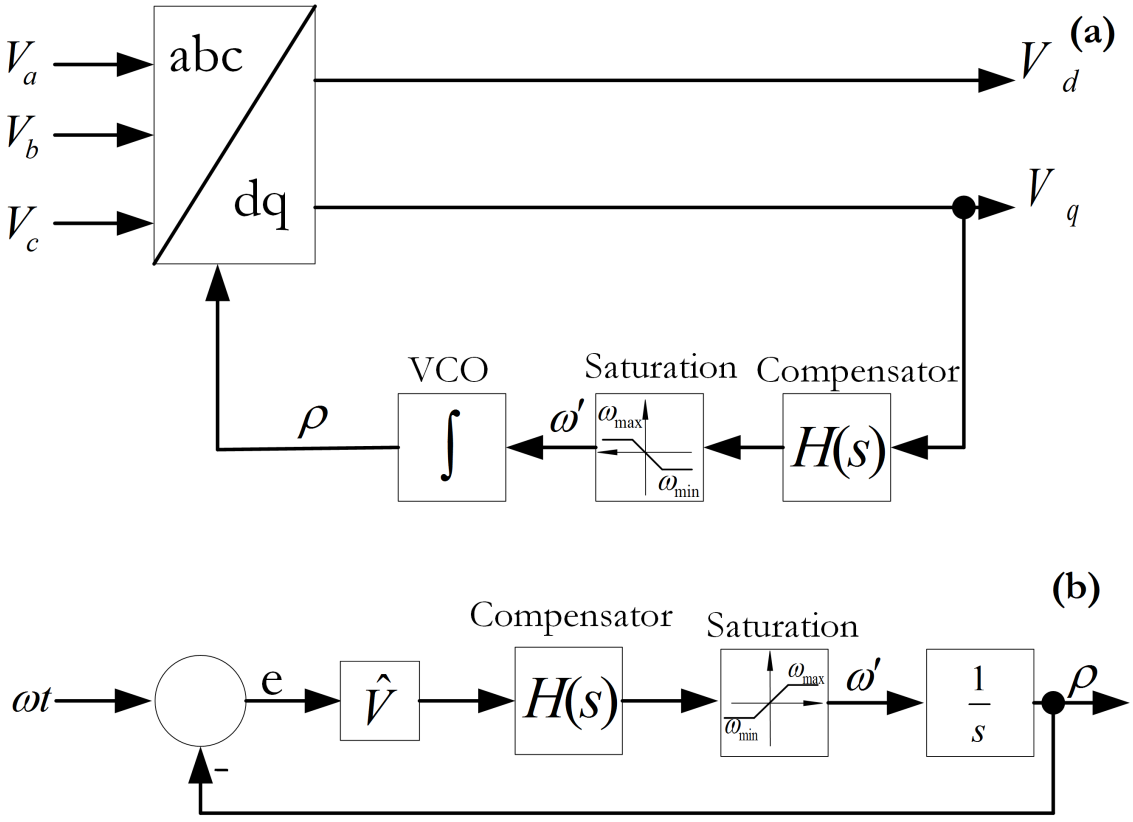

Figure A.4: PLL schematic and associated control block diagram

as voltage-controlled oscillator (VCO). It resets the ρ to zero whenever it reaches 2π. The control block diagram is based on the following PLL control law:

$$\begin{aligned} \frac{d\rho}{dt} &= \omega'(t) = H(p)\hat{V}(\omega t - \rho) \\ \omega'(0) = \omega_s \quad and \quad \omega_{min} &\leq \omega'(t) \leq \omega_{max} \end{aligned} \tag{A.1}$$

The $p = d(\bullet)/dt$ is the differentiation operator, ω_s is the nominal power system angular frequency. The initial condition and range constrain of $\omega'(t)$ ensure a satisfactory behavior of the PLL [49]. In this study, the $\omega_{min} = 345.6\, rad/s$ and $\omega_{max} = 471.2\, rad/s$.

With per-unitization, the following values are chosen for the PLL compensator $H(s)$

based on the method proposed in [49]:

$$H(s) = \frac{2.68 \times 10^5 (s^2 + 568,516)(s^2 + 166s + 6889)}{s^2(s^2 + 1508s + 568,516)(s^2 + 964s + 232,324)} \; [(rad/s)/V] \qquad \text{(A.2)}$$

A.7 Induction Motors

The following table summarizes the induction motor loads information used in this thesis [117].

Motor number	1	2
Power rating (HP)	2250	500
Voltage rating(KV)	2.3	2.3
Stator R_S (Ω)	0.029	0.262
Stator/Rotor inductance $L_S = L_r\prime$ (μH)	600	3200
Rotor $R_r\prime$ (Ω)	0.022	0.187
Mutual inductance L_m (mH)	34.6	143.3
Base inertia J'_{IM} ($Kg.m^2$)	63.87	11.06
Damping Coefficient D ($N.m.s$)	1.607	0.402

Bibliography

[1] F. Katiraei, *Dynamic analysis and control of distributed energy resources in a micro-grid*. Ph.D. dissertation, U. Toronto, Canada, 2005.

[2] H. You, V. Vittal, and X. Wang, "Slow coherency-based islanding," *IEEE Transactions on Power Systems*, vol. 19, pp. 483–491, Feb 2004.

[3] G. Andersson, P. Donalek, R. Farmer, N. Hatziargyriou, I. Kamwa, P. Kundur, N. Martins, J. Paserba, P. Pourbeik, J. Sanchez-Gasca, R. Schulz, A. Stankovic, C. Taylor, and V. Vittal, "Causes of the 2003 major grid blackouts in north america and europe, and recommended means to improve system dynamic performance," *IEEE Transactions on Power Systems*, vol. 20, pp. 1922–1928, Nov 2005.

[4] R. H. Lasseter, "Smart distribution: Coupled microgrids," *Proceedings of the IEEE*, vol. 99, pp. 1074–1082, June 2011.

[5] "IEEE draft standard for interconnection and interoperability of distributed energy resources with associated electric power systems interfaces," *IEEE P1547/D7.0, September 2017*, pp. 1–147, Jan 2017.

[6] J. A. P. Lopes, C. L. Moreira, and A. G. Madureira, "Defining control strategies for microgrids islanded operation," *IEEE Transactions on Power Systems*, vol. 21, pp. 916–924, May 2006.

[7] A. H. K. Alaboudy, H. H. Zeineldin, and J. Kirtley, "Microgrid stability characterization subsequent to fault-triggered islanding incidents," *IEEE Transactions on Power Delivery*, vol. 27, pp. 658–669, April 2012.

[8] A. A. Akhil etc, *DOE/EPRI Electricity Storage Handbook in Collaboration with NRECA*. SAND2015-1002, Sandia National Laboratories.

[9] Y. A. R. I. Mohamed and E. F. El-Saadany, "Adaptive decentralized droop controller to preserve power sharing stability of paralleled inverters in distributed generation microgrids," *IEEE Transactions on Power Electronics*, vol. 23, pp. 2806–2816, Nov 2008.

[10] J. C. Vasquez, J. M. Guerrero, A. Luna, P. Rodriguez, and R. Teodorescu, "Adaptive droop control applied to voltage-source inverters operating in grid-connected and islanded modes," *IEEE Transactions on Industrial Electronics*, vol. 56, pp. 4088–4096, Oct 2009.

[11] G. Diaz, C. Gonzalez-Moran, J. Gomez-Aleixandre, and A. Diez, "Scheduling of droop coefficients for frequency and voltage regulation in isolated microgrids," *IEEE Transactions on Power Systems*, vol. 25, pp. 489–496, Feb 2010.

[12] J. Kim, J. M. Guerrero, P. Rodriguez, R. Teodorescu, and K. Nam, "Mode adaptive droop control with virtual output impedances for an inverter-based flexible ac microgrid," *IEEE Transactions on Power Electronics*, vol. 26, pp. 689–701, March 2011.

[13] Y. Sun, W. Huang, G. Wang, W. Wang, D. Wang, and L. Zhang, "Study of control strategy of dg based on nonlinear droop characteristic," in *2012 China International Conference on Electricity Distribution*, pp. 1–4, Sept 2012.

[14] "Benchmark Systems for Network Integration of Renewable and Distributed Energy Resources, CIGRE WG (TF): WG C6.04," April 2014.

[15] P. Kundur, N. Balu, and M. Lauby, *Power System Stability and Control*. EPRI power system engineering series, McGraw-Hill, 1994.

[16] G. Masters, *Renewable and Efficient Electric Power Systems*. Wiley - IEEE, Wiley, 2013.

[17] S. Blumsack, "How the free market rocked the grid," *IEEE Spectrum*, vol. 47, pp. 44–59, December 2010.

[18] E. Santacana, G. Rackliffe, L. Tang, and X. Feng, "Getting smart," *IEEE Power and Energy Magazine*, vol. 8, pp. 41–48, March 2010.

[19] T. Zhang, *The Economic Benefits of Battery Energy Storage System in Electric Distribution System*. MS Thesis, Worcester Polytechnic Institute (WPI), USA, 2013.

[20] M. Smith and D. Ton, "Key connections: The u.s. department of energy?s microgrid initiative," *IEEE Power and Energy Magazine*, vol. 11, pp. 22–27, July 2013.

[21] P. F. Ribeiro, B. K. Johnson, M. L. Crow, A. Arsoy, and Y. Liu, "Energy storage systems for advanced power applications," *Proceedings of the IEEE*, vol. 89, pp. 1744–1756, Dec 2001.

[22] M. Farhadi and O. Mohammed, "Energy storage technologies for high-power applications," *IEEE Transactions on Industry Applications*, vol. 52, pp. 1953–1961, May 2016.

[23] K. D. Bachovchin, *Design, Modeling, and Power Electronic Control for Transient Stabilization of Power Grids Using Flywheel Energy Storage Systems*. Ph.D. dissertation, Carnegie Mellon University (CMU), PA, 2015.

[24] A. Kanchanaharuthai, V. Chankong, and K. A. Loparo, "Transient stability and voltage regulation in multimachine power systems vis statcom and battery energy storage," *IEEE Transactions on Power Systems*, vol. 30, pp. 2404–2416, Sept 2015.

[25] A. Oudalov, D. Chartouni, and C. Ohler, "Optimizing a battery energy storage system for primary frequency control," *IEEE Transactions on Power Systems*, vol. 22, pp. 1259–1266, Aug 2007.

[26] O. Leitermann, *Energy storage for frequency regulation on the electric grid*. Ph.D. dissertation, Massachusetts Institute of Technology (MIT), MA, 2015.

[27] I. Serban, R. Teodorescu, and C. Marinescu, "Energy storage systems impact on the short-term frequency stability of distributed autonomous microgrids, an analysis using aggregate models," *IET Renewable Power Generation*, vol. 7, pp. 531–539, Sept 2013.

[28] I. Serban and C. Marinescu, "Control strategy of three-phase battery energy storage systems for frequency support in microgrids and with uninterrupted supply of local loads," *IEEE Transactions on Power Electronics*, vol. 29, pp. 5010–5020, Sept 2014.

[29] E. Liegmann and R. Majumder, "An efficient method of multiple storage control in microgrids," *IEEE Transactions on Power Systems*, vol. 30, pp. 3437–3444, Nov 2015.

[30] A. S. Khalsa and S. Baktiono, "Certs microgrid test bed battery energy storage system report: Phase 1," tech. rep., 10/2016 2016.

[31] G. Delille, B. Francois, and G. Malarange, "Dynamic frequency control support by energy storage to reduce the impact of wind and solar generation on isolated power system's inertia," *IEEE Transactions on Sustainable Energy*, vol. 3, pp. 931–939, Oct 2012.

[32] F. Blaabjerg, Z. Chen, and S. B. Kjaer, "Power electronics as efficient interface in dispersed power generation systems," *IEEE Transactions on Power Electronics*, vol. 19, pp. 1184–1194, Sept 2004.

[33] J. M. Carrasco, L. G. Franquelo, J. T. Bialasiewicz, E. Galvan, R. C. PortilloGuisado, M. A. M. Prats, J. I. Leon, and N. Moreno-Alfonso, "Power-electronic systems for the grid integration of renewable energy sources: A survey," *IEEE Transactions on Industrial Electronics*, vol. 53, pp. 1002–1016, June 2006.

[34] D. Boroyevich, I. Cvetkovi, D. Dong, R. Burgos, F. Wang, and F. Lee, "Future electronic power distribution systems a contemplative view," in *2010 12th International Conference on Optimization of Electrical and Electronic Equipment*, pp. 1369–1380, May 2010.

[35] J. D. van Wyk and F. C. Lee, "On a future for power electronics," *IEEE Journal of Emerging and Selected Topics in Power Electronics*, vol. 1, pp. 59–72, June 2013.

[36] A. Tabesh and R. Iravani, "Multivariable dynamic model and robust control of a voltage-source converter for power system applications," *IEEE Transactions on Power Delivery*, vol. 24, pp. 462–471, Jan 2009.

[37] C. Schauder and H. Mehta, "Vector analysis and control of advanced static var compensators," *IEE Proceedings C - Generation, Transmission and Distribution*, vol. 140, pp. 299–306, July 1993.

[38] A. Timbus, M. Liserre, R. Teodorescu, and F. Blaabjerg, "Synchronization methods for three phase distributed power generation systems - an overview and evaluation," in *2005 IEEE 36th Power Electronics Specialists Conference*, pp. 2474–2481, June 2005.

[39] F. Blaabjerg, R. Teodorescu, M. Liserre, and A. V. Timbus, "Overview of control and grid synchronization for distributed power generation systems," *IEEE Transactions on Industrial Electronics*, vol. 53, pp. 1398–1409, Oct 2006.

[40] S.-K. Chung, "A phase tracking system for three phase utility interface inverters," *IEEE Transactions on Power Electronics*, vol. 15, pp. 431–438, May 2000.

[41] D. Jovcic, "Phase locked loop system for facts," *IEEE Transactions on Power Systems*, vol. 18, pp. 1116–1124, Aug 2003.

[42] P. Rodrguez, R. Teodorescu, I. Candela, A. V. Timbus, M. Liserre, and F. Blaabjerg, "New positive-sequence voltage detector for grid synchronization of power converters under faulty grid conditions," in *2006 37th IEEE Power Electronics Specialists Conference*, pp. 1–7, June 2006.

[43] P. Rodriguez, A. Luna, I. Candela, R. Mujal, R. Teodorescu, and F. Blaabjerg, "Multiresonant frequency-locked loop for grid synchronization of power converters under distorted grid conditions," *IEEE Transactions on Industrial Electronics*, vol. 58, pp. 127–138, Jan 2011.

[44] B. B. Johnson, S. V. Dhople, A. O. Hamadeh, and P. T. Krein, "Synchronization of parallel single-phase inverters with virtual oscillator control," *IEEE Transactions on Power Electronics*, vol. 29, pp. 6124–6138, Nov 2014.

[45] H. P. Beck and R. Hesse, "Virtual synchronous machine," in *2007 9th International Conference on Electrical Power Quality and Utilisation*, pp. 1–6, Oct 2007.

[46] Q. C. Zhong, "Virtual synchronous machines: A unified interface for grid integration," *IEEE Power Electronics Magazine*, vol. 3, pp. 18–27, Dec 2016.

[47] M. Liserre, F. Blaabjerg, and S. Hansen, "Design and control of an lcl-filter-based three-phase active rectifier," *IEEE Transactions on Industry Applications*, vol. 41, pp. 1281–1291, Sept 2005.

[48] V. Purba, S. V. Dhople, S. Jafarpour, F. Bullo, and B. B. Johnson, "Reduced-order structure-preserving model for parallel-connected three-phase grid-tied inverters," in *2017 IEEE 18th Workshop on Control and Modeling for Power Electronics (COMPEL)*, pp. 1–7, July 2017.

[49] A. Yazdani and R. Iravani, *Voltage-Sourced Converters in Power Systems: Modeling, Control, and Applications*. Wiley, 2010.

[50] J. M. Guerrero, L. Hang, and J. Uceda, "Control of distributed uninterruptible power supply systems," *IEEE Transactions on Industrial Electronics*, vol. 55, pp. 2845–2859, Aug 2008.

[51] M. C. Chandorkar, D. M. Divan, and R. Adapa, "Control of parallel connected inverters in standalone ac supply systems," *IEEE Transactions on Industry Applications*, vol. 29, pp. 136–143, Jan 1993.

[52] K. D. Brabandere, B. Bolsens, J. V. den Keybus, A. Woyte, J. Driesen, and R. Belmans, "A voltage and frequency droop control method for parallel inverters," *IEEE Transactions on Power Electronics*, vol. 22, pp. 1107–1115, July 2007.

[53] A. Tuladhar, H. Jin, T. Unger, and K. Mauch, "Control of parallel inverters in distributed ac power systems with consideration of line impedance effect," *IEEE Transactions on Industry Applications*, vol. 36, pp. 131–138, Jan 2000.

[54] J. W. Simpson-Porco, F. Drfler, and F. Bullo, "Synchronization and power sharing for droop-controlled inverters in islanded microgrids," *Automatica*, vol. 49, no. 9, pp. 2603 – 2611, 2013.

[55] J. M. Guerrero, L. G. de Vicuna, J. Matas, M. Castilla, and J. Miret, "Output impedance design of parallel-connected ups inverters with wireless load-sharing control," *IEEE Transactions on Industrial Electronics*, vol. 52, pp. 1126–1135, Aug 2005.

[56] J. M. Guerrero, J. Matas, L. G. de Vicuna, M. Castilla, and J. Miret, "Decentralized control for parallel operation of distributed generation inverters using resistive output impedance," *IEEE Transactions on Industrial Electronics*, vol. 54, pp. 994–1004, April 2007.

[57] N. R. Chaudhuri and B. Chaudhuri, "Adaptive droop control for effective power sharing in multi-terminal dc (mtdc) grids," *IEEE Transactions on Power Systems*, vol. 28, pp. 21–29, Feb 2013.

[58] J. Yu, *Hybrid AC-High Voltage DC Grid Stability and Controls*. Ph.D. dissertation, Arizona State University (ASU), AZ, Nov. 2017.

[59] P. Rodriguez, A. V. Timbus, R. Teodorescu, M. Liserre, and F. Blaabjerg, "Flexible active power control of distributed power generation systems during grid faults," *IEEE Transactions on Industrial Electronics*, vol. 54, pp. 2583–2592, Oct 2007.

[60] A. Camacho, M. Castilla, J. Miret, R. Guzman, and A. Borrell, "Reactive power control for distributed generation power plants to comply with voltage limits during grid faults," *IEEE Transactions on Power Electronics*, vol. 29, pp. 6224–6234, Nov 2014.

[61] J. Rocabert, A. Luna, F. Blaabjerg, and P. Rodrguez, "Control of power converters in ac microgrids," *IEEE Transactions on Power Electronics*, vol. 27, pp. 4734–4749, Nov 2012.

[62] S. Barsali, M. Ceraolo, P. Pelacchi, and D. Poli, "Control techniques of dispersed generators to improve the continuity of electricity supply," in *2002 IEEE Power Engineering Society Winter Meeting. Conference Proceedings (Cat. No.02CH37309)*, vol. 2, pp. 789–794 vol.2, 2002.

[63] A. Yazdani and P. P. Dash, "A control methodology and characterization of dynamics for a photovoltaic (pv) system interfaced with a distribution network," *IEEE Transactions on Power Delivery*, vol. 24, pp. 1538–1551, July 2009.

[64] Y. Li, D. M. Vilathgamuwa, and P. C. Loh, "Microgrid power quality enhancement using a three-phase four-wire grid-interfacing compensator," *IEEE Transactions on Industry Applications*, vol. 41, pp. 1707–1719, Nov 2005.

[65] M. Prodanovic and T. C. Green, "High-quality power generation through distributed control of a power park microgrid," *IEEE Transactions on Industrial Electronics*, vol. 53, pp. 1471–1482, Oct 2006.

[66] M. B. Delghavi and A. Yazdani, "A control strategy for islanded operation of a distributed resource (dr) unit," in *2009 IEEE Power Energy Society General Meeting*, pp. 1–8, July 2009.

[67] M. B. Delghavi and A. Yazdani, "A unified control strategy for electronically interfaced distributed energy resources," *IEEE Transactions on Power Delivery*, vol. 27, pp. 803–812, April 2012.

[68] J. He, Y. W. Li, D. Bosnjak, and B. Harris, "Investigation and active damping of multiple resonances in a parallel-inverter-based microgrid," *IEEE Transactions on Power Electronics*, vol. 28, pp. 234–246, Jan 2013.

[69] R. Lasseter and P. Piagi, "Providing premium power through distributed resources," in *Proceedings of the 33rd Annual Hawaii International Conference on System Sciences*, pp. 9 pp.–, Jan 2000.

[70] R. H. Lasseter and P. Paigi, "Microgrid: a conceptual solution," in *2004 IEEE 35th Annual Power Electronics Specialists Conference (IEEE Cat. No.04CH37551)*, vol. 6, pp. 4285–4290 Vol.6, June 2004.

[71] P. Piagi and R. H. Lasseter, "Autonomous control of microgrids," in *2006 IEEE Power Engineering Society General Meeting*, pp. 8 pp.–, 2006.

[72] A. A. Renjit, M. S. Illindala, R. H. Lasseter, M. J. Erickson, and D. Klapp, "Modeling and control of a natural gas generator set in the certs microgrid," in *2013 IEEE Energy Conversion Congress and Exposition*, pp. 1640–1646, Sept 2013.

[73] E. Alegria, T. Brown, E. Minear, and R. H. Lasseter, "Certs microgrid demonstration with large-scale energy storage and renewable generation," *IEEE Transactions on Smart Grid*, vol. 5, pp. 937–943, March 2014.

[74] F. Katiraei, M. R. Iravani, and P. W. Lehn, "Micro-grid autonomous operation during and subsequent to islanding process," *IEEE Transactions on Power Delivery*, vol. 20, pp. 248–257, Jan 2005.

[75] F. Katiraei and M. R. Iravani, "Power management strategies for a microgrid with multiple distributed generation units," *IEEE Transactions on Power Systems*, vol. 21, pp. 1821–1831, Nov 2006.

[76] F. Katiraei, R. Iravani, N. Hatziargyriou, and A. Dimeas, "Microgrids management," *IEEE Power and Energy Magazine*, vol. 6, pp. 54–65, May 2008.

[77] C. K. Sao and P. W. Lehn, "Control and power management of converter fed microgrids," *IEEE Transactions on Power Systems*, vol. 23, pp. 1088–1098, Aug 2008.

[78] S. M. Ashabani and Y. A. R. I. Mohamed, "General interface for power management of micro-grids using nonlinear cooperative droop control," *IEEE Transactions on Power Systems*, vol. 28, pp. 2929–2941, Aug 2013.

[79] H. H. Zeineldin and J. L. Kirtley, "Micro-grid operation of inverter based distributed generation with voltage and frequency dependent loads," in *2009 IEEE Power Energy Society General Meeting*, pp. 1–6, July 2009.

[80] Q. Shafiee, J. M. Guerrero, and J. C. Vasquez, "Distributed secondary control for islanded microgrids; a novel approach," *IEEE Transactions on Power Electronics*, vol. 29, pp. 1018–1031, Feb 2014.

[81] F. Guo, C. Wen, J. Mao, and Y. D. Song, "Distributed secondary voltage and frequency restoration control of droop-controlled inverter-based microgrids," *IEEE Transactions on Industrial Electronics*, vol. 62, pp. 4355–4364, July 2015.

[82] Y. Zhang and B. T. Ooi, "Stand-alone doubly-fed induction generators (dfigs) with autonomous frequency control," *IEEE Transactions on Power Delivery*, vol. 28, pp. 752–760, April 2013.

[83] J. M. Guerrero, J. C. Vasquez, J. Matas, L. G. de Vicuna, and M. Castilla, "Hierarchical control of droop-controlled ac and dc microgrids; a general approach toward standardization," *IEEE Transactions on Industrial Electronics*, vol. 58, pp. 158–172, Jan 2011.

[84] A. Bidram and A. Davoudi, "Hierarchical structure of microgrids control system," *IEEE Transactions on Smart Grid*, vol. 3, pp. 1963–1976, Dec 2012.

[85] D. E. Olivares, A. Mehrizi-Sani, A. H. Etemadi, C. A. Caizares, R. Iravani, M. Kazerani, A. H. Hajimiragha, O. Gomis-Bellmunt, M. Saeedifard, R. Palma-Behnke, G. A. Jimnez-Estvez, and N. D. Hatziargyriou, "Trends in microgrid control," *IEEE Transactions on Smart Grid*, vol. 5, pp. 1905–1919, July 2014.

[86] R. Majumder, "Some aspects of stability in microgrids," *IEEE Transactions on Power Systems*, vol. 28, pp. 3243–3252, Aug 2013.

[87] P. Kundur, J. Paserba, V. Ajjarapu, G. Andersson, A. Bose, C. Canizares, N. Hatziargyriou, D. Hill, A. Stankovic, C. Taylor, T. V. Cutsem, and V. Vittal, "Definition and classification of power system stability IEEE/CIGRE joint task force on stability terms and definitions," *IEEE Transactions on Power Systems*, vol. 19, pp. 1387–1401, Aug 2004.

[88] R. Majumder, *Modeling, stability analysis and control of microgrid*. Dissertation, Queensland University of Technology, Australia, 2010.

[89] M.-S. Ali, *Control Strategies for the Next Generation Microgrids*. Dissertation, University of Toronto, Toronto, ON. Canada, 2012.

[90] J. Elizondo and J. L. Kirtley, "Effect of inverter-based dg penetration and control in hybrid microgrid dynamics and stability," in *2014 Power and Energy Conference at Illinois (PECI)*, pp. 1–6, Feb 2014.

[91] E. Barklund, N. Pogaku, M. Prodanovic, C. Hernandez-Aramburo, and T. C. Green, "Energy management in autonomous microgrid using stability-constrained droop control of inverters," *IEEE Transactions on Power Electronics*, vol. 23, pp. 2346–2352, Sept 2008.

[92] M. B. Delghavi and A. Yazdani, "Islanded-mode control of electronically coupled distributed-resource units under unbalanced and nonlinear load conditions," *IEEE Transactions on Power Delivery*, vol. 26, pp. 661–673, April 2011.

[93] A. Mehrizi-Sani and R. Iravani, "Potential-function based control of a microgrid in islanded and grid-connected modes," *IEEE Transactions on Power Systems*, vol. 25, pp. 1883–1891, Nov 2010.

[94] N. Soni, S. Doolla, and M. C. Chandorkar, "Improvement of transient response in microgrids using virtual inertia," *IEEE Transactions on Power Delivery*, vol. 28, pp. 1830–1838, July 2013.

[95] N. Jayawarna, X. Wu, V. Zhang, N. Jenkins, and M. Barnes, "Stability of a microgrid," in *The 3rd IET International Conference on Power Electronics, Machines and Drives, 2006. PEMD 2006*, pp. 316–320, April 2006.

[96] F. Katiraei, M. R. Iravani, and P. W. Lehn, "Small-signal dynamic model of a micro-grid including conventional and electronically interfaced distributed resources," *IET Generation, Transmission Distribution*, vol. 1, pp. 369–378, May 2007.

[97] N. Pogaku, M. Prodanovic, and T. C. Green, "Modeling, analysis and testing of autonomous operation of an inverter-based microgrid," *IEEE Transactions on Power Electronics*, vol. 22, pp. 613–625, March 2007.

[98] N. Bottrell, M. Prodanovic, and T. C. Green, "Dynamic stability of a microgrid with an active load," *IEEE Transactions on Power Electronics*, vol. 28, pp. 5107–5119, Nov 2013.

[99] E. Nasr-Azadani, C. A. Caizares, D. E. Olivares, and K. Bhattacharya, "Stability analysis of unbalanced distribution systems with synchronous machine and dfig based distributed generators," *IEEE Transactions on Smart Grid*, vol. 5, pp. 2326–2338, Sept 2014.

[100] J. Sun, "Small-signal methods for ac distributed power systems;a review," *IEEE Transactions on Power Electronics*, vol. 24, pp. 2545–2554, Nov 2009.

[101] J. Sun, "Impedance-based stability criterion for grid-connected inverters," *IEEE Transactions on Power Electronics*, vol. 26, pp. 3075–3078, Nov 2011.

[102] A. C. R. Kamel and K. Nagasaka, "Detailed analysis of micro-grid stability during islanding mode under different load conditions," *Engineering*, vol. Vol. 3, no. No. 5, pp. pp. 508–516, 2011.

[103] E. N. Azadani, C. Canizares, and K. Bhattacharya, "Modeling and stability analysis of distributed generation," in *2012 IEEE Power and Energy Society General Meeting*, pp. 1–8, July 2012.

[104] R. D. MIDDLEBROOK, "Input filter considerations in design and application of switching regulators," *IAS'76*, 1976.

[105] J. Elizondo, R. Y. Zhang, P. H. Huang, J. K. White, and J. L. Kirtley, "Inertial and frequency response of microgrids with induction motors," in *2016 IEEE 17th Workshop on Control and Modeling for Power Electronics (COMPEL)*, pp. 1–6, June 2016.

[106] M. Farrokhabadi, C. A. Caizares, and K. Bhattacharya, "Frequency control in isolated/islanded microgrids through voltage regulation," *IEEE Transactions on Smart Grid*, vol. 8, pp. 1185–1194, May 2017.

[107] Y.Z. Zhang, "Capacity-based adaptive droop control for battery energy storage operation," in *2017 IEEE Power and Energy Society General Meeting*, pp. 1–5, July 2017.

[108] J. Han, "Control theory, is it a model analysis approach or a direct control approach?," *Syst. Sci. Math.*, vol. 9, pp. 328–335, May 1989 (in Mandarin Chinese).

[109] J. Han, "From PID to Active Disturbance Rejection Control," *IEEE Transactions on Industrial Electronics*, vol. 56, pp. 900–906, March 2009.

[110] J. C. Das, "Effects of momentary voltage dips on the operation of induction and synchronous motors," *IEEE Transactions on Industry Applications*, vol. 26, pp. 711–718, Jul 1990.

[111] T. Short, *Electric Power Distribution Handbook, Second Edition*. Taylor & Francis, 2014.

[112] H. W. Dommel, "Digital computer solution of electromagnetic transients in single- and multiphase networks," *IEEE Transactions on Power Apparatus and Systems*, vol. PAS-88, pp. 388–399, April 1969.

[113] H. Willis, *Power Distribution Planning Reference Book, Second Edition*. Power Engineering (Willis), CRC Press, 2004.

[114] W. H. Kersting, "Radial distribution test feeders," in *2001 IEEE Power Engineering Society Winter Meeting. Conference Proceedings (Cat. No.01CH37194)*, vol. 2, pp. 908–912 vol.2, 2001.

[115] "Standard load models for power flow and dynamic performance simulation," *IEEE Transactions on Power Systems*, vol. 10, pp. 1302–1313, Aug 1995.

[116] P. Krause, O. Wasynczuk, S. Sudhoff, and S. Pekarek, *Analysis of Electric Machinery and Drive Systems*. IEEE Press Series on Power Engineering, Wiley, 2013.

[117] J. J. Cathey, R. K. Cavin, and A. K. Ayoub, "Transient load model of an induction motor," *IEEE Transactions on Power Apparatus and Systems*, vol. PAS-92, pp. 1399–1406, July 1973.

[118] E. Kimbark, *Power System Stability, Volumes I, II, III, 3 Volume Set*. IEEE Press Series on Power Engineering, Wiley, 1995.

[119] "Matlab simscape power systems blocks reference," tech. rep., MathWorks, 1 Apple Hill Drive, Natick, MA 01760-2098, January 2018.

[120] J. Grainger and W. Stevenson, *Power system analysis*. McGraw-Hill series in electrical and computer engineering: Power and energy, McGraw-Hill, 1994.

[121] N. Jaleeli, L. S. VanSlyck, D. N. Ewart, L. H. Fink, and A. G. Hoffmann, "Understanding automatic generation control," *IEEE Transactions on Power Systems*, vol. 7, pp. 1106–1122, Aug 1992.

[122] "IEEE Recommended Practice for Excitation System Models for Power System Stability Studies," *IEEE Std 421.5-2016 (Revision of IEEE Std 421.5-2005)*, pp. 1–207, Aug 2016.

[123] I. C. Report, "Excitation system models for power system stability studies," *IEEE Transactions on Power Apparatus and Systems*, vol. PAS-100, pp. 494–509, Feb 1981.

[124] Y. G. Rebours, D. S. Kirschen, M. Trotignon, and S. Rossignol, "A survey of frequency and voltage control ancillary services mdash;part i: Technical features," *IEEE Transactions on Power Systems*, vol. 22, pp. 350–357, Feb 2007.

[125] K. E. Yeager and J. R. Willis, "Modeling of emergency diesel generators in an 800 megawatt nuclear power plant," *IEEE Transactions on Energy Conversion*, vol. 8, pp. 433–441, Sep 1993.

[126] Ibraheem, P. Kumar, and D. P. Kothari, "Recent philosophies of automatic generation control strategies in power systems," *IEEE Transactions on Power Systems*, vol. 20, pp. 346–357, Feb 2005.

[127] T. Zhang, J. A. Orr, and A. E. Emanuel, "Adaptable energy storage system control for microgrid stability enhancement," in *2018 IEEE Power and Energy Society General Meeting*, pp. 1–5, August 2018[Accepted].

[128] Tan Zhang, *Adaptive Converter Control for Fast Frequency Regulation*. Provisional Patent Number 62/645,393, filed March 20, US, 2018.

[129] J. Elizondo and J. L. Kirtley, "Effect of DG and induction motor load power rating on microgrid transient behavior," in *ISGT 2014*, pp. 1–5, Feb 2014.

[130] G. K. Stefopoulos and A. P. Meliopoulos, "Induction motor load dynamics: Impact on voltage recovery phenomena," in *2005/2006 IEEE/PES Transmission and Distribution Conference and Exhibition*, pp. 752–759, May 2006.

[131] J. Elizondo, P.-H. Huang, J. L. Kirtley, and M. S. Elmoursi, "Enhanced critical clearing time estimation and fault recovery strategy for an inverter-based microgrid with IM load," in *2016 IEEE Power and Energy Society General Meeting (PESGM)*, pp. 1–5, July 2016.

[132] "NEMA MG 1-2016," Mar 2017.

[133] D. Kosterev, A. Meklin, J. Undrill, B. Lesieutre, W. Price, D. Chassin, R. Bravo, and S. Yang, "Load modeling in power system studies: WECC progress update," in *2008 IEEE Power and Energy Society General Meeting (PESGM)*, pp. 1–8, July 2008.

[134] D. James and J. D. Kueck, "Commercial Building Motor Protection Response Report, No. PNNL-24468," June 2015.

[135] A. H. Bonnett, "The impact that voltage and frequency variations have on ac induction motor performance and life in accordance with nema mg-1 standards," in *Pulp and Paper, 1999. Industry Technical Conference Record of 1999 Annual*, pp. 16–26, June 1999.

[136] H. Vu, P. Pruvot, C. Launay, and Y. Harmand, "An improved voltage control on large-scale power system," *IEEE Transactions on Power Systems*, vol. 11, pp. 1295–1303, Aug 1996.

[137] "Powerworld simulator 18 block diagrams," tech. rep., PowerWorld Corporation, 2001 S First Street Champaign, IL 61820, May 2014.